IDCOR

Technical Report 15.2B Debris Coolability, Vessel Penetration, and Debris Dispersal

August 1983

by:
Fauske & Associates, Inc.
Burr Ridge, Illinois

B-18

The Industry Degraded Core Rulemaking Program, Sponsored By the Nuclear Industry

NOTICE

This report was prepared on account of work under contract to the Atomic Industrial Forum. Neither the Atomic Industrial Forum, nor any of its employees or members, the IDCOR Policy Group or the IDCOR or Atomic Industrial Forum consultants and contractors, makes any warranty, expressed or implied, or assumes legal liability or responsibility for the accuracy, completeness or usefulness of any information, apparatus, product or process disclosed, or represents that its use would not infringe privately-owned rights.

The opinions, conclusions, and recommendations set forth in this report are those of the authors and do not necessarily represent the views of the Atomic Industrial Forum, Inc., its employees, or the IDCOR Policy Group, its members, or the Atomic Industrial Forum or IDCOR Policy Group consultants or contractors.

Because IDCOR is supported in part by Federal funds, the following notice is required by Federal regulations:

The Atomic Industrial Forum's IDCOR activities are subject to Title VI of the Civil Rights Act of 1964, which prohibits discrimination based on race, color, or national origin. Written complaints of exclusion, denial of benefits, or other discrimination of those bases under this program may be filed with (among others) the Tennessee Valley Authority (TVA), Office of EEO, 400 Commerce Avenue EPB14, Knoxville, TN 37902, and must be *not later than 90 days from the date of the alleged discrimination*. Applicable TVA regulations appear in part 302 of Title 18, Code of Federal Regulations. Copies of the regulations, or further information, may be obtained from the above address on request.

TABLE OF CONTENTS

TABLE OF CONTENTS (Continued)

TABLE OF CONTENTS (Continued)

LIST OF FIGURES

LIST OF FIGURES (Continued)

LIST OF TABLES

ABSTRACT

Evaluations for in-vessel coolability, vessel failure, core dispersion and ex-vessel coolability have been formulated and basic models have been incorporated into both the BWR-MAAP and PWR-MAAP coding structures. These models suggest that in-vessel coolability could be potentially established if water were supplied to the reactor core region before core support plate failure and migration of the molten and degraded material into the lower plenum. One exception to this may be the depressurized state for a large break loss of coolant accident in a PWR system where the combination of a low system pressure and limited surface area could limit the coolability of a badly damaged core state. However, for pressures typical of small break loss of coolant accidents and transient events, coolability could potentially be established if water were added to the core. It should be noted that these are conservative evaluations since the governing physical process is assumed to be the counterflow of steam escaping from the debris in the presence of water flowing downward into the particulated bed.

Once material has migrated into the lower plenum, the time to reactor pressure vessel failure is sufficiently short that in-vessel debris coolability could not be established within the lower plenum. This is the case for both PWR and BWR systems and as a result, in-vessel coolability after such time is not credited in the MAAP coding structure.

For those BWR and PWR sequences where reactor pressure failure occurs with an elevated primary system pressure, the blowdown of gases from the primary system could influence the disposition of debris which has been discharged from the reactor pressure vessel. This is strongly influenced by the specific configuration of the reactor cavity/pedestal region and the surrounding containment regions. For a reactor cavity/instrument tunnel geometry like that in the Zion system, debris could be readily removed from the reactor cavity region and this has been demonstrated by small scale experiments using materials with a density approaching that of core debris. For other reactor cavity configurations, like that at Sequoyah, such intimate dispersal would not be likely, but some removal of debris could occur. For

the BWR-Mark-III systems with the "sunken" pedestal configuration, debris dispersal could potentially be achieved for those accident sequences in which there is a small blowdown from the primary system. However, for most BWR accident sequences, the activation of the Automatic Depressurization System (ADS) would result in a depressurized reactor vessel at the time of failure in the lower plenum. However, such physical behavior is modeled in the MAAP code and material can potentially be dispersed from the pedestal region. For those containment configurations typical of Mark-I and Mark-II containments, dispersion of core debris is not an important feature for describing the core material distribution between the pedestal and drywall regions. However, it could potentially distribute material into the suppression pool for immediate quenching and perhaps a sustained coolable state. Since there is currently insufficient data to make such detailed evaluations, this behavior is not modeled in the BWR-MAAP coding system for the Mark-I and Mark-II containments. This represents a conservatism in the analysis since such debris transportation into the suppression pool would be a positive response towards terminating the accident sequence.

Given the material distribution within the containment following reactor vessel failure, the ex-vessel coolability can generally be assured if water is available to the debris on a continual basis. As part of this evaluation, a heat transport path must be available from the debris to an ultimate heat sink such that the energy can be removed from the containment building. For some distributions of material, and in particular for some of the older containment buildings, thin layers of material can be coolable by directly exchanging their heat with the containment atmosphere through single-phased gaseous convection. This can provide cooling for debris configurations several centimeters thick, but again the essential part of the evaluation is the establishment of a heat transport path between the debris and an ultimate heat sink.

EXECUTIVE SUMMARY

Models have been developed to assess the potential for establishing in-vessel coolability, the mode of reactor pressure vessel failure should coolability not be established, the distribution of degraded core material after being released from the primary system and the potential for establishing ex-vessel coolability. These models have been compared to, and show agreement with the relevant experimental data where such is available, i.e. debris coolability and material dispersal. In addition, these have been incorporated into both the BWR-MAAP and PWR-MAAP coding systems to represent the integrated system response to postulated severe core damage accident sequences.

Severe core damage for an LWR system would only result if sufficient water could be lost from the primary system to result in uncovery of the reactor core. This uncovery must also be sustained for a considerable time interval, the exact value of which is dependent upon the detailed accident sequence. However, since water must be lost from the primary system to initiate core degradation, in-vessel coolability could only be established if water could subsequently be added to the reactor core. Given the availability of such a water source, the potential for establishing in-vessel coolability is assessed conservatively through a counter-flow of steam flowing upward from the debris bed in the presence of downward flowing liquid. This mechanism predicts that in-vessel debris coolability could potentially be established for most accident sequences if water is added to the degraded core while the material remains within the original core boundaries.

Evaluations are also presented for coolability with limited core damage and such evaluations are influenced by the specific design differences between BWR and PWR fuel assemblies. Specifically, the segmented core configuration for BWR assemblies allows considerable degradation to occur without destroying the interstitial channel configuration which constitutes the core by-pass flow in BWR systems. If water can be added to the core prior to the loss of this by-pass channel integrity, which can be approximately equated to melting of the stainless steel control rod blades, the core could be quenched

and a coolable configuration achieved for any accident sequence considered. This evaluation is independent of the actual configuration inside of the fuel cans, since it is assumed that the material has "lumped" together and completely blocked the internal channel regions. For the open lattice PWR configurations, the extent of limited core damage can generally be subscribed to the release of low melting point control rod material alloys into the fuel assemblies or the onset of zircaloy clad melting for those systems which have a high melting point control rod material. Liberation of molten material in the presence of no significant hydrodynamic forces would mean that such material would drain into the cooler regions of the core and resolidify. Once this type of blockage has been initiated, the evaluations considered should be those of extensive core damage.

Once core debris flows out of the original core boundaries and into the lower plenum of the reactor pressure vessel, those reactor vessel designs with lower head penetrations would experience failure of these penetrations within a time interval of several tens of seconds to a few minutes. This is insufficient time to remove the stored energy from significant amounts of core debris which would accumulate within the lower plenum, and thus in-vessel coolability for this configuration in the lower plenum would be very unlikely. For those reactor vessel designs without bottom penetrations, analyses indicate that the pouring of material into the lower plenum would result in failure of the reactor vessel within a few minutes. Therefore, this failure time is approximately the same as that calculated for those with lower head penetrations.

Given the initial failure, the discharge of molten material through the failure site would result in significant ablation of the reactor vessel wall. Thus, the breach size would be increased rapidly under such ablative attack, and significant quantities of core material (20 to 80 percent) could be discharged within a time interval of several seconds. In this analysis, the initial failure size has little influence on the discharge time, but the most important aspect of the analysis is that the material is discharged to the containment over a comparatively short time interval.

Once material has been released from the primary system into the containment, gaseous blowdown of the primary system would occur through the reactor vessel breach should the primary system be at an elevated pressure. BWR systems respond to many accident sequences by depressurizing through the Automatic Depressurization System (ADS) and would generally not undergo this depressurization immediately after vessel failure. Pressurized water reactors have a spectrum of small break and transient initiated accident sequences in which the primary system remains at an elevated pressure during the core degradation process. As a result, the primary system would undergo a rapid depressurization following a discharge of molten core debris and these blowdown forces could have a significant influence on the disposition of the debris within the containment. This debris dispersal is greatly influenced by the specific reactor cavity/instrument tunnel configuration and can vary from essentially all of the debris being relocated within the containment to all of the debris being retained within the reactor cavity. For the Zion and Sequoyah reference plants considered in the original containment analysis subtask, the reactor cavity configurations are sufficiently different that extensive debris dispersal would be anticipated for the Zion system with limited dispersal typifying the Sequoyah configuration.

Similar analysis apply to the BWR Mark-III system, which has a "sunken" pedestal configuration shows that debris dispersal could potentially occur for sequences with an elevated system pressure. However, these sequences do not dominate the accident spectrum for this BWR Mark-III containment. However, the BWR-MAAP code calculates the potential for dispersal should such accident sequences be considered.

Coolability of debris within the containment building is in general dependent upon the continued availability of water to the debris and the establishment of a heat transport path to extract this energy to the containment. In this regard, the debris dispersal can have a significant influence on the response of the containment since debris can be brought into intimate contact with water as a result of the dispersal process. This again is greatly dependent upon the specific configuration as well as the systems available for extracting heat from the containment. In general, this can be accomplished by normal containment heat removal systems including containment

sprays, fan coolers, etc. However, for some containments, particularly those with an uninsulated steel shell, the heat transport path can be one of direct energy transfer through the containment shell to the atmosphere as the ultimate heat sink. Any of these, or a combination thereof, can be sufficient to effect a permanently coolable state within the containment. However, given the variety of accident sequences and containment configurations considered, these assessments can be greatly different between various types of plants and also between accident sequences for the same plant.

1.0 INTRODUCTION

1.1 Background

Considerations of the governing physical processes during postulated severe core damage accidents involve the assessment of molten debris pouring into the lower plenum of the reactor pressure vessel and the subsequent potentials for steam generation, hydrogen generation, in-vessel debris coolability and the mode of failure for the reactor vessel. The assessments for steam and hydrogen generation, including steam explosions, are the subject of other IDCOR reports for subtask 12.1, Hydrogen Generation Ref. [1.1] and subtask 14.1, Steam Generation Refs. [1.2 and 1.3]. Downward melt propagation and the resulting configuration within the lower plenum of the reactor vessel is dependent upon the specific system design and would be greatly different for the boiling water and pressurized water reactor systems. Specifically, the analyses must include the different configurations resulting from the lower vessel control rod penetrations for BWRs as opposed to those which enter through the upper head in PWRs. These differences in the configuration influence both the steaming rates and the basic configuration to be evaluated for the attainment of in-vessel coolability.

Vessel failure is also greatly influenced by these specific configurations, in particular the lower head control rod drive and instrument tube penetrations for boiling water reactors and the in-core instrument tubes for most PWR systems which are mounted with limited depth penetration welds from the vessel interior. There are some PWR vessels without lower head penetrations and a different character of vessel failure must be considered for such designs. This additional consideration was evaluated in IDCOR subtask 15.2 and is discussed in Ref. [1.4].

Following vessel failure, debris would be discharged from the reactor pressure vessel into the containment and depending upon the specific accident sequence and the containment configuration, the debris could experience a variety of events. These would include ex-vessel steam explosions, dispersal of the debris, rapid quenching with water accumulated within the

containment and possibly core-concrete attack. The accident sequence has a major influence on these behaviors since many accident sequences result in a significant primary system pressure at the time of reactor pressure failure. As a result, the blowdown of the primary system through the vessel breach developed by the discharge of core material would exert significant forces on the debris which could be accumulated directly below the reactor pressure vessel. While the forces are determined by the accident sequence and the size of the vessel breach, the resulting distribution of the debris is greatly influenced by the specific configuration of the containment. Since there are various designs of reactor containment buildings for the plants considered in the IDCOR effort, considerations will be given in this report to those containment buildings which comprise the four original reference plants for the IDCOR effort. These systems are Zion (PWR with a large dry containment), Sequoyah (PWR with an ice condenser containment), Peach Bottom (BWR with a Mark-I containment), and Grand Gulf (BWR with a Mark-III containment). The dispersal potential as a function of the accident sequence will be discussed for these various configurations. In addition, the effects of deviations from these four reference plants will also be addressed.

As the debris configurations are developed within this ex-vessel state the potential for achieving a permanently coolable state would also be evaluated. In addition, the energy must also be extracted from the containment building, hence the potential for establishing a heat transport path to extract the energy is also an important part of such evaluations. With the exception of some older reactor systems, which have a limited amount of core material and a sizable containment building, the potential for achieving an ex-vessel coolable state can be directly related to the availability of water to the debris on a permanent basis. Again, this can be related to the specific reactor building configuration and the manner in which the heat transport path is established. This will also be addressed for the four difference reference plants considered in the IDCOR containment evaluation, subtask 23.1.

These phenomena and their relevance to various accident sequences will be considered by first summarizing the pertinent issues, next presenting the basic considerations for the relevant physical processes, followed by the

pertinent experimental information, and lastly the application to the reactor system.

1.2 References

1.1 "Hydrogen Generation During Severe Core Damage Sequences," Fauske & Associates Report No. FAI/82-33, December 1982.

1.2 "Final Report of Key Phenomenological Models for Assessing Explosive Steam Generation Rates," Fauske & Associates Report No. FAI/82-26, December 1982.

1.3 "Final Report of Key Phenomenological Models for Assessing Non-Explosive Steam Generation Rates," Fauske & Associates Report No. FAI/82-30, December 1982.

1.4 L. E. Anderson, et. al., "Effects of Hypothetical Core Melt Accidents on a PWR Vessel With Top-Entry Instruments," EPRI/NSAC Final Report for IDCOR Subtask 15.2, May 1983.

2.0 PERTINENT ISSUES

2.1 Introduction

These evaluations which begin with the material migration out of the original core boundaries and describe the basic physical processes for the debris through the assessment of ex-vessel coolability. Included in these analyses are, in-vessel coolability for the material in the lower plenum of the reactor pressure vessel, the mode of reactor vessel failure and the processes dictating the size of the vessel failure, the dispersal potential of debris as it exists the primary system and accumulates within the containment, and finally the potential for establishing a coolable state in an ex-vessel configuration.

2.2 In-Vessel Coolability

For this assessment a knowledge of the vessel failure mode and the time interval between molten material pouring into the lower plenum and the onset of vessel failure. Since substantial quantities of molten material would likely flow into the lower plenum within a very short time interval, this substantial energy inventory must be removed for vessel failure to establish a coolable configuration. Should this be the case, then evaluations of particle size and distributions may be considered also. However, if the debris accumulation results in vessel failure in a time interval which is short compared to that required to extract the considerable stored energy from the melt, then vessel failure would be anticipated well before a coolable state could be achieved and material would be discharged from the primary system. As will be discussed, this appears to be the case both for those vessels with extensive bottom head penetrations and also for those without. Consequently, potential for obtaining in-vessel coolability once the material has migrated out of the original core boundaries is generally not given a high probability of success.

2.3 Vessel Failure

Accumulation of debris within the lower plenum of those vessels with lower head penetrations results in an accentuated attack on the partial

penetration welds. Failure of a penetration allows the high temperature debris to be discharged through the failure location. Should the debris be molten, which would likely be the case, the high temperature of the material would ablate the steel vessel wall and enlarge the failure site. This ablation process is dependent upon the temperature of the debris and the pressure within the primary system at the time of vessel failure. The model for this ablation process is developed in Section 3.

For those configurations without lower head penetrations, the initial contact and accumulation of debris would produce thermal attack on the reactor vessel wall. In particular, a jet of molten debris resulting from the failure of the core support structure would cause an accentuated attack on a localized area of the reactor vessel head. This was addressed as part of the EPRI/NSAC participation in the IDCOR program and this evaluation has demonstrated a timed vessel failure of a few minutes as opposed to several tens of minutes required to attack the entire reactor vessel head. This analysis is included as Appendix B to this report.

2.4 Debris Dispersal

For those postulated accident scenarios where the reactor vessel would be penetrated by molten debris, the debris would tend to be accumulated within the containment directly below the reactor vessel. Should there be significant pressure within the primary system at the time of reactor vessel failure, the gaseous blowdown forces would be directed at the debris and could potentially have a significant influence on the debris distribution within the containment building.

As was considered in the Zion Probabilistic Safety Study [2.1], relocation of the debris from the reactor cavity could be the result of the hydrodynamic forces resulting from core debris ejecting from the primary system, wave formation within the molten pool as the gaseous blowdown is initiated and from the direct entrainment of debris as the gas flows over the top of the debris configurations. These mechanisms were considered individually and were shown to have the same basic result for the Zion containment configuration; the debris would be moved from the reactor cavity region by

these blowdown forces with the principle mass of debris being contained in a single wave of liquid and solid material. This removal and distribution in the containment were evaluated for the specifics of the Zion containment design.

Similar evaluation was carried out in Ref. [2.2] for the Limerick BWR Mark-II configuration. In this assessment, the parallel flow paths between the entrance to the vessel pedestal region from the drywell (the personnel passageway) and those additional openings such as the windows for the control rod drive hydraulic lines were evaluated. These other gaseous flow paths were shown to have a significant influence on the gas flow distribution within the pedestal region and therefore the subsequent relocation of core material. Hence, these calculations illustrated that the specific configuration must be evaluated for a given plant evaluation.

In Section 6, Application to Reactor Systems, the specific configurations for the four original IDCOR reference plants will be discussed. Given the specific geometries, considerably different behaviors could be anticipated for similar types of accident initiators.

2.5 Ex-Vessel Coolability

Evaluation of debris coolability within the containment configuration are generally dependent upon two major features: (1) the distribution of debris within the containment building and (2) the availability of water to the debris. These features are greatly influenced by the specific containment building configuration and the various manners in which water may be held up within the containment building or supplied to the containment building floors. In addition, the coolability assessment must include an evaluation of the heat transport paths that could provide water to the debris on a continual basis. This could be accomplished through active and passive means within the containment building as well as through the initiation of water addition to the primary system should such features become available during such an accident.

The debris distribution, water accumulation, and the development of a heat transport path will be addressed for each of the four original IDCOR

reference plants in Section 6. These discussions will specifically reflect the manner in which such considerations were included in the MAAP code modeling for these reference plants. The results of this modeling have been initially presented in the preliminary analyses for these plants and will also be discussed in the final report. these plants in IDCOR subtask 23.1.

2.6 Summary

In the chronology of an accident sequence, that time interval between when the core material leaves its original boundaries and when the potential for sustained core-concrete interaction is evaluated includes detailed assessments of several pertinent issues. These are (1) in-vessel coolability, (2) mode of vessel failure, (3) core debris dispersion, and (4) ex-vessel coolability. These issues have a substantial influence on the progression or regression of the accident sequence and they define those states which can result in a safe stable state such that the accident is terminated. As will be discussed in the following sections, these are influenced by the specific configurations of both the primary system and the reactor containment building.

2.7 References

2.1. "Zion Probabilistic Safety Study," Commonwealth Edison Company, September 1981.

2.2. "Probabilistic Risk Assessment Limerick Nuclear Generating Station," Philadelphia Electric Company, April 1982.

3.0 BASIC CONSIDERATIONS

3.1 Introduction

For the assessments of in-vessel debris coolability, vessel failure, debris dispersion and ex-vessel debris coolability, several features must be evaluated including the dryout heat flux for particulated debris beds, the ablation characteristics for molten debris flowing through the initial breaches within a reactor pressure vessel and the forces acting upon the debris to result in dispersion for those accident sequences in which the primary system is at a substantial pressure at the time of reactor pressure vessel failure. These will be discussed in this section with the phenomenological assessments being detailed in terms of (a) coolability of particulated debris beds, (b) ablative phenomena and (c) core dispersive mechanisms. These features are general in nature and are potentially applicable to both BWR and PWR systems. However, with the specific lower plenum configuration in BWR systems, other features must be addressed including the freezing of debris on the surface of control rod drive guide tubes which contain water. This will be considered following the general considerations for both reactor systems.

3.2 Coolability of Particulated Debris Beds

3.2.1 Governing Physical Processes

For a one-dimensional debris bed with an overlying water pool, the principal limitation is one of water flowing downward through the bed in the presence of upward flowing steam. Experimental measurements [3.1-3.3] have shown that for debris beds with uniform particles, with sizes of hundreds of microns and larger, dryout generally occurs between the central region and the top of the bed. Such observations demonstrate the process is not one of preventing water from penetrating to the bottom of the bed (in which case dryout would occur at the bottom), but one of a counter-flow limitation in which the vapor "floods" the liquid either within or at the top of the debris bed. For a top flooding mechanism, this limitation can be envisioned as occurring in two different ways as illustrated in Fig. 3.1. The first is a limitation on the ability of a liquid film to remain on a particle in the

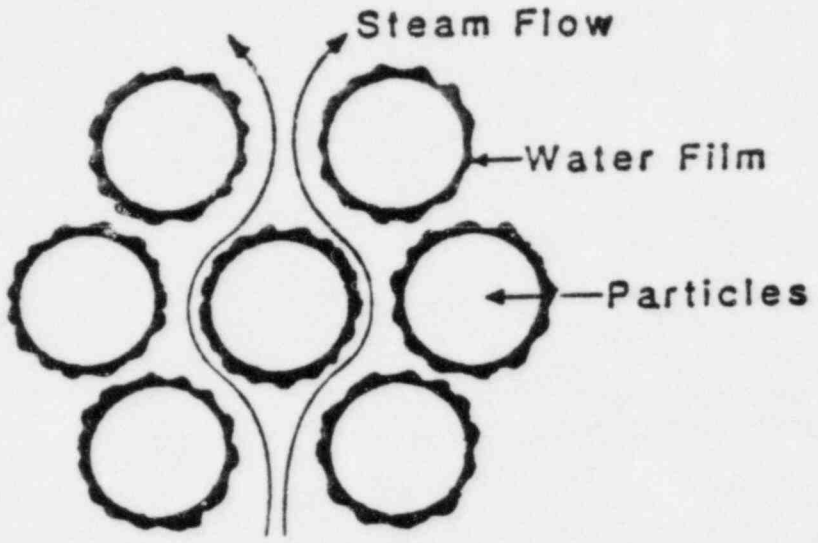

a) Drag on a Liquid Film

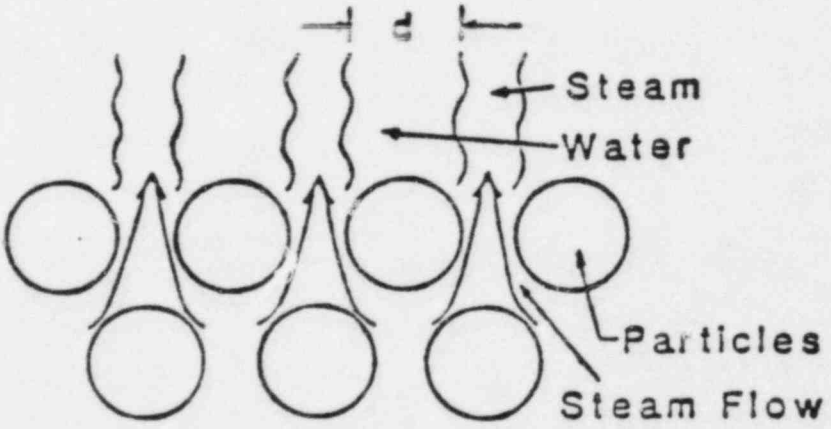

b) Hydrodynamic Limitation
Above the Bed

Fig. 3.1 Hydrodynamic limitations.

presence of the upward vapor flow and the second is a limitation immediately above the bed wherein the upward flowing vapor levitates the liquid immediately over the bed. In both of these cases, the governing liquid dimension is the size of the particle as discussed below.

For the first case, liquid covers the particle as a thin film and the levitation criteria only comes into effect when the drag on the liquid is sufficient to cause a net upward movement of the liquid film. In effect, this can be evaluated by assuming the whole particle has the density of the coolant (ρ_f) and assessing the drag forces necessary to levitate this liquid particle.

$$(\rho_f - \rho_g)\ 4/3\ \pi r_p^3 g = C_D \pi r_p^2 \frac{\rho_g U_g^2}{2} \qquad (3.1)$$

In this expression, g is the acceleration of gravity, ρ_g is the vapor density, r_p is the particle radius, C_D is the effective drag coefficient and U_g is the superficial steam velocity. At the point of levitation, the drag imposed by the coolant moving through the particles is sufficient to cause net upward movement of the liquid mass, thereby eventually leading to a dryout of the debris bed.

In the second mechanism, vapor is flowing upward through the porous regions between the particles, therefore the characteristic dimension separating the vapor channels is the particle diameter. As a result, if the upward vapor flow levitates the liquid above the bed, the liquid globules would have a characteristic dimension equal to the particle size. Formulating the levitation criteria with the upward vapor flow results in the same expression given above, i.e. the analytical description is identical for both of these mechanisms. The principal feature to be addressed is the effective drag coefficient in a densely packed particle bed; this will be addressed later.

This top flooding limitation is applicable as long as a more limiting condition does not occur within the bed and when the characteristic dimension determined by the particle size is greater than that characteristic dimension determined by the stability characteristics of the coolant, i.e.

capillary sizes. The limitation within the bed can be considered in terms of another counter-flow mechanism in which the vapor drag on the liquid can be greater than that treated as a configuration of smooth liquid droplets in a dense configuration. Within the bed, the liquid-vapor drag is a function of the specific liquid configuration including its thickness, effective roughness, etc. This will be treated by examining the experimental data for various particle sizes which indicate a dependence on the bed depth, the degree of this dependence being a function of the particle size.

As part of the evaluation of limitations within or above the bed, considerations must be given to the stability of a liquid film on the surface of the individual particles. Specifically, does nucleation occur beneath the film or is thermal conduction sufficient to remove the heat generated. Assuming liquid film thickness to be uniform on all particles, the film thickness (δ) can be expressed in terms of the average bed void fraction (α), bed porosity (ε), bed volume (V) and the particle diameter (d_p) as

$$\delta = \frac{V_f}{A_s} = \frac{(1 - \alpha)\varepsilon V}{N4\pi r_p^2} = \frac{(1 - \alpha)\varepsilon d_p}{6(1 - \varepsilon)} \tag{3.2}$$

The heat flux from the surface of a particle is a function of the total power generated within the bed (Q), the particle diameter, and the bed volume.

$$q/A)_B = \frac{Q}{N4\pi r_p^2} = \frac{Qd_p}{6(1 - \varepsilon)A \cdot L} \tag{3.3}$$

Considering the energy transfer across the liquid film to be via conduction, the temperature difference would be

$$\Delta T_f = \frac{q/A)_B\ (1 - \alpha)\varepsilon d_p^2}{36\ k_f\ (1 - \varepsilon)^2\ L} \tag{3.4}$$

where k_f is the liquid thermal conductivity. As indicated by this expression, the temperature difference is a strong function of the particle

diameter. This temperature difference across the film can be compared to the superheat required for the formation of bubbles in a uniform temperature field

$$\Delta T_{sup} = \frac{4\sigma T}{h_{fg}\, \rho_g\, \delta} \tag{3.5}$$

where h_{fg} is the latent heat of vaporization. If the temperature difference across the film is less than that required to support a vapor bubble in a uniform temperature field, then nucleation would not occur within the film and a limitation within the bed would be expected. Conversely, if the temperature difference across the film far exceeds that required to support vapor embryos, then nucleation would occur within the film and a configuration of liquid film surrounding the particles would likely not be appropriate.

To illustrate this general behavior, let us consider the data from Ref. [3.1,3.2,3.3]. For the experiments of Trenberth and Stevens [3.3], the largest particle size used was 2 mm in diameter, and at a bed depth of 80 mm, the dryout heat flux was $\sim$ 600 kw/m^2. A temperature drop across the water film of 0.4°C would be calculated. This is less than the value of 1°C typical of the superheat necessary to support a vapor embryo with the diameter equal to the film thickness. Consequently, nucleation within the film would not be anticipated and the limitation within the bed would be likely. Squarer, et al. [3.2] studied particle diameters up to 6.35 mm with a dryout heat flux of about 1400 kw/m^2 at a bed depth of $\sim$ 20 cm. Under these conditions, the film temperature drop would be 8.4°C, i.e. substantially greater than that required to support a bubble within a uniform film. In this configuration, nucleation beneath the film would be expected and the limitation would be somewhat different than the internal bed behavior of Trenberth and Stevens. For the data of Barleon and Werle, particle diameters of 1.6 cm were used with a dryout heat flux of $\sim$ 5000 kw/m^2 and a bed depth of 8 cm. For these conditions, a film temperature difference would exceed 300°C, i.e. two orders of magnitude above that necessary to support a bubble in a uniform temperature field. As a result, a continuous liquid film surrounding individual particles would not be a viable configuration and an internal bed limitation would not be anticipated. With this behavior, a limitation to sustain coolability of the bed should approach a hydrodynamic limitation at the upper surface of the bed.

For a reactor system, the volumetric internal heat generation at 1% of nominal power would be close to 2 Mw/m^3 and for a particle 1 cm in diameter, the surface 3.2 kw/m^2. With an assumed particle diameter of 1 mm, the surface heat flux would be 0.32 kw/m^2. Since both of these are more than an order of magnitude below those typical of the values in the experiments of Barleon and Werle [3.1] and Squarer, et al. [3.2], the two-phase flow pattern would also be considerably different. Behavior closer to the data of Trenberth and Stevens (an internal bed limitation) would be expected.

The data of Trenberth and Stevens Ref. [3.3] illustrate these different controlling mechanisms. For shallow beds, the dryout heat flux is larger, see Table 3.1, and decreases with increasing bed depth until a value is reached where the dryout heat flux remains constant (transition to another mechanism) for further increases. Figure 3.2 shows the bed depth at this transition to a constant dryout heat flux as a function of the particulate size. For the 20 mm deep bed of 2 mm diameter particles, the dryout heat flux is 1287 kw/m^2. The calculated film temperature difference is 8.6°C which is far greater than that required to sustain a stable bubble beneath the liquid film. Thus nucleation would be expected, disrupting the film and a different mechanism could control. Using a uniform superheat of 1°C, the prediction for the transition depth is shown in Fig. 3.2 and indicates the general behavior reported in Ref. [3.3]. Extrapolating these results to the large particle sizes used by Barleon and Werle suggests that the results are typical of either very thin films ($\sim$ 1 μm) or essentially no continuous film. In either case, the internal bed hydraulic resistance would begin to approach that typical of all vapor flow. However, such vapor fluxes exceed the hydrodynamic stability at the top of the bed, i.e. the limitation would occur at the top of the bed.

Another feature of limited interest when considering the hydrodynamic stability, is that produced by fixed beds with small particles. Should the particle size of a given bed be smaller than the capillary dimension for the coolant, then the limiting heat flux for levitating liquid above a uniform shallow bed would be that characteristic of a flat plate configuration, i.e. the vapor channels resulting in a hydrodynamic stability cannot be closer than that dimension characterized by the coolant. This is only of

Table 3.1

Dryout Data of Trenberth and Stevens for Water at 0.1 MPa

Particle Size mm	Bed Depth mm	Dryout Heat Flux kw/m^2
0.68	30	> 484
0.68	30	452
0.68	30	> 467
0.68	35	292
0.68	40	618
0.68	40	204
0.68	40	189
0.68	50	158
0.68	50	173
0.68	60	163
1.2	20	> 1395
1.2	30	373
1.2	30	> 1414
1.2	30	1924
1.2	40	360
1.2	40	1745
1.2	40	309
1.2	50	389
1.2	60	347
2.0	20	1287
2.0	25	586
2.0	30	930
2.0	40	955
2.0	40	834
2.0	52	836
2.0	60	669
2.0	75	611
2.0	90	475

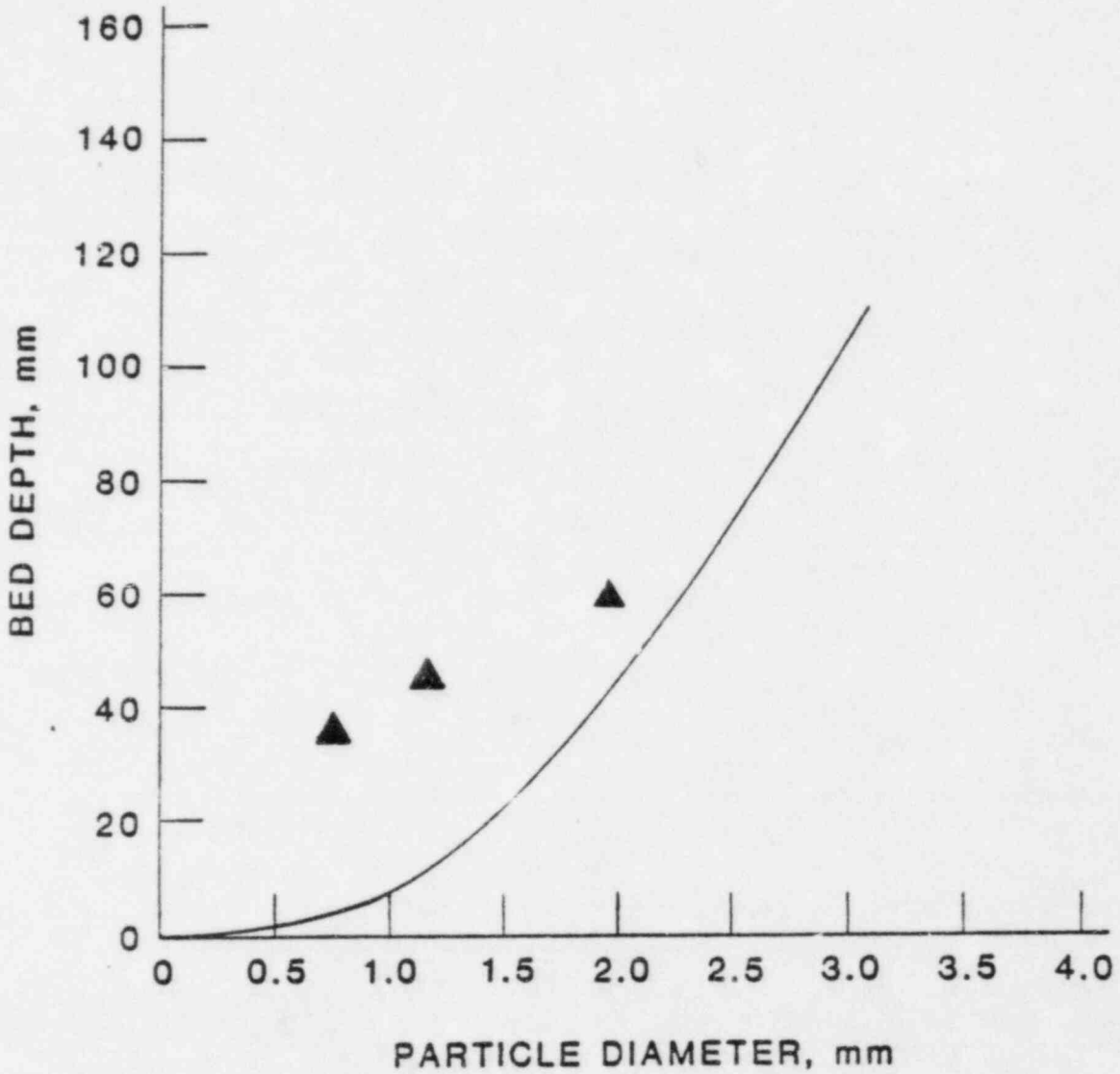

Fig. 3.2 Water transition bed depth measured by Trenberth and Stevens.

interest for shallow beds with particle sizes of the order of a few mm. In such shallow beds movement of the particles and "channeling" has also been observed and these changes in configuration would also substantially increase the heat flux and alter the basic considerations associated with hydrodynamic stability.

3.2.2 Analytical Models

Particle drag has been investigated with respect to a dense packing of uniform spheres in a flowing media. The definitive experiments of Rowe [3.4] and Rowe, et al. [3.5] have illustrated that the drag on individual spheres in the most dense configuration can be $\sim$ 68 times the drag of a single sphere in an infinite stream at the same Reynolds number. If the packing fraction is decreased to that characteristic of a cubic configuration, which has a porosity of $\sim$ 50%, the drag is approximately 20 times that for an individual sphere in an infinite stream. These experimental results were expanded to include various types of porous conditions and it was demonstrated that the only major reduction in drag occurs when there is a continuous (straight-line) fluid path through the debris configuration. A relation for the drag can be derived using the pressure gradient through a particle bed at the incipient fluidization point, i.e. that condition where the pressure drop through the bed exactly equals the weight of the particles divided by the cross-sectional area of the bed. The pressure gradient required for a specific fluid velocity can be equated to the gradient representing the static weight of the bed at incipient fluidization as expressed by

$$\frac{dP}{dz} = 2C_f \frac{\rho_f U^2}{d} \frac{(1 - \varepsilon)}{\varepsilon^3} = (1 - \varepsilon)(\rho_p - \rho_f)g \tag{3.6}$$

where C_f is the effective friction factor within the bed. This results in an expression for the incipient fluidization velocity as dictated by the particle and fluid densities, the bed porosity, and the particle diameter.

$$U^2 = \frac{(\rho_p - \rho_f)gd\varepsilon^3}{2C_f\rho_f} \tag{3.7}$$

At this point the drag on each individual particle exactly equals the weight of the particle,

$$(\rho_p - \rho_f)g \frac{\pi d^3}{6} = C_D \pi \frac{d^2}{4} \frac{\rho_f U^2}{2} \tag{3.8}$$

Substituting the above formulation for the fluid velocity into this expression gives the drag coefficient on an individual sphere in terms of the frictional coefficient for the total bed.

$$C_D = \frac{8}{3} \frac{C_f}{\varepsilon^3} \tag{3.9}$$

Wallis [3.6] gives an expression as proposed by Ergun [3.7] for the effective friction factor which encompasses both the laminar and turbulent regimes

$$C_f = \frac{75}{N_{Rep}} + 0.875 \tag{3.10}$$

where N_{Rep} is the particle Reynolds number which is defined in terms of the standard Reynolds number for an individual sphere by $N_{Rep} = N_{Re}/(1-\varepsilon)$. The first term represents the laminar behavior, which controls for small particle diameters, and the second term represents the turbulent regime. Substituting this equation into the expression for the effective coefficient on a sphere within a packed bed at the fluidization point results in

$$C_D = \frac{8}{3\varepsilon^3} \frac{75(1 - \varepsilon)}{N_{Re}} + 0.875 \tag{3.11}$$

If this effective drag coefficient is ratioed with the drag of an individual sphere in an infinite stream of fluid, it is found that at the maximum packing fraction for uniform particle sizes the drag for individual spheres is far greater than that of an isolated sphere as shown in Fig. 3.3. This formulation for particle drag when substituted into Eq. (3.1) results in a prediction for the hydrodynamic stability limit at the top of the bed. If the particle diameter is less than the coolant capillary dimension, the flat plate saturated CHF value should be used to determine the stability limit.

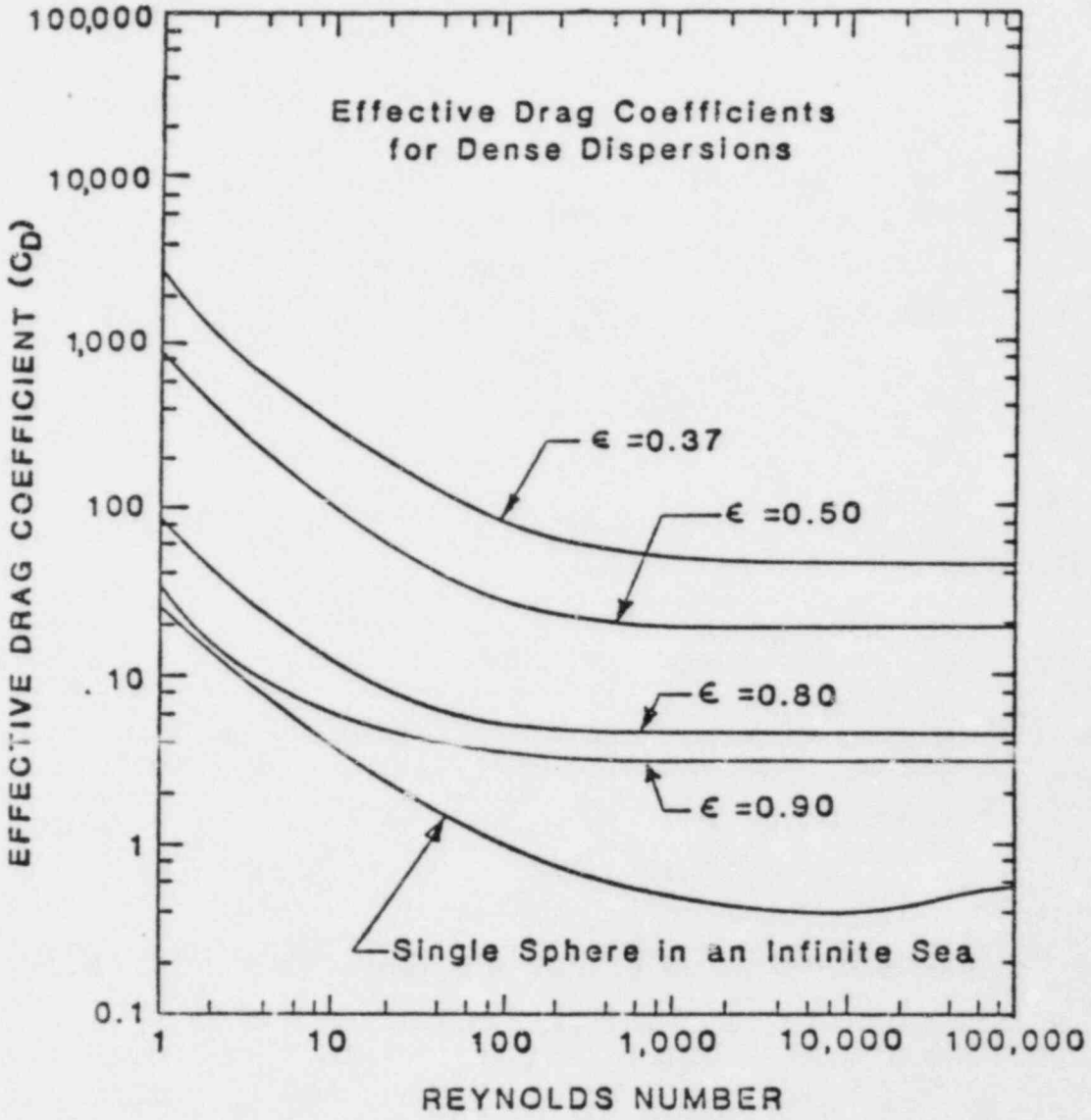

Fig. 3.3 Effective drag coefficients.

The above expressions are for a single-phase fluid through a dense bed of particles. For liquid-vapor interaction within the bed, a higher pressure drop would be anticipated. This can be represented using the same form as Eq. (3.10) with the turbulent coefficient increased from 0.875 to 7 as determined from the data of Trenberth and Stevens [3.3].

These representations for hydrodynamic stability and internal limitation models are compared to other analytical approaches in Fig. 3.4 for a bed porosity of 0.4. As illustrated, at this porosity, the Lipinski [3.8] and Ostensen [3.9] models are very close to the hydrodynamic stability model for large particle sizes and the laminar asymptote is in agreement with the models proposed by Hardee-Nilson [3.10] and Dhir-Catton [3.11].

3.2.3 Two-Dimensional Considerations

For those configurations in which the debris is completely surrounded by water, as illustrated in Fig. 3.5, the supply of water to cool the bed would not be limited by the counter-flow addition of water from above since radially inward flow would occur. While this is a complex process, the effect of this two-dimensional process can be estimated by considering the steam outflow at the top of the bed. If the pressure gradient through such a bed is assumed to be one-dimensional, the gradient at the top of the bed created by the steam flow can be equated to the static head of liquid imposed by the surrounding pool. In this case the fluid at the top of the bed is saturated or superheated steam as compared to the counter-flow of saturated steam and water for the top flooding systems. The balance of static head and frictional gradient developed by the steam flow can be expressed as

$$-\frac{dP}{dz} = 2C_f \frac{\rho_g U^2}{d} \frac{(1-\epsilon)}{\epsilon^3} = (\rho_f - \rho_g)\, g \qquad (3.12)$$

where C_f describes the frictional resistance for single-phase flow through a particle bed. As described in Wallis [3.6], this frictional coefficient can be empirically represented by Eq. (3.10). Substituting this into the above

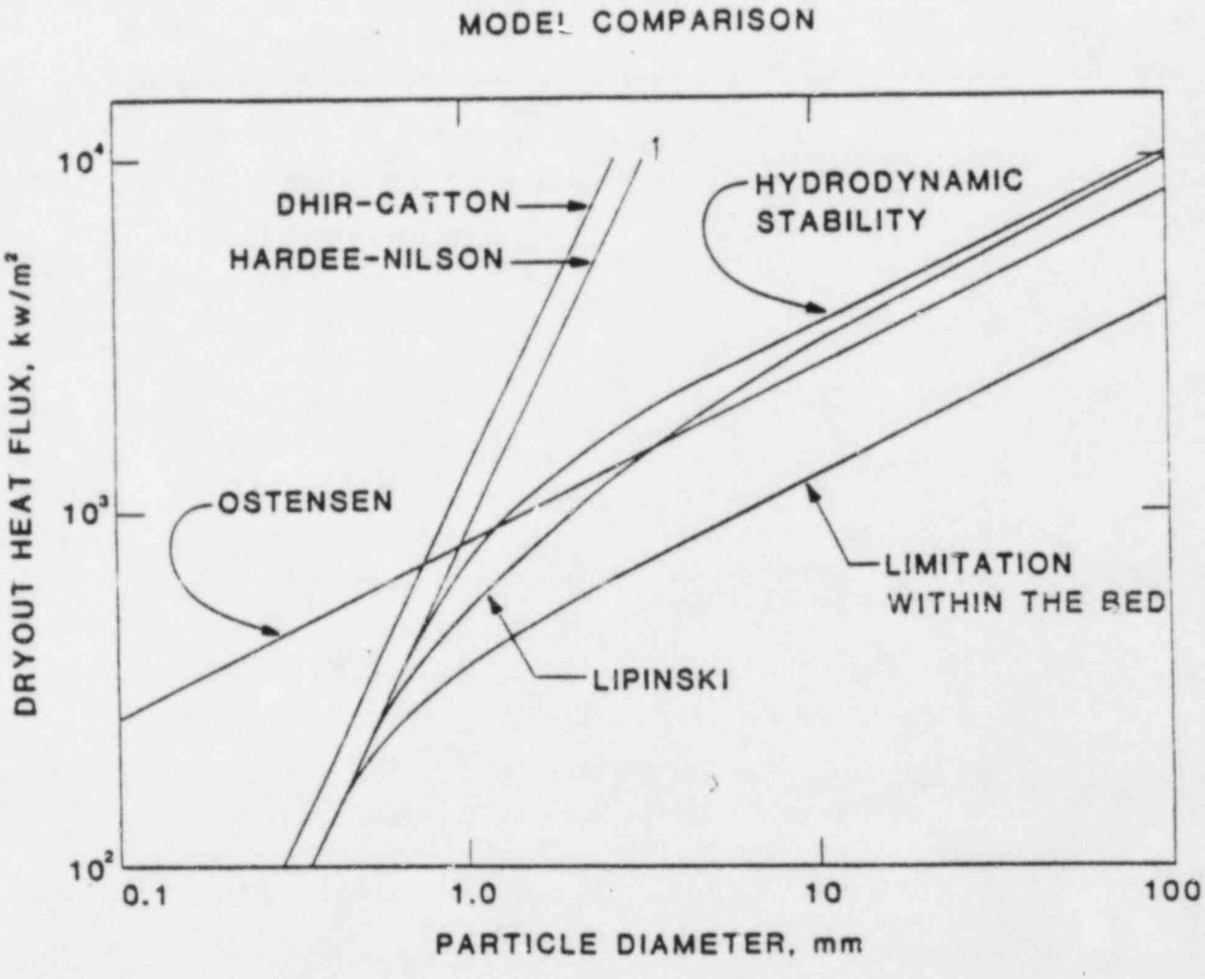

Fig. 3.4 Dryout heat flux models for debris beds.

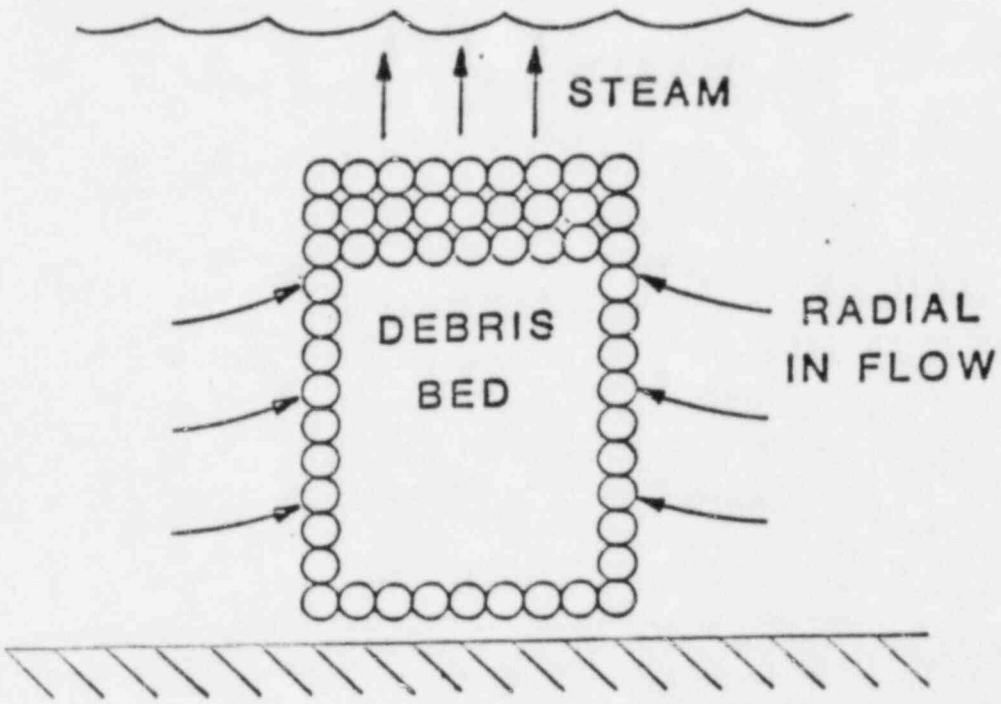

Fig. 3.5 Approximate configuration for a two-dimensional debris bed.

momentum equation, the maximum steam velocity can be determined and translated into the maximum heat flux that can be extracted from the bed.

$$q/A = \left[\frac{(\rho_f - \rho_g) g d \varepsilon^3 P}{2C_f(1-\varepsilon)RT}\right]^{1/2} [h_g - h_\ell + C_p(T_g - T_{sat})] \qquad (3.13)$$

where the vapor is assumed to behave as a perfect gas. This accounts for the energy removed by saturated or subcooled water entering the bed and exiting at the critical velocity representative of the saturated or superheated condition. Adding superheat to the steam increases the energy content of the steam, but also decreases the density and thus decreases the flow rate needed to balance the static head of liquid. Predictions for the limiting heat flux given in Table 3.2 for a particle size of 1 cm and a bed porosity of 0.45. As illustrated the saturated steam outlet condition represents a value of 5160 kw/m^2, which is about 40% greater than the hydrodynamic stability prediction. Table 3.2 also demonstrates the effect of superheat which initially causes a decrease in the heat flux (probably due to the perfect gas assumption) and then increases somewhat for large superheats. In general, the additional heat removal due to superheating does not appear to provide a sizable additional amount of heat removal. Small amounts of liquid subcooling can provide more heat removal capacity than large vapor superheats.

3.3 Vessel Failure

For the postulated severe accident sequences in which a degraded core continues to melt and progresses to a point where the core material either "slumps" or is discharged into the lower plenum, the potential exists for thermal attack of the reactor vessel steel by the high temperature, degraded core material. The lower plenum region contains several different structural components which would experience this attack, including the reactor vessel wall, the lower core support structure, the supports for the in-core instrument penetrations, and the lower structure which guards against a hypothetical drop of the reactor internals. All of these components would experience thermal attack, but only the reactor vessel wall and the penetrations would be of concern for evaluating the time, location and size of the

Table 3.2

PREDICTIONS FOR THE MAXIMUM TWO-DIMENSIONAL HEAT REMOVAL FROM A PARTICLE BED COOLED BY WATER AT 0.1 MPa

$d = 0.01$ m $\qquad\qquad$ $\varepsilon = 0.45$

T_{in} K	T_{out} K	Maximum Heat Flux kw/m^2
293	373	5925
333	373	5543
353	373	5351
373	373	5160
373	473	5069
373	573	5048
373	673	5067
373	773	5108
373	973	5232
373	1373	5548
373	1873	5974

reactor vessel failure for these postulated, severe accident sequences. In this section, the thermal attack of the reactor vessel steel and the penetration welds (the expected failure mode) by the discharge of degraded core material into the lower plenum will be evaluated. Following this, the rate at which the core material would be discharged from the reactor vessel will be evaluated in terms of the pertinent thermal ablation process involved.

With material migration to the lower plenum, the water would either be vaporized or displaced by the debris. If the degraded material is held up on the core support structure until it collapses and then pours into the plenum as a molten stream, the water would undergo limited vaporization and would be displaced either the downcomer annulus or into the outer radial core zones which could still be intact. Extensive fragmentation would not occur, as discussed in Ref. [3.12 and 3.13], since a finely fragmented melt with all particles surrounded by water far exceeds the stability limit for the water, i.e. film boiling fragmentation model. As a result, the molten debris would penetrate directly to the bottom of the plenum where it could accumulate and begin to thermally attack the steel surfaces in this locale. The water could continue to vaporized off the upper surface of the debris pool, but this would not substantially affect the rate of attack of the vessel wall and the penetrations.

3.3.1 Thermal Attack of the Vessel Steel Structure by a Stream of Degraded Core Material

The thermal attack of a thick steel slab by a solidifying stream of degraded material that flows over one side of the slab (vessel wall), as shown in Fig. 3.6 has been evaluated. Predicting the steel melting rate and the temperature profile within the vessel wall is complicated by the behavior of a growing frozen crust on the melting steel surface. If it is assumed that the crust of core debris is mechanically stable and does not break up and expose the steel melt film to the flow of hot core debris, and that crust motion (sliding) does not produce appreciable convection currents within the steel melt film, the problem is greatly simplified. Considerable experimental support for frozen crust stability on an underlying melt layer can be found in the literature, Ref. [3.14 - 3.16].

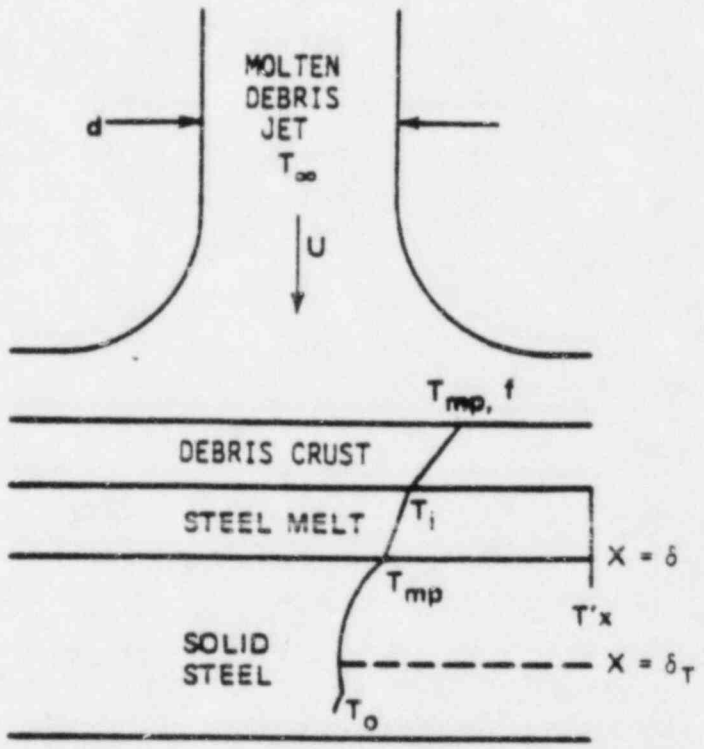

Fig. 3.6 Schematic diagram of frozen crust of core debris on melting steel slab.

In addition to the foregoing consideration of fuel crust stability, the following additional assumptions are made.

1. The analysis is restricted to the neighborhood of the stagnation point of the axisymmetric flow of core debris. According to measurements made with gas jets, the axisymmetric stagnation flow model breaks down at a radial distance of about 1.2 times the jet (or nozzle) diameter (d) Ref. [3.17]. The heat flux ($q/_A$) through the upper surface of the fuel crust within this radial stagnation zone is given by Ref. [3.18]

$$q/_A = 0.55\left(Pr_f^{0.35}\right)k_f(T - T_{mp,f})\left(\frac{2u}{d\nu_f}\right)^{1/2} \qquad (3.14)$$

where k_f, ν_f and Pr_f are the thermal conductivity, kinematic viscosity and Prandtl number of the flowing core debris. While this equation is strictly valid only for laminar stagnation flow, available heat transfer data for gas jets Refs. [3.19 and 3.20] and liquid streams Refs. [3.21 and 3.22] indicate that it can be successfully applied when the stream is turbulent.

2. The frozen layer of degraded core material, the steel melt layer and the thermal boundary layer within the solid steel are thin compared with their extension in the lateral direction so that heat conduction in this direction is small compared to that normal to the surface.

3. All physical properties (density, heat capacity, thermal conductivity) are considered constant for the solid and molten regions. In addition the change of volume upon solidification or melting is neglected. Perfect "thermal contact" between the crust of core debris and the steel at x = 0 is assumed.

4. The thermal boundary layer at $x = \delta_T(t)$ does not reach the opposite end of the steel slab; consequently, the steel wall may be considered to extend to infinity in the x-direction.

5. The initial steel temperature, T_o is sufficiently low so that steel melting will begin only after convection heating from the molten core debris raises the fuel crust-solid steel interface temperature, T_i, to the steel melting temperature, T_{mp}.

6. The initial effects of pure transient and conduction immediately following fuel-steel contact are ignored. Similarly, the initial effects of heat capacity (or temperature profile distortion) within the fuel crust are neglected. Thus it is assumed that the convective heat flux from the core debris is transmitted directly to the steel/core debris crust interface at $x = 0$, and therefore it is not necessary to evaluate the temperature field within the frozen core debris layer unless the crust thickness-time history is required. The relaxation time to quasi-steady heat transfer in the frozen layer of core material can be shown to be comparable to the time it takes the heat flux from the flowing core debris to exceed the conduction heat flux through the frozen layer Ref. [3.23]. In other words, the temperature profile in the debris layer becomes linear as the crust reaches maximum thickness and tends to remain close to linear throughout the crust melting period. From the results of the analysis reported in Ref. [3.24], we find that for the conditions of interest, the relaxation time for attainment of a steady state profile within the frozen debris crust is less than 5.0 s, which is negligible on the time scale of interest, $\sim$ 50.0 s.

We now apply the heat-balance integral method to determine how the melting propagates and how the temperature is distributed in the melted and unmelted portions of the steel slab. Although the heat balance integral method is particularly suited to solution of nonlinear phase change problems, it will first be employed to determine the temperature distribution in the

steel slab before melting starts. Subject to the above assumptions, we need only consider a semi-infinite steel slab occupying the space $x > 0$. Beginning at time $t = 0$, a constant heat flux q is applied to the interface $x = 0$; initially, the temperature of the slab is T_o. The temperature distribution must satisfy the heat balance:

$$q \cdot t = \rho_s c_s \int_0^{\delta_T} (T_s - T_o) dx \tag{3.15}$$

and the boundary condition

$$q = -k_s \left(\frac{\partial T_s}{\partial x} \right)_{x=0} \tag{3.16}$$

where the subscripts s refers to the properties of solid steel. We now assume a second-order polynominal for the temperature distribution $T_s(x,t)$:

$$\frac{T_s(x,t) - T_o}{T_i(t) - T_o} = \left(1 - \frac{x}{\delta_T} \right)^2 \tag{3.17}$$

It should be noted that this expression is consistent with the notion of a thermal wave thickness δ_T beyond which the effects of heat conduction are negligible. Combining the above three equations gives the solution

$$\delta_T = (6\alpha_s t)^{1/2} \tag{3.18}$$

$$T_i = T_o + \frac{1}{2} \frac{q}{k_s} (6\alpha_s t)^{1/2} \tag{3.19}$$

Setting the interface temperature T_i equal to the steel melting temperature T_{mp}, we obtain the time t_m when melting begins at the interface $x = 0$:

$$t_m = \frac{2}{3} k_s \rho_s c_s \left(\frac{T_{mp} - T_o}{q} \right)^2 \tag{3.20}$$

The thickness of the thermal boundary layer at this time is

$$\delta_T(t_m) = (6\alpha_s t_m)^{1/2} \tag{3.21}$$

At any instant after melting starts, the steel slab consists of distinct melt and solid portions. A macroscopic energy balance across the melted and unmelted material regions results in the expression

$$q(t - t_m) = \rho_s[L + c_s(T_{mp} - T_o)]\,\delta + \rho_m c_m \cdot \int_0^{\delta} (T_m - T_{mp})dx$$

$$+ \rho_s c_s \cdot \int_{\delta}^{\delta_T} (T_s - T_o)dx - \rho_s c_s \cdot \int_0^{\delta_T(t_m)} (T_s - T_o)dx \tag{3.22}$$

where the subscript m refers to the properties of the steel melt and L is the latent heat of fusion. This equation expresses the fact that during the melting period $(t-t_m)$, the heat flux from the stream of core debris supplied sufficient heat to raise the solid steel temperature from its initial value, T_o, to its melting temperature, T_{mp}, and to supply the latent heat of melting and the sensible heat in the solid and melt regions (minus the energy stored in the solid at time $(t-t_m)$). Another energy balance applied to the solid region $\delta < x < \delta_T$ requires that

$$\frac{d}{dt} \int_{\delta}^{\delta_T} (T - T_o)dx + (T_{mp} - t_o)\,\frac{d\delta}{dt} = \alpha_s \left(\frac{\delta T}{\delta x}\right)_{x=\delta} \tag{3.23}$$

The temperature distribution in the melt layer is assumed to be linear in x. Thus

$$\frac{T_m(x,t) - T_{mp}}{T_i(t) - T_{mp}} = 1 - \frac{x}{\delta} \tag{3.24}$$

During the melting period, the temperature distribution in the solid steel is given by

$$\frac{T_s(x,t) - T_o}{T_{mp} - T_o} = \left(\frac{\delta_T - x}{\delta_T - \delta}\right)^2 \tag{3.25}$$

This leads to the following set of equations so that upon substitution:

$$q(t - t_m) = \rho_s[L + c_s(T_{mp} - T_o)]\,\delta + \frac{1}{2}\rho_m c_m q\delta^2/k_m$$

$$+ \frac{1}{3}\rho_s c_s(\delta_T - \delta)(T_{mp} - T_o) - \frac{1}{3}\rho_s c_s \delta_T(t_m)(T_{mp} - T_o) \qquad (3.26)$$

$$\frac{1}{3}\frac{d}{dt}(\delta_T - \delta) + \frac{d\delta}{dt} = \frac{2\alpha_s}{\delta_T - \delta} \qquad (3.27)$$

$$T(t) - T_{mp} = \frac{\delta q}{k_m} \qquad (3.28)$$

for the determination of $\delta(t)$, $\delta_T(t)$ and $T_i(t)$.

Before proceeding further, it is expedient to nondimensionalize the equations. The new variables are defined as follows

$$\tau = \frac{t}{t}; \qquad \Delta = \frac{\delta}{\delta(t_m)}; \qquad \Delta_T = \frac{\delta_T}{\delta(t_m)}; \qquad \theta_i = \frac{T_i - T_{mp}}{T_{mp} - T_o}$$

The following parameters are introduced:

$$\beta = \frac{L}{c_s(T_{mp} - T_o)}; \qquad \gamma = \frac{\alpha_s}{\alpha_m}$$

In terms of the dimensionless quantities introduced in the foregoing, the previously defined set of equations takes the form

$$\tau = 3(\beta + 1)\,\Delta + 3\gamma\Delta^2 + \Delta_T \qquad (3.29)$$

$$\frac{d\Delta_T}{d\tau} + 3\frac{d\Delta}{d\tau} = \frac{1}{\Delta_T} \qquad (3.30)$$

$$\theta_i = 2 \frac{k_s}{k_m} \Delta \tag{3.31}$$

These equations can be solved by numerical integration. However, if the right-hand side of the first equation were free of the term $3\gamma\Delta^2$, then the equations have the simple inverted solution for $\Delta_T(\tau)$,

$$\tau = 1 + \beta(\beta + 1)\ln\left(\frac{\beta}{(\beta + 1) - \Delta_T}\right) - \beta(\Delta_T - 1) \tag{3.32}$$

which is valid for thin melt layers, $\Delta << (1 + \beta)/\lambda$, or, equivalently, negligible heat capacity in the steel melt layer.

Figure 3.7 shows the dimensionless thermal boundary layer thickness, Δ_T, the dimensionless melt-layer thickness, Δ, and the dimensionless interface temperature, θ_i, for $\beta = 0.34$. This value of β corresponds to an initial steel temperature $T_o = 300^oC$. Note that the thickness of the thermal wave asymptotically approaches a constant value and, in turn, the steel melt layer becomes a linear function of time.

Using the results of the analysis, it is interesting to examine the thermal response of a steel wall initially at 300^oC to attack by a 30 cm diameter stream of degraded core material superheated 200^oC above its fusion temperature and flowing at a velocity u = 440 cm/s. Inserting the above values into the heat flux expression, we find $q/_A = 2150$ Kw/m^2. Solution of the previously defined equations then reveal that the steel slab will begin to melt at $t_m = 36.0$ sec and the thermal boundary layer thickness at this time $\delta_T(t_m) = 3.74$ cm. The temperature distribution in the slab at or before incipient melting can then be determined. Figure 3.8 presents the spatial variation of the temperature at $t = t_m$. Before melting begins, a mathematically exact relationship for the temperature distribution can be found in Ref. [3.23] and displayed in Figure 3.8 for $t = t_m$. a comparison of the integral method with the exact solution reveals reasonable agreement for this special case. By means of Figure 3.7 and the appropriate equation, it is possible to determine the temperature at any point of the steel slab at any instant after melting starts, providing Δ remains small and/or the fuel

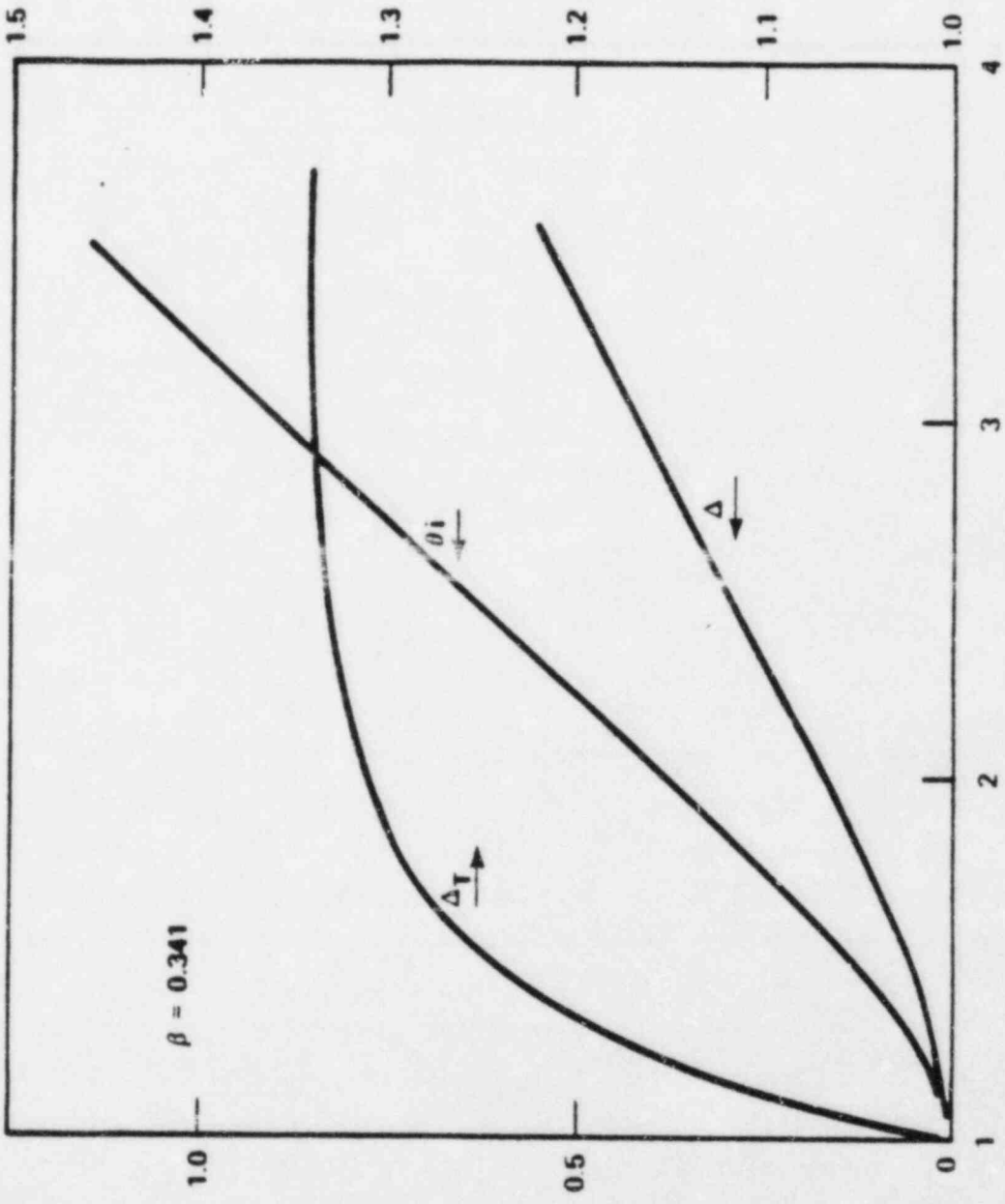

Fig. 3.7 Δ_T, Δ, θ_i versus time for $\beta = 0.34$.

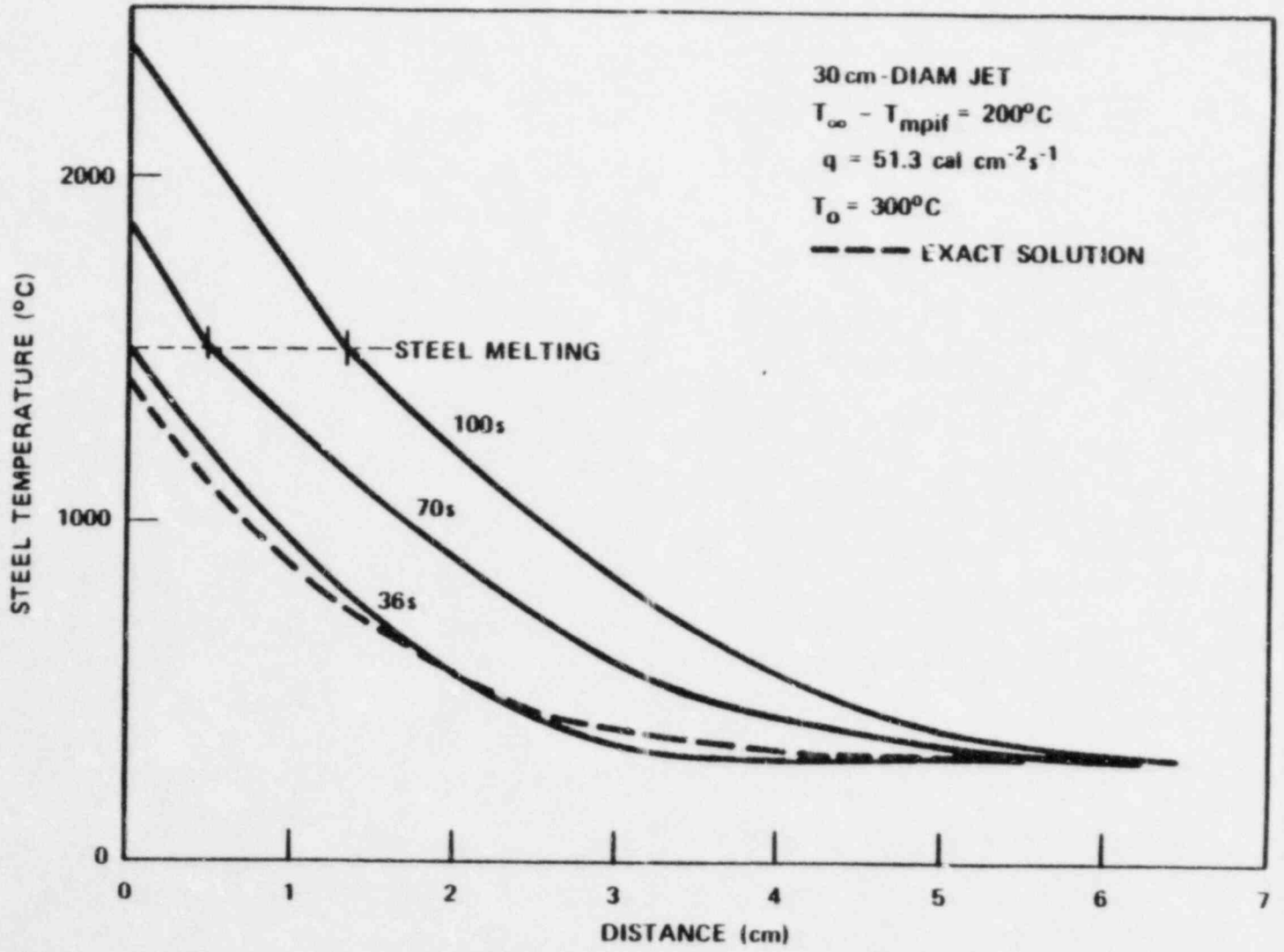

Fig. 3.8 Effect of time on temperature profile in melting steel wall.

crust does not disappear via remelting, (i.e., $T_i < T_{mp,f}$). In Figure 3.8, two temperature distributions are shown within the steel melt and the solid steel region at t = 70 s, and t = 100 s.

Due to the rapid heating and localized melting of the reactor vessel wall as the degraded core material flows into the lower plenum, the steel will achieve temperatures of 1000°C or greater at depths up to 2 cm in about one minute, i.e., the approximate draining time of the material. At such temperatures, there would be little strength left in this steel and, as shown in Figs. 3.9 and 3.10 this is the approximate depth of the weld material anchoring the in-core instrument penetrations for both BWR and PWR systems. Since the weld material would be subject to essentially the same thermal attack as the vessel wall, for the spectrum of sequences in which a significant pressure remains in the primary system as well as those which have a depressurized primary system, these penetrations could be expected to fail during, or within minutes after, the core debris pours into the bottom head.

This analytical information has considered the effects of a molten core stream pouring into the lower plenum, a behavior that was postulated to result from debris accumulation on the core support plate. As such, it is viewed as a conservative representation of the process whereby core debris is transported from the original core boundaries into the lower plenum and eventually outside of the reactor pressure vessel. In the evaluation presented above, only the limited depth welds for the penetrations were considered, but the actual design of the in-core instrument penetrations could also have a significant effect on the material migration.

Boiling Water Reactors have a forest of penetrations in the lower head because the control rods are driven from the bottom and the in-core instrumentation also enters the vessel from the bottom. For the larger systems there are 175 control rods, each with its own penetration, several additional penetrations for in-core neutron flux monitors, and a reactor vessel drain. Figure 3.9 illustrates the general configuration utilized for both control rod penetrations and in-core instrument tube penetrations. In both cases the weld area would be subject to a three-dimensional thermal attack in the presence of any significant accumulation of degraded core

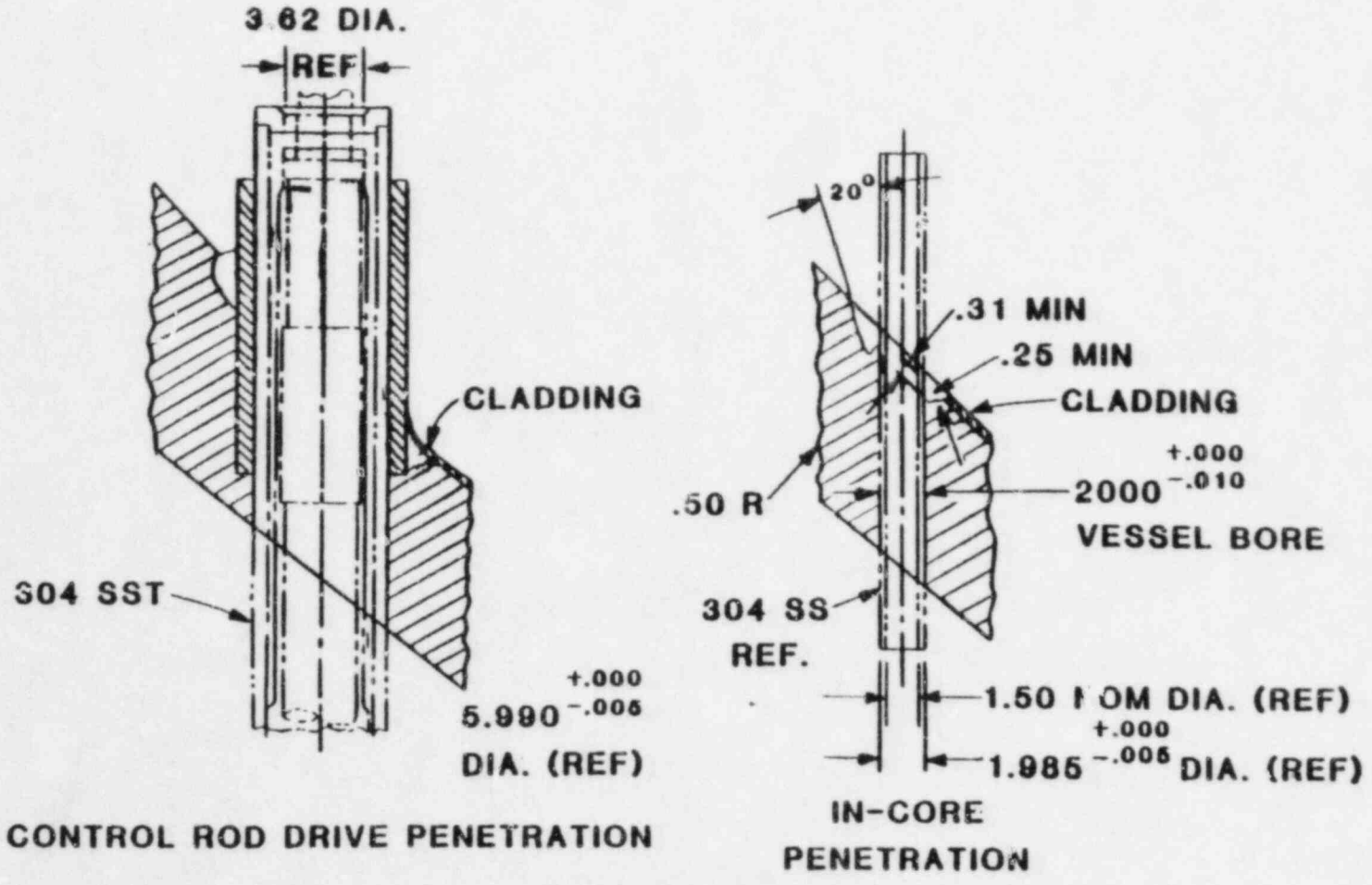

Fig. 3.9 Typical penetration welds for BWR control rod drives and instrumentation.

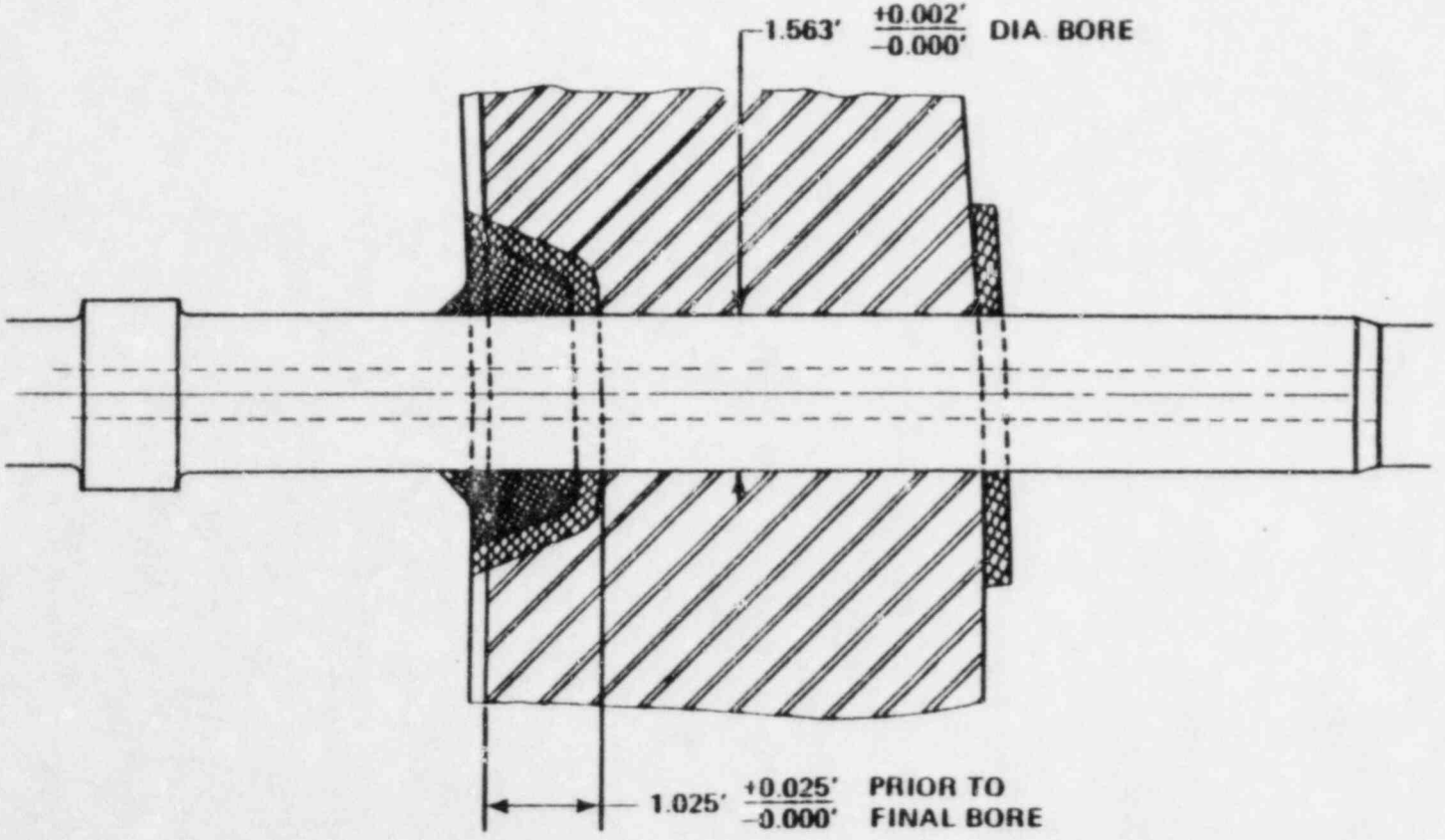

Fig. 3.10 Typical instrumentation nozzle - vessel weld for a PWR system.

material. Because of the large number of penetrations and the three-dimensional type of melting attack that these would experience, as opposed to the essentially one-dimensional melting at the vessel wall, these penetrations would be the first element of the primary system pressure boundary to fail, particularly for meltdown scenarios in which there is considerable pressure within the reactor vessel. In the event that a control rod drive support is melted through and the mechanism is ejected, the resulting vessel breach would be approximately 10 cm in diameter.

For the Zion system, the 58 in-core penetrations are essentially continuous tubing from the seal table, located in the containment building above the top of the reactor vessel, down through the instrument tunnel and reactor cavity, up through the reactor vessel and through the entire core. The in-core instruments, of which there are only five, are inserted into the core through these tubes and are indexed by a switching device so that the flux distribution within the core can be mapped. As a result, at least 53 of these positions are always open, and generally all 58 positions are open. The central hole, through which the probes are inserted, is at the containment atmosphere. Consequently, when these tubes fail, a potential path is available to duct material from the reactor core into the containment. For these particular probes, the design is a double tube configuration with the central passage for the probe and water, at the primary system pressure, in the annular gap between the two tubes. As a result the analysis of the flow of degraded material through such holes when they become available is quite complex and requires a detailed resolution of the distribution of material within the core as well as the material temperature. Therefore, such details have not been included in the analysis, and the accumulation of core debris on the support structure and its subsequent collapse has been used to evaluate the behavior within the lower plenum.

Another feature contributing to the failure of the penetrations would be the "fin effect" of tube stubs surrounded by core debris. Given the accumulation of material in the lower plenum, the molten debris would freeze as it contacted the various steel structures in the plenum. As a result, the reactor vessel, the lower support structure, and the remnants of the in-core instrument tubes would be initially covered by a crust of core debris. In the

absence of a sustained molten stream and ablation as discussed above, the temperature of the weld material around the penetrations would increase faster than the vessel wall since the stainless steel penetrations stubs would conduct energy from the molten pool into the welds. Consequently, these limited penetration junctions would be the first part of the reactor vessel pressure boundary to fail even in the absence of a strong ablative attack by the molten core.

Given that an in-core instrument guide tube is melted through and ejected, Figure 3.11 schematically illustrates this configuration in which the molten core material flows through this breach under the driving pressure of the overlying steam/gas mixture. The velocity of this discharge can be estimated by Bernoulli's equation where the core material is assumed to all be liquid:

$$U = \left[\frac{2(P_o - P_a)}{\rho_F}\right]^{1/2} \tag{3.33}$$

For the depressurized cases (large break LOCA sequences), the driving pressure comes from the static head ($\rho_f gh$) which produces a velocity equal to $U = (2gh)^{1/2}$.

The pressures P_o and P_a represent the vessel and primary containment conditions respectively and ρ_F is the density of the molten core material. As the high temperature liquid flows through the breach, it will contact comparatively cold steel in the process. The interface temperature developed upon contact μ given by

$$T = \frac{T_F + T_s \left[\frac{k_s \rho_s c_s}{k_F \rho_F c_F}\right]^{1/2}}{1 + \left[\frac{k_s \rho_s c_s}{k_F \rho_F c_F}\right]^{1/2}} \tag{3.34}$$

where T_F and T_s are the initial temperatures of the core material and steel and k_F, ρ_F, c_F, k_s, ρ_s, and c_s are the thermal conductivity,

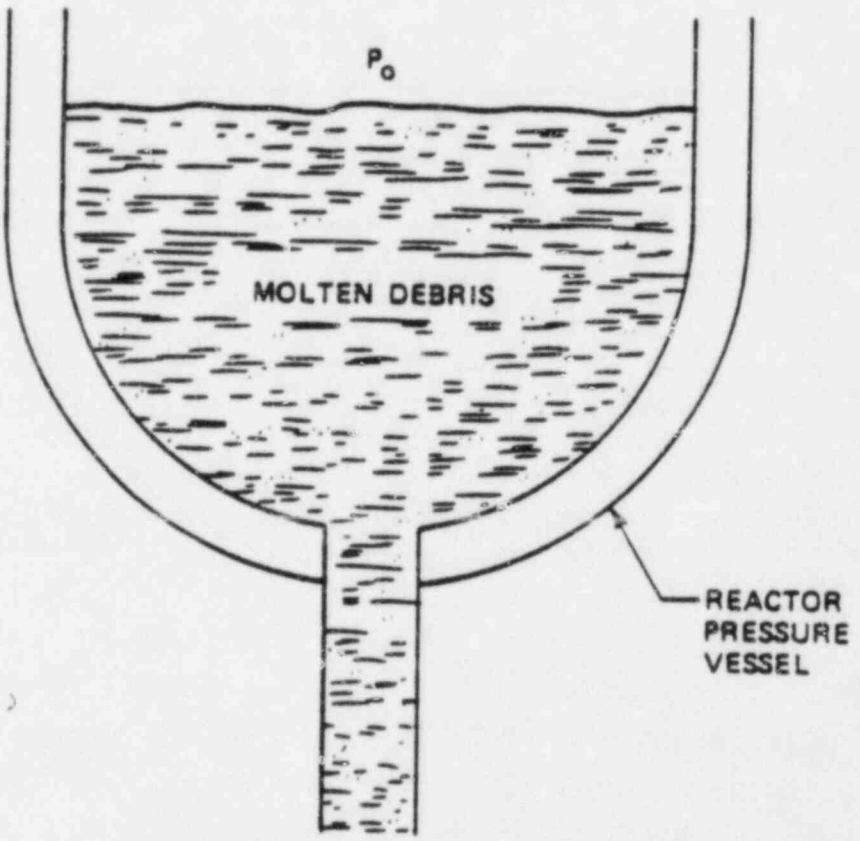

Fig. 3.11 Ejection of core debris from the vessel following failure of an instrumentation nozzle.

density and specific heat of the core material and steel, respectively. For typical conditions of interest ($T_F \sim 2200^oK$ and $T_s \sim 250^oC$), this interface temperature is well below the melting points of both the steel and the fuel/zirconium oxide mixture. Consequently, the molten material freezes upon contact forming a thin crust of material as shown in Fig. 3.12 which tends to insulate the steel from the molten stream. The solid crust receives energy from the convective stream as given by the expression

$$q = hA\ (T_F - T_{m,F}) \tag{3.35}$$

where h is the convective heat transfer coefficient, A is the surface area of the crust, and $T_{m,F}$ is the melting point of the fuel/zirconium oxide mixture. Using Reynolds' analogy, the heat transfer coefficient can be related to velocity by

$$h = f\,\frac{\rho_F c_F U}{2} \tag{3.36}$$

where f is the dimensionless friction factor (f = 0.005). If the vessel pressure is assumed to be 17.2 MPa (PWR system), the discharge velocity would be about 70 m/sec, and the corresponding heat transfer coefficient would be approximately 735 $kw/m^{2o}C$. For the highest pressure in a BWR system, 7 MPa, the discharge velocity would be 43 m/sec and the heat transfer coefficient would be about 450 $kw/m^2\ ^oC$. The resulting heat flux must be transferred through the crust and into the steel. If the crust is too thick to transmit the required energy, it will remelt until it is sufficiently thin; if the steel cannot absorb the imposed heat flux it will also melt. The time required for thermal boundary layer development within the steel to the point where it can no longer remain solid can be estimated from the error function solution for an instantaneous change of surface temperature where the interface temperature is assumed to be the steel melting point:

$$h(T_F - T_{F,m}) = k_s(T_{s,m} - T_s)/\left(\pi\alpha_s\theta\right)^{1/2} \tag{3.37}$$

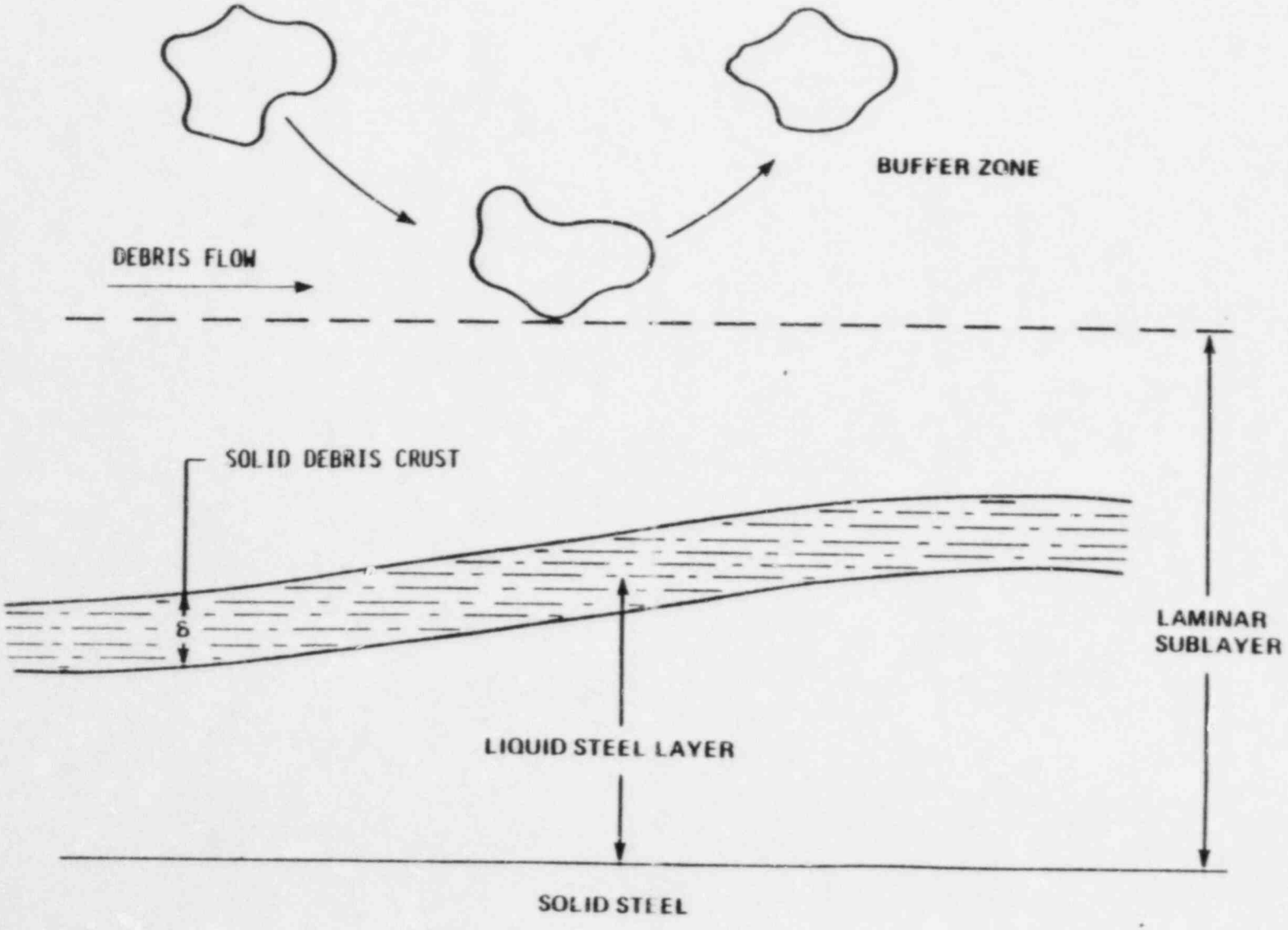

Fig. 3.12 Crust formation.

The steel thermal diffusivity is designated by α_s, and the time interval by θ. Thus, the expression for the required time is obtained by rearranging the above equation to

$$\theta = [k_s(T_{s,m} - T_s)]^2/\pi\alpha_s\,[h(T_F - T_{F,m})]^2 \tag{3.38}$$

For the conditions outlined above, the time for the onset of steel melting is 0.04 seconds, which is quite short compared to the vessel discharge time. Consequently, even with the presence of an insulating crust, the steel substrate will be quickly driven to melting because of the high heat flux imposed by the convective stream.

Melting of the steel substrate below the fuel crust will jeopardize the stability of this crust. The thickness of this crust can be estimated from

$$\delta = k_F(T_{F,m} - T_{s,m})/h(T_F - T_{F,m}) \tag{3.39}$$

For the temperatures and flow condition listed above, the fuel crust would only be approximately 66 μm thick which would have negligible strength; this is in agreement with the stability arguments presented by Epstein, et. al. Ref. [3.25]. Therefore, once steel melting is initiated, the thin crust of core material would be continually formed, destroyed, and reformed. The only significant implication of the crust would be the limitation that it provides in the energy transfer process, i.e., it determines the driving temperature difference for the convective heat transfer from the molten stream.

As a result of the behavior described above, the steel will be melted very shortly after the penetration is established and the convective stream will continually attack the reactor vessel wall. This ablation process will enlarge the original failure size at a rate which can be obtained by equating the convective energy transfer to the energy required to melt the steel:

$$hA_s(T_F - T_{F,m}) = \rho_s A_s\,[c_s(T_{s,m} - T_s) + \gamma_s]\,\frac{dr}{dt} \tag{3.40}$$

The derivative dr/dt is the growth rate of the breach radius, A_s is the exposed cylindrical surface area of the steel, and γ_s is the heat of fusion of the steel. From this expression, the growth rate of the breach is a constant and is given by

$$\frac{dr}{dt} = \frac{h(T_F - T_{F,m})}{\rho_s(c_s(T_{s,m} - T_s) + \gamma_s)} = B \qquad (3.41)$$

As a result of this ablation, the available flow area through which the molten material can be expelled from the vessel will increase substantially during the core ejection stage.

With the configuration illustrated in Fig. 3.11, the incompressible molten material is forced out of the vessel by the high pressure, compressible gas/steam mixture above the core debris for the transient and small LOCA sequences and by the static head of the molten pool in the large break LOCA cases. Since, for the high pressure cases, the volume occupied by the molten core is small compared to the initial volume of the gas/steam mixture, the vessel pressure and, therefore, the discharge velocity, will remain essentially constant during the expulsion process. Thus, the exhaust flow can be described by

$$\dot{m} = \rho_F A_c U \qquad (3.42)$$

where

$$A_c = \pi r^2 = \pi(r_o + Bt)^2 \qquad (3.43)$$

For postulated large break scenarios, the discharge velocity will decay with decreasing pool depth as given by $U = (2gh)^{1/2}$ where g is the acceleration of gravity and h is the instantaneous pool depth. Since this is a comparatively weak dependence of depth, in these analyses, the velocity is assumed to remain constant at the initial value.

The quantity r_o is the radius of the initial vessel failure. To express the total mass discharged at any point in time, one only has to integrate with respect to time:

$$\Delta m = \rho_F U \pi \int_0^t (r_o + Bt)^2 \, dt = \rho_F U \pi \left[r_o^2 t + r_o B t^2 + \frac{B^2 t^3}{3} \right] \qquad (3.44)$$

This mass discharged as a function of time is graphically illustrated for typical PWR scenarios in Figs. 3.13-3.15: Fig. 3.13 for the large break sequences, in Fig. 3.14 for the small break cases and Fig. 3.15 for the transient cases. In addition, Fig. 3.16 illustrates a similar BWR calculation for an assumed failure of a control rod drive penetration and a vessel pressure of 7 MPa. It is apparent from the functional form that the flow rate is continually increasing because of the linear growth of the radius with time. For all the PWR sequences shown, the final vessel break is almost the same, and the breach diameter is less than one-tenth of the vessel diameter. This, and the relative time scales for complete discharge for the various transients ($\sim$ 4 seconds for the high pressure cases versus almost 80 seconds for the large LOCA sequences), are the principle results developed by this analysis. Subsequent discharge of the follow-on gas/steam mixture for the elevated pressure cases and the resultant containment behavior should be calculated based upon this vessel breach size.

Given the vessel failure mechanism discussed above and the size of the resultant breach in the vessel lower head, one must then evaluate the progression of the degraded core material into the reactor cavity and the containment using molten core material discharge rates and conditions as calculated from this failure mechanism as well as the behavior and influence of the follow-on steam/gas mixture which blows down through the vessel breach. These phenomena must be addressed in terms of their influence on the ultimate disposition and coolability of the molten core debris.

Vessel failure for vessels without lower head penetrations have also been considered in the IDCOR program. These analyses are included as Appendix A to this report.

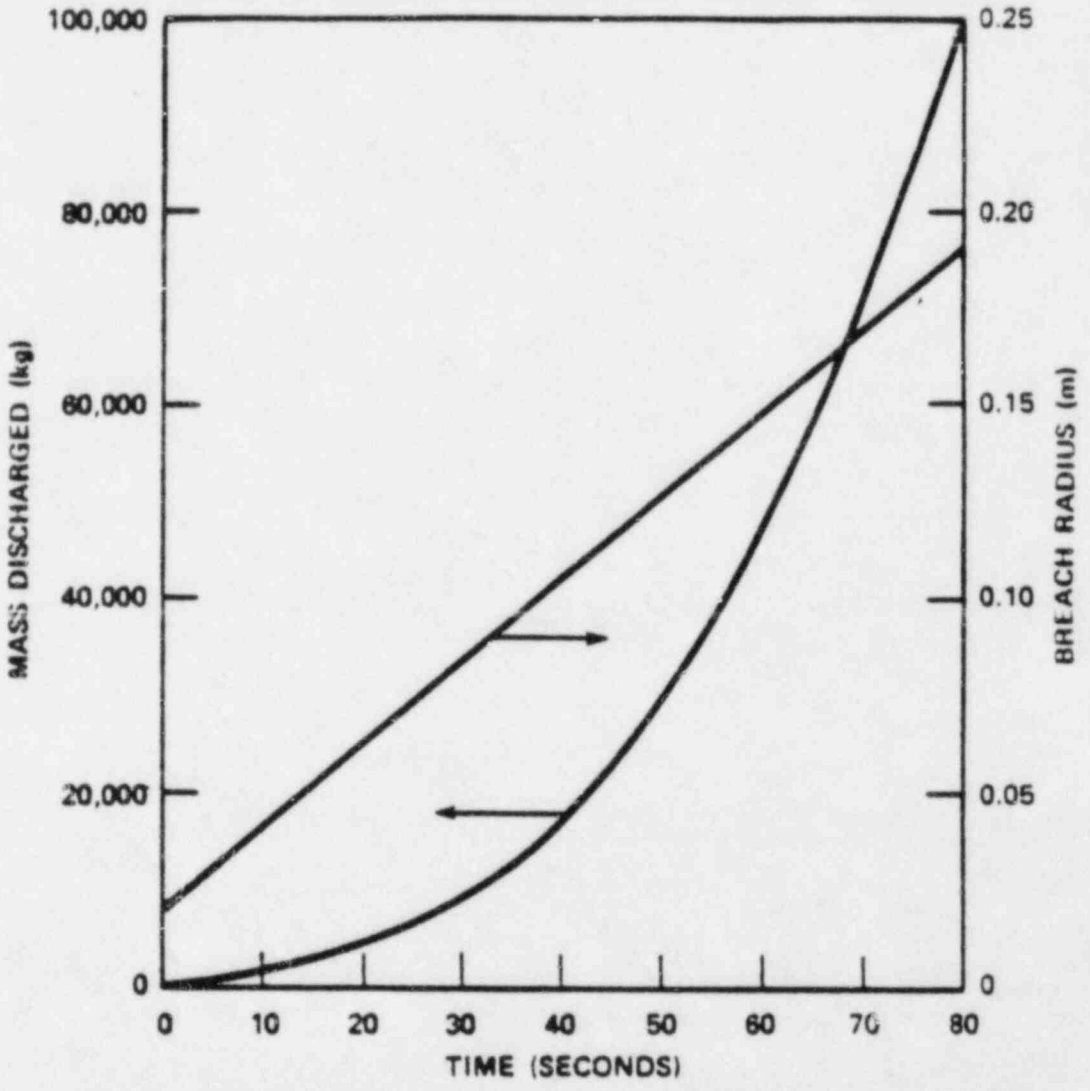

Fig. 3.13 Mass discharged as a function of time for a large LOCA.

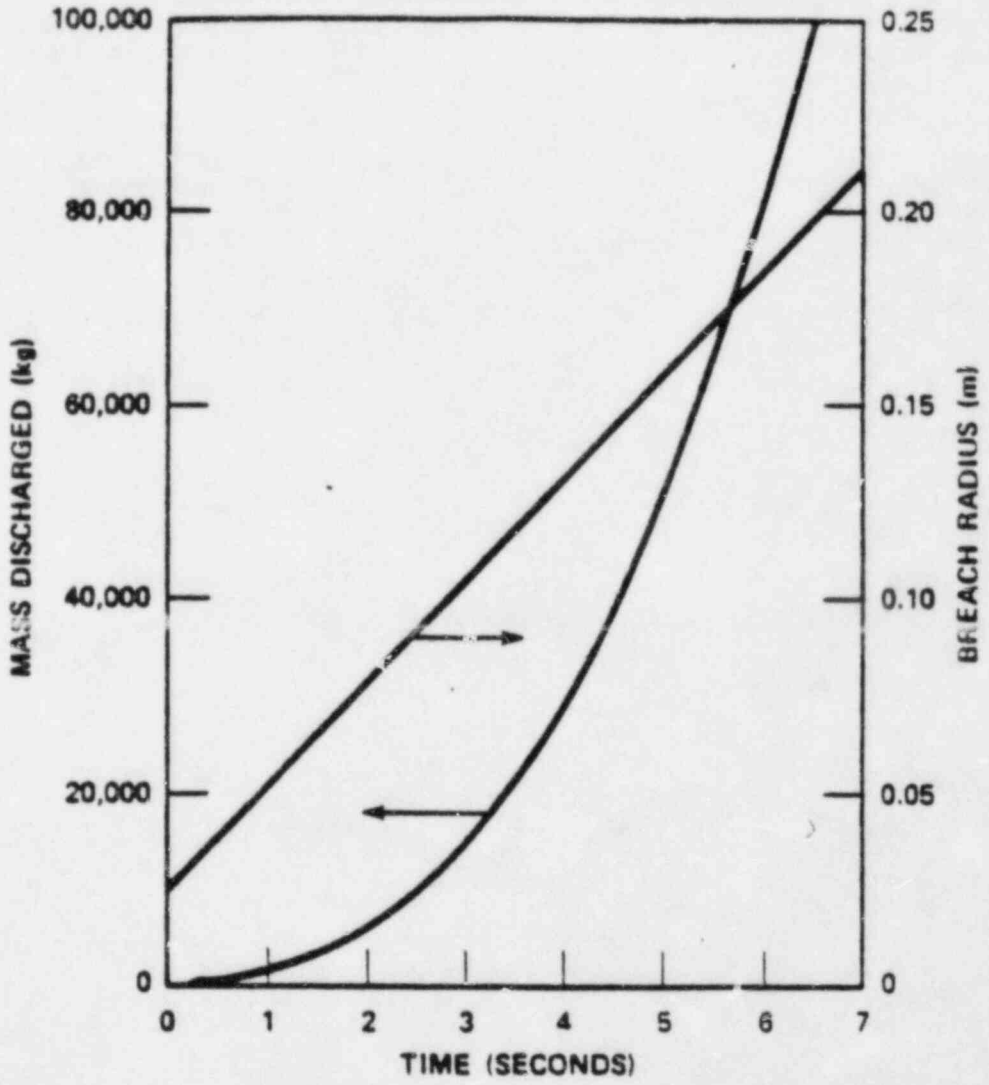

Fig. 3.14 Mass discharged as a function of time for a small LOCA.

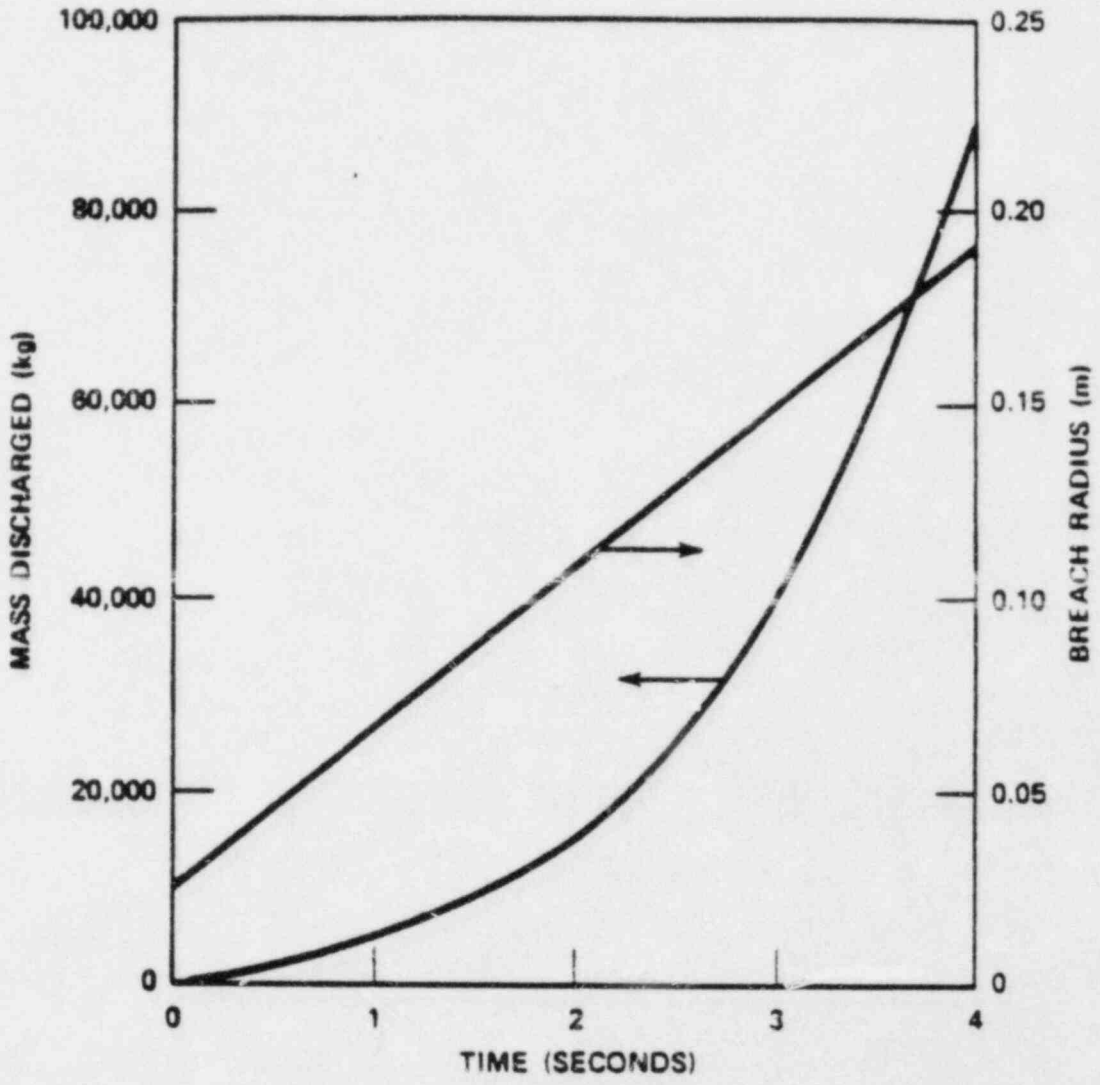

Fig. 3.15 Mass discharged as a function of time for a transient case.

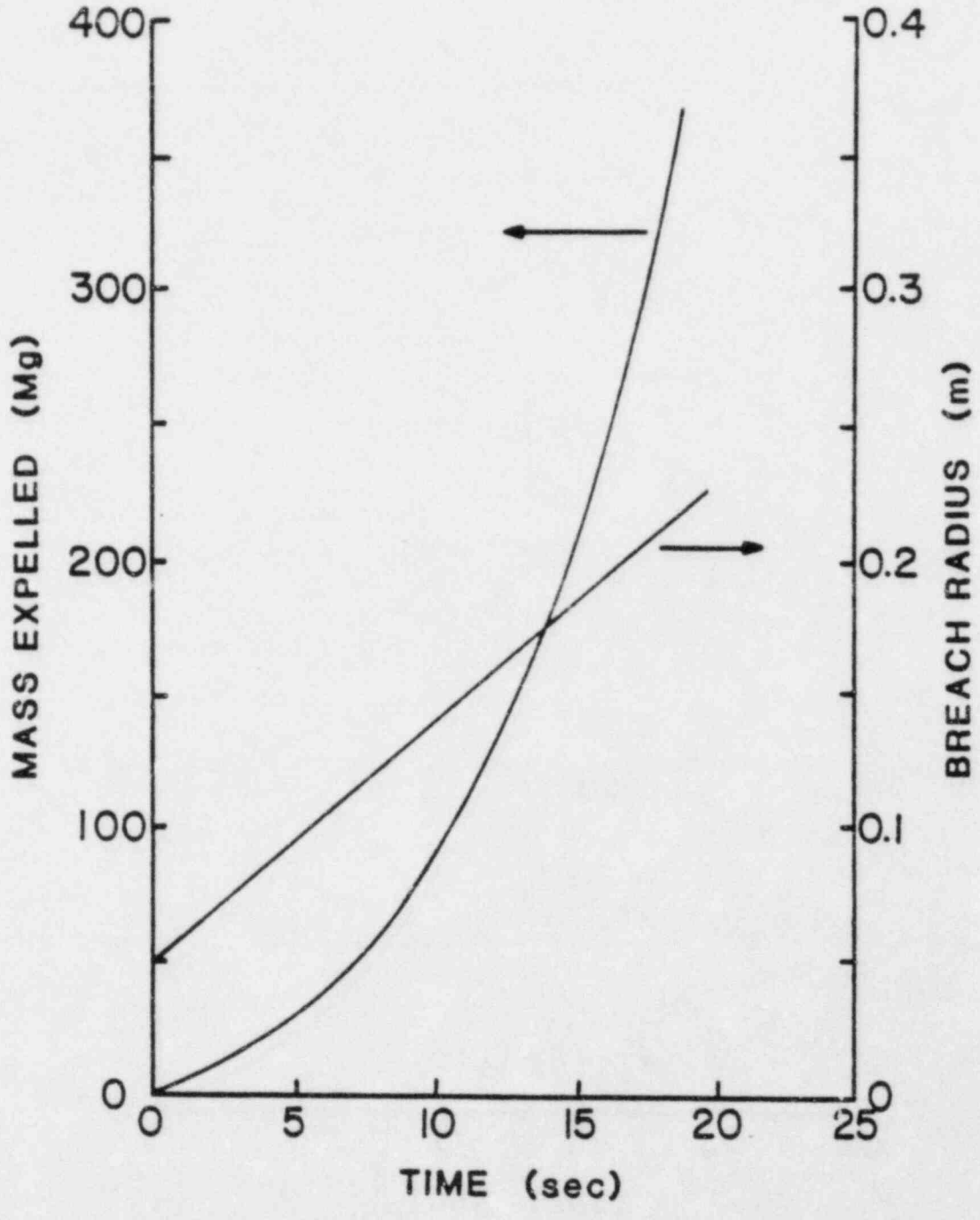

Fig. 3.16 BWR calculated mass discharged and breach radius verse time.

3.4 Debris Dispersal

3.4.1 Hydraulic Jump

For those postulated severe accident scenarios in which a substantial pressure is available within the primary system at the time of vessel failure, the high velocity discharge of molten core debris into the reactor cavity/instrument tunnel/pedestal region would have a pronounced influence on the dynamic configuration of the accumulated debris. As discussed previously, such hypothetical accident initiators could be a transient or a small break LOCA. A large break LOCA is not a part of this evaluation since the discharge rate would only be that resulting from the static head, which is a considerably lower velocity than those typified by the other two accident initiators.

As the material is discharged from the vessel, the high velocity jet would impinge on the concrete working slab and spread as illustrated for a PWR reactor cavity in Figure 3.17, while it is also attacking the concrete. Initially the spreading flow would be radial, but given the typical personnel access path of reactor cavity/instrument tunnel/pedestal regions, the flow would quickly spread to the reactor cavity walls and then be directed through the instrument tunnel or personnel passageway should this be available. In the Zion configuration, for example, the instrument tunnel is approximately two meters wide and four meters high. As shown in Fig. 3.17 this configuration runs horizontally for a distance of about seven meters and then runs upward at a sharp angle to the containment floor about eight meters above. As the flow is directed into this instrument tunnel region, the flow velocities would be sizable, i.e. for an assumed depth of 0.1 m, the material velocity at the end of a transient accident sequence could be over 17 m/sec.

As the molten core debris flows through the instrument tunnel, the material momentum would be decreasing due to viscous shear in the melt. The magnitude of the viscous dissipation can be estimated from a turbulent boundary layer formulation. The shear stress varies with the Reynolds number which is given by

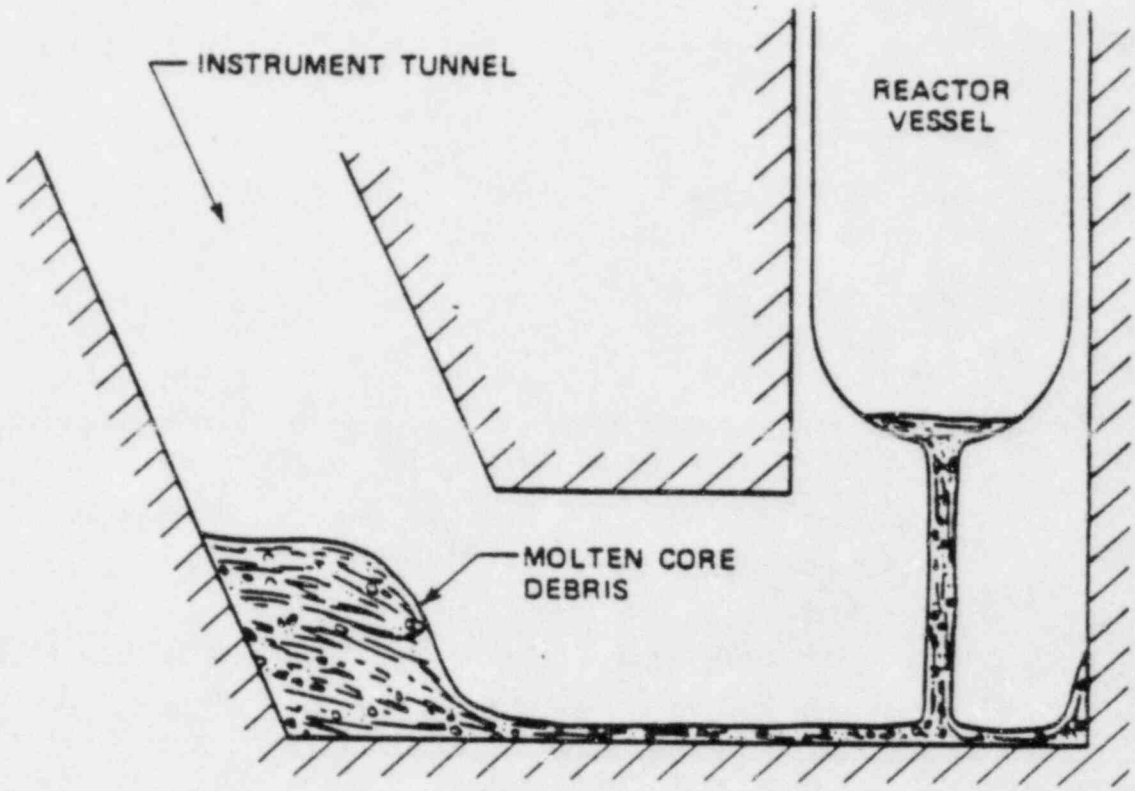

Fig. 3.17 Molten core debris configuration at the end of the liquid discharge.

$$N_{Re} = \frac{Ux}{\gamma_F} \tag{3.45}$$

where γ_F is the debris kinematic viscosity and x is the distance along the surface in the direction of flow. For this order of magnitude representation, we will use a value of 1 m which will overestimate the frictional term. Using a value of 5.7×10^{-7} m^2/sec for the kinematic viscosity as recommended in Ref. [3.26] yields a Reynolds number of 3×10^7 and the turbulent drag coefficient corresponding to this value is about 0.0025. The shear force on an area 7 m long and of unit width is

$$F = 0.0025\ (7)\ \frac{\rho_F U^2}{2} \approx 17{,}700\ N \tag{3.46}$$

for a velocity of 17 m/sec. This can be compared to momentum of the stream

$$F_M = \dot{m}U = \rho_F\ (0.1)\ U^2 \approx 202{,}000\ N \tag{3.47}$$

which shows that the momentum is at least an order of magnitude larger than the shear force at the wall. As a result, only the potential flow characteristics need to be considered in the order of magnitude assessment.

Given such high velocities, the high density flowing stream would experience a hydraulic jump somewhere in the instrument tunnel region for this reference plant design because of the steeply inclined shaft at the end of the horizontal section. Across a hydraulic jump, the energy is redistributed from a high velocity, low static head state to one of a low velocity, high static head. This behavior is illustrated in Fig. 3.17 for a flow stream of depth y, and velocity U_1 decelerating to a velocity U_2 with increased depth y_2. Equating the forces and momentum change between the two states results in

$$\int_0^{y_1} b\rho_f g y dy + \dot{m}_\ell U_1 = \int_0^{y_2} b\rho_F g y dy + \dot{m}_\ell U_2 \tag{3.48}$$

where $\dot{m}_\ell$ is the liquid flow rate and b is the width of the instrument tunnel. Carrying out the integration gives

$$\frac{gy_1^2}{2} + y_1U_1^2 = \frac{gy_2^2}{2} + y_2U_2^2 \tag{3.49}$$

and if the continuity relationship is used to eliminate the velocity U_2, the expression can be written as

$$\frac{gy_1^2}{2} + U_1^2y_1\,(1 - y_1/y_2) = \frac{gy_2^2}{2} \tag{3.50}$$

Solving for the depth y_2 in terms of y_1 yields

$$y_2 = \left[y_1^2 + \frac{2U_1^2y_1}{g}\,(1 - y_1/y_2)\right]^{1/2} \tag{3.51}$$

and if y_1/y_2 is much less than unity, the expression can be approximated by

$$y_2 = \left[y_1^2 + \frac{2U_1^2y_1}{g}\right]^{1/2} \tag{3.52}$$

In general, for the conditions of interest, the first term inside the brackets is small compared to the second term, thus the equation can be further simplified to

$$y_2 = U_1\left(\frac{2y_1}{g}\right)^{1/2} \tag{3.53}$$

and since the flow rate in the instrument tunnel ($\dot{m}_\ell$) is given as

$$\dot{m}_\ell = \rho_F\, by_1U_1 \tag{3.54}$$

the equation for the hydraulic jump height can be expressed in terms of the imposed liquid flow and the initial height (y_1):

$$y_2 = \frac{\dot{m}_\ell}{b\rho_F}\left(\frac{2}{gy_1}\right)^{1/2} \tag{3.55}$$

As illustrated, the jump height only varies as the square root of the initial height.

These calculations show the jump height to be relatively insensitive to the initial depth of the jet flow. Consequently, to provide comparative values for this behavior in the particular accident initiators of interest, an initial depth of 0.1 m will be assumed and the flow rate (and thus the velocity) will be determined by the material discharge rate at the end of the discharge interval for the core debris.

For the case in which y_1 would be 0.1 m and U_1 would be 17 m/sec (the transient case), the value for y_2 would be 2.4 m, i.e., the hydraulic jump would be substantial and the above assumption of y_1/y_2 being small compared to unity would be justified. If the approximate analysis is compared to the small break case, at the end of the core debris discharge interval the vessel breach area would be about 0.05 m^2 and the velocity would be 45 m/sec (reactor vessel pressure of 7 MPa). The material velocity in the instrument tunnel for an assumed depth of 0.1 m would be 11 m/sec and the value of y_2 would be 1.6 m, in which case y_1/y_2 would again be small compared to unity.

As a result of the dynamic forces inherent in the high velocity discharge of the molten core debris in the transient and small break scenarios, the configuration of the debris at the end of the liquid discharge interval would be similar to that illustrated in Figure 3.17. It is this configuration which then responds to the subsequent high velocity gaseous discharge of a steam/hydrogen mixture through the breach in the reactor pressure vessel. The effects of this discharge will be analyzed in the following subsection.

This dynamic debris configuration could be very influential in determining the dispersive capabilities in the BWR containment designs. For example, such an initial configuration would provide for a more rapid and

uniform material removal in a Mark III containment with a "sunken" pedestal geometry.

In the case of the large break LOCA, the dynamic behavior of the liquid discharge, while qualitatively the same, is correspondingly reduced in magnitude. For instance, with an assumed discharge velocity of 4 m/sec, a vessel breach area of 0.05 m^2, and a depth (y_1) in the instrument tunnel of 0.1 m, the depth after the hydraulic jump would be 0.17 m. This is a much smaller effect, but the most important difference is the depressurized state of the primary system, i.e., there would be no subsequent behavior to substantially change the pool configuration. Therefore, the hydraulic jump would subside after the liquid discharge interval.

3.4.2 Steam/Hydrogen Blowdown from the Primary System

At this juncture in the scenario (i.e., at vessel failure), there would be a major difference between the ex-vessel event progression for the large break LOCA's versus the small break LOCA's and transients because of the elevated primary system pressure in the latter two types of sequences. Consequently, this subsection only relates (in a physical manner) to small break and transient sequences.

Following the release of degraded core material from the reactor pressure vessel, the steam/hydrogen mixture will be discharged from the system for those defined accident scenarios in which the primary system has remained at an elevated pressure. For such sequences this represents a large volume of gas, with a pressure potentially equal to or slightly above the nominal operating pressure, being discharged through a vessel breach which could be up to 40 cm in diameter. For PWR small break LOCA sequences and BWR transient sequences, a characteristic primary system pressure at the time of the gaseous discharge could be 7 MPa. The discharge of this vapor/gas mixture would be determined by the compressible flow characteristics of the mixture with the primary system pressure greater than approximately twice the containment pressure. The resultant dynamics of the process must be based on this compressible flow behavior, which can be treated as being isothermal in order to simplify the calculations for these illustrative examples. This also provides a representation of heat transferred to the gas as it attempts to

expand and cool below the temperatures of the surrounding structural components. The sonic velocity (c) corresponding to an isothermal discharge of a gaseous mixture can be expressed by

$$c = (RT)^{1/2} \tag{3.56}$$

where R is the gas constant for the specific mixture and T is the temperature of the mixture, which was taken to be 600°K in these calculations. As the high velocity stream passes through the reactor vessel breach, it will have a static pressure about 60 percent of the primary system pressure at any instant. (The critical pressure ratio for an isothermal expansion is 0.6.) since the gas mixture pressure is substantially above the containment pressure, additional acceleration will occur in the unbounded, single phase, compressible jet. The asymptotic velocity (U_a) achieved by this unbounded expansion is given by Ref. [3.27]

$$U_a = \frac{P_t - P_a}{G_t} + U_t \tag{3.57}$$

where U_t is the isothermal velocity of the throat and is equal to the sonic velocity (c). In this expression, G_t is the flow rate per unit area at the throat location, P_t is the pressure at the throat, and P_a is the pressure in the reactor cavity at any instant in time. Assuming an equal volume mixture of steam and hydrogen, the isothermal velocity at the throat would be about 700 m/s. Assuming that the primary system pressure at the time of initiation for the steam/hydrogen release is 15 MPa (PWR transient), the throat pressure in the breach of the reactor vessel would be 9 MPa, the gas density at the vessel breach would be 18 kg/m^3 which results in a mass flow rate per unit area of approximately 12,770 kg/m^2-sec. Assuming the containment atmosphere at this time is 0.1 MPa, the resulting supersonic velocity for the unbounded expansion of the single phase, critical flow jet is approximately 1400 m/sec for both types of accident initiators. This supersonic velocity jet is directed towards the pool of degraded core material which has accumulated in the reactor cavity or pedestal region. It is the stagnation of this supersonic jet which would have a major influence on the ultimate distribution

of accumulated degraded core material. The stagnation pressure P_o for this supersonic gaseous jet can be calculated for an assumed isothermal process as

$$-\int_{p_a}^{p_o} v\,dp = \int_{u_a}^{o} u\,du \tag{3.58}$$

For the PWR small break initiator or the BWR transient accident scenarios, the primary system pressure at reactor vessel failure could typically be 7 MPa, which would produce a pressure at the breach of 4.2 MPa. The resulting flow rate for these conditions would be approximately 6000 kg/sec-m^2.

3.4.3 Removal of Core Debris From Reactor Cavity Region

In conjunction with the dynamic considerations discussed above for the molten core debris, the subsequent discharge of high pressure steam and hydrogen would have a substantial influence on the ultimate disposition of the degraded core material. Before considering the ultimate effects, it is instructive to consider the initial influence of the high pressure gaseous discharge even if the hydraulic jump configuration discussed previously is not established and the molten material is initially configured as a quiescent liquid pool.

As high velocity steam/hydrogen mixture impacts on the upper surface of the quiescent pool, the supersonic flow is stagnated and diverted at a right angle. Carrying out the integration shown above for an assumed isothermal process yields

$$\ln\left[\frac{P_o}{P_a}\right] = \frac{U_a^2}{2RT} \tag{3.59}$$

and for an equal volume mixture traveling at 1400 m/sec, the stagnation pressure ratio is almost 0.7 MPa. Thus, for a containment pressure of 0.1 MPa, the isothermal stagnation pressure on the surface of the molten debris pool would be 0.7 MPa. This pressure is imposed on the liquid surface which would deform by moving downward, and the stagnation pressure would represent

the total pressure along a stream line in the moving liquid. Consequently, the downward liquid velocity (U_d) can be estimated by

$$U_d = \left[\frac{2(P_o - P_a)}{\rho_f}\right]^{1/2} \tag{3.60}$$

where ρ_f is the molten core debris density. This would produce a downward velocity of about 14 m/sec.

Given this downward velocity of the pool in immediate contact with the jet, and an assumed initial pool depth of 0.3 m, the material would be driven out of the original impact area in about 0.020 secs. Therefore, the distorted surface at such time would consist of a high amplitude, narrow "ring" as shown as Fig. 3.18. After this interval, the steam/hydrogen gas jet will penetrate to the floor of the reactor cavity where it stagnates and reverses as also shown in this figure. With this highly distorted liquid surface and the high velocity gas flow out of the cavity region, the initial material removed would occur as a result of a breakdown of the distorted ring and entrainment of the resultant debris in the gas stream. The particle size of the debris material can be estimated from the levitation in the high velocity gas flow.

The drag force (F_D) on a spherical particle is given by

$$F_D = C_D \pi r_p^2 \left(\frac{\rho_g U_g^2}{2}\right) \tag{3.61}$$

where C_D is the drag coefficient, r_p is the radius of the particle, ρ_g is the density of the stream, and U_g is the velocity of the gas stream. For a sphere in an infinite flow field, the drag coefficient for high velocity flow is about 0.5 Ref. [3.28], which is the value used in these calculations. However, for a dense array of entrained masses, the drag coefficient could be considerably greater than the above value. This would mean the gas stream would be far more efficient in the entrainment and removal processes than is credited in these calculations. If the drag force is equated to the weight of

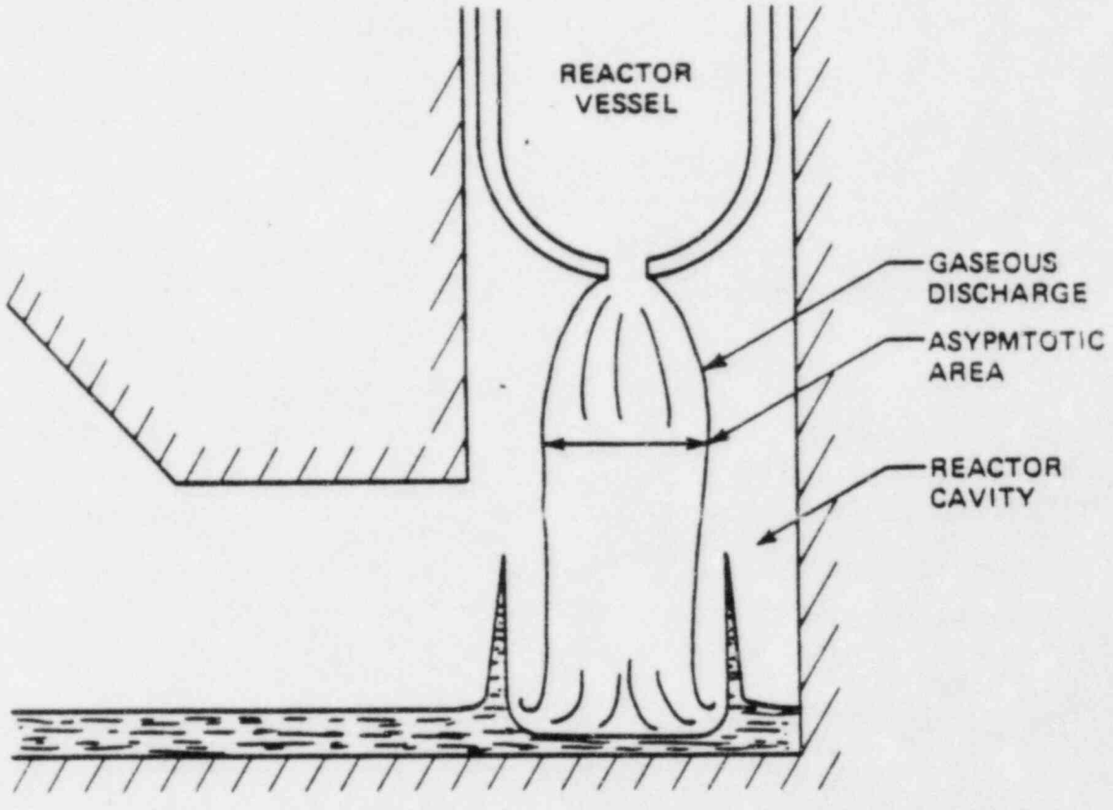

Fig. 3.18 Dynamic pool configuration as a result of initial high pressure gas discharge.

the sphere, the expression for the radius as a function of the gas velocity is given by

$$r_p = \frac{3}{16} \frac{\rho_g U_g^2}{\rho_F g} \tag{3.62}$$

where g is the acceleration of gravity. The velocity of the gas in the instrument tunnel or personnel passageway can be estimated from the blowdown rate through the reactor vessel breach, the density at the containment pressure, and the cross-sectional area of the instrument tunnel or passageway (A_{it}). For a PWR transient sequence, the pressure in the primary system at the time of reactor vessel failure could be about 15 MPa and, with a breach diameter of 0.34 m, the resulting gas discharge rate would be approximately 1160 kg/sec. If the containment pressure at the time of vessel failure is 0.3 MPa, the density for an equal molar mixture of hydrogen and steam at an assumed temperature of 300°C would be 0.6 kg/m^3, and the corresponding velocity in the instrument tunnel ($A_{it} \sim 7$ m^2) about 276 m/sec. Given such conditions, sizable particles could be entrained and levitated. Thus, the breakdown of the material in the distorted ring would be in the form of large particles entrained in the gas stream.

As the gas discharge continues, the impingement and reversal of the steam/hydrogen jet, as illustrated in Fig. 3.19, requires an average pressure on the concrete (P_i) interface which can be expressed as

$$(P_i - P_a)(A_a + A_1) = W_g (U_a + U_1) \tag{3.63}$$

where A_a is the area of the gas jet at the asymptotic diameter, A_1 is the area available for the gas flow after reversal, and U_1 is the average velocity after reversal. This can be rearranged to give

$$P_i - P_a = \frac{W_g^2}{\rho_g A_a A_1} \tag{3.64}$$

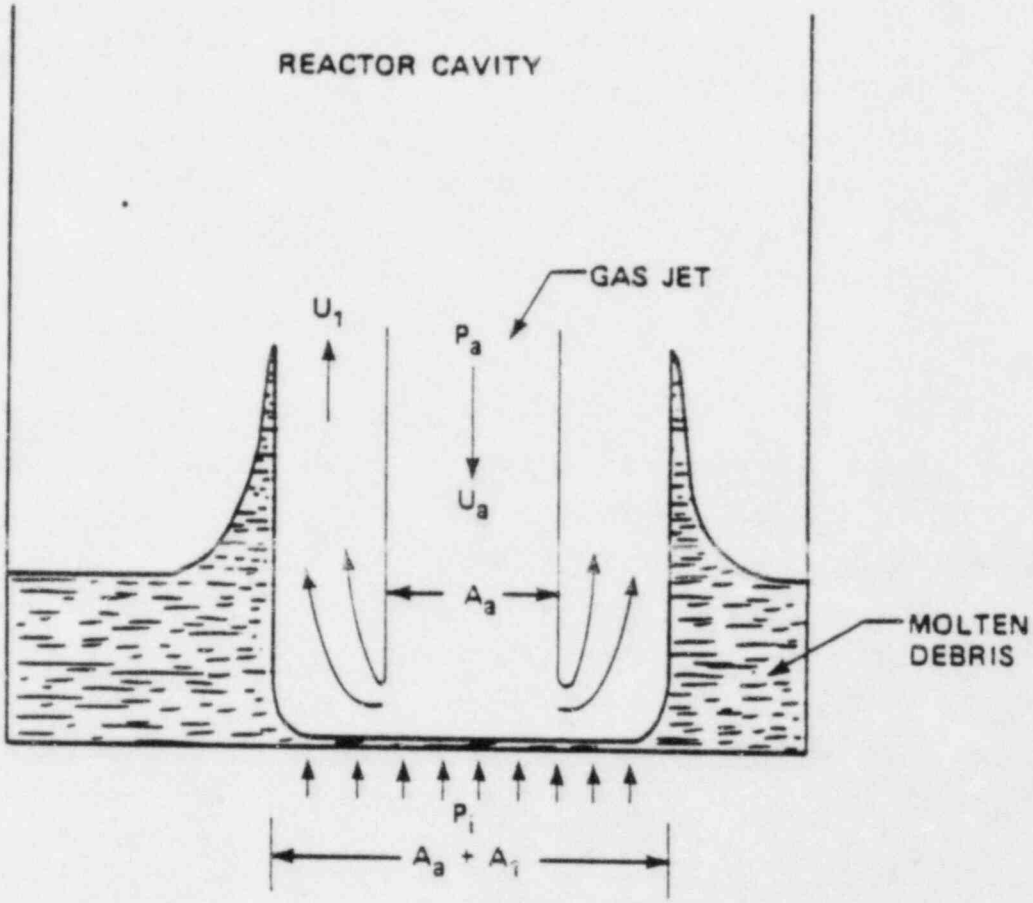

Fig. 3.19 Stagnation and reversal of the high velocity gas jet.

This illustrates that the average pressure decays as the area for reverse flow increases. The reverse flow area can then be equated to the total surface area over which the pool has been removed minus the asymptotic jet area (A_a).

The pressure acting to push back the molten debris pool can be approximated by the addition of the average static pressure required to reverse the jet plus the dynamic head of the gas flow at the base of the molten pool. For an equal volume steam/hydrogen mixture, the stagnation pressures for this flow at the base of the pool are small compared to the static pressure required to reverse the jet; thus only the static pressure due to reversal is considered here.

As a result of the elevated static pressure at the base, a radial movement will be induced into the pool. The rate at which the radial movement would progress can be estimated from the radial acceleration (a):

$$a = \frac{\Delta P}{\rho_F \ell} \tag{3.65}$$

where the driving pressure difference (ΔP) is determined by the gas jet reversal behavior and the half length of the wave (ℓ) resulting from the surface distortion as illustrated in Fig. 3.20. For these approximate calculations, the length (ℓ) is assumed to remain constant, and the sensitivity to the value is determined by assuming a range of characteristic values.

Once the acceleration is determined, the material velocity (v) can be estimated in the finite difference calculations by

$$v = v_o + a\Delta t \tag{3.66}$$

where v_o is the velocity in the previous time step and Δt is the time step interval. Along with the velocity, the change in radius ($r - r_o$) can be obtained from

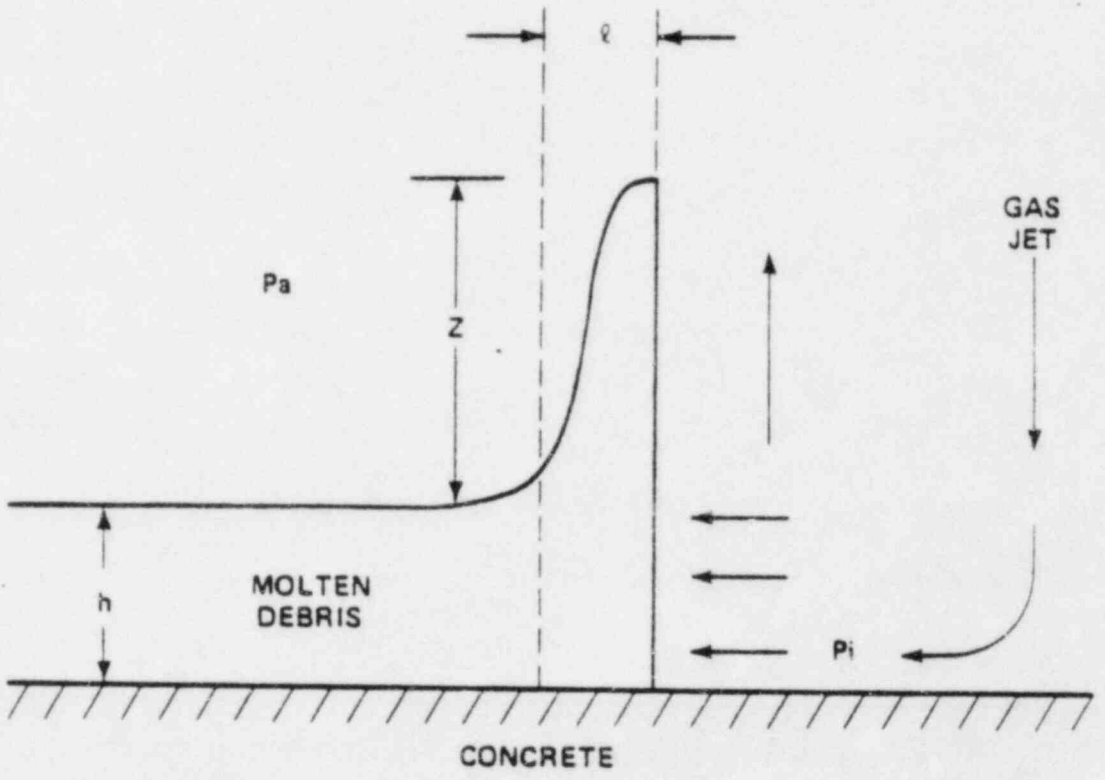

Fig. 3.20 Forces acting on the distorted surface.

$$r - r_o = v_o t + \frac{1}{2} a t^2 \tag{3.67}$$

where r_o is the radius at the beginning of the time step. The volume displaced by the movement (ΔV) is given by

$$\Delta V = \pi(r^2 - r_o^2)h \tag{3.68}$$

where h is the pool height in the undisturbed zone; and for a fixed length (ℓ), this results in an added increment to the wave height (ΔZ) as expressed by

$$\Delta Z = \Delta V/(2\pi r_o \ell) \tag{3.69}$$

As the wave height (Z) grows, the traveling velocity for the wave (U_w) increases as given by

$$U_w = (gZ)^{1/2} \tag{3.70}$$

which for a 1 m high wave would produce a traveling velocity of 3.1 m/sec. This traveling velocity of the wave along the surface can then be compared to the material velocity to determine the basic character of the wave. For instance, if the traveling velocity is large compared to the material velocity, the wave will "stretch out". However, if the material velocity exceeds the traveling velocity, the amplitude of the wave will increase.

In Ref. [3.29], finite difference calculations were carried out for half wave lengths of 0.1 and 0.3 m thickness, with the calculation started from a condition where the area for gas jet reversal was equal to the asymptotic jet area placement previously discussed. The volume displaced by such an initial condition was assumed to be accumulated on the liquid pool with a thickness equal to the half wave length as shown in Fig. 3.20. These calculations, shown in Fig. 3.21, illustrate the basic characteristic of the dynamic process, namely that the amplitude of the wave increases rapidly as does the material velocity. In fact, the material velocity is in excess of the wave velocity characterized by the amplitude. Thus the wave generated by

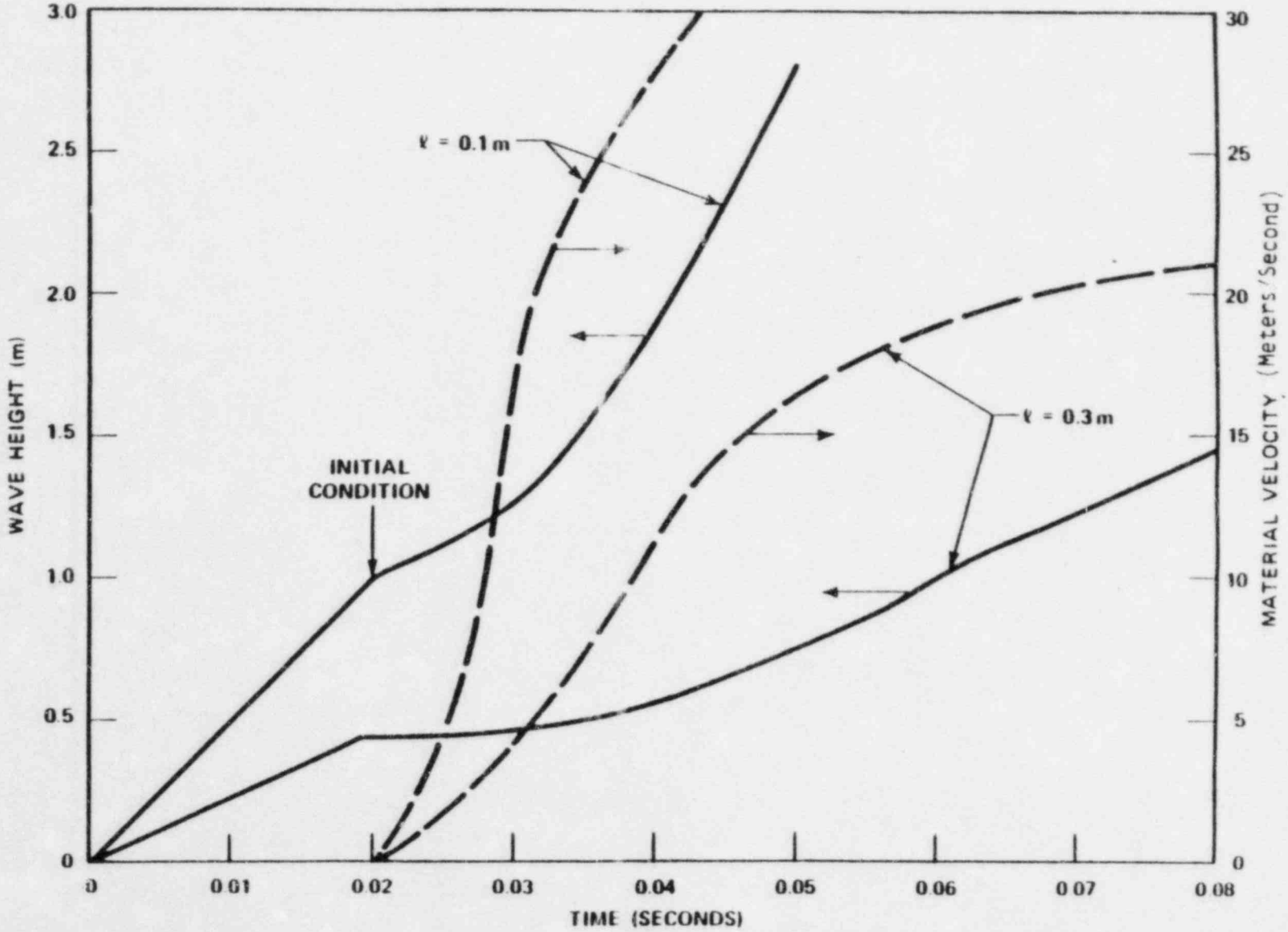

Fig. 3.21 Wave growth and material velocity.

the dynamic response would be a high amplitude, short wave length disturbance, such as shown in Fig. 3.22 for the case where ℓ = 0.3 m, which could travel out to the walls of the reactor cavity and through the instrument tunnel at velocities of tens of meters per second.

Given this dynamic response, the major characteristic produced by the gas jet impingement transient is similar to that generated from the liquid flow alone, i.e. a major fraction of the degraded core material would be transported down the instrument tunnel to the upward sloping section. At this locale, the configuration of the debris would be approximately the same as that developed by the "hydraulic jump" behavior. Since the material velocity could be several tens of meters per second when the wave of molten debris reaches the upward sloping portion of the instrument tunnel, the momentum of the wave itself could play a substantial role in removing the material from the reactor cavity/instrument tunnel region. For the configuration considered in Ref. [3.29], the distance from the floor of the reactor cavity to the floor of the containment is about 8 m. If the sloping configuration of the instrument tunnel diverts the movement from horizontal to essentially vertical, a velocity of slightly over 12 m/sec would be sufficient to enable the material to leave the tunnel region in the presence of gravitational deceleration. This velocity is well below that calculated from the longest wave length.

Another aspect of this dynamic deformation process which should be considered is the influence of water in the reactor cavity/instrument tunnel/pedestal region along with the core debris. For some potential accident scenarios, the degraded core material could be submerged in water and undergoing a vigorous vaporization process. As discussed above, vigorous vaporization would be limited by the liquid (water) flooding limitation applied to the instrument tunnel area or a CHF limitation over the pool surface area. Such a limitation would only apply until the onset of the high velocity gaseous discharge from the reactor pressure vessel. With the dynamic processes induced by this discharge, the heat exchange between the core debris and the water would be augmented substantially, with the principal result of the process being an accelerated quenching of the core debris. This process would occur over a time interval less than one second, and would correspond to

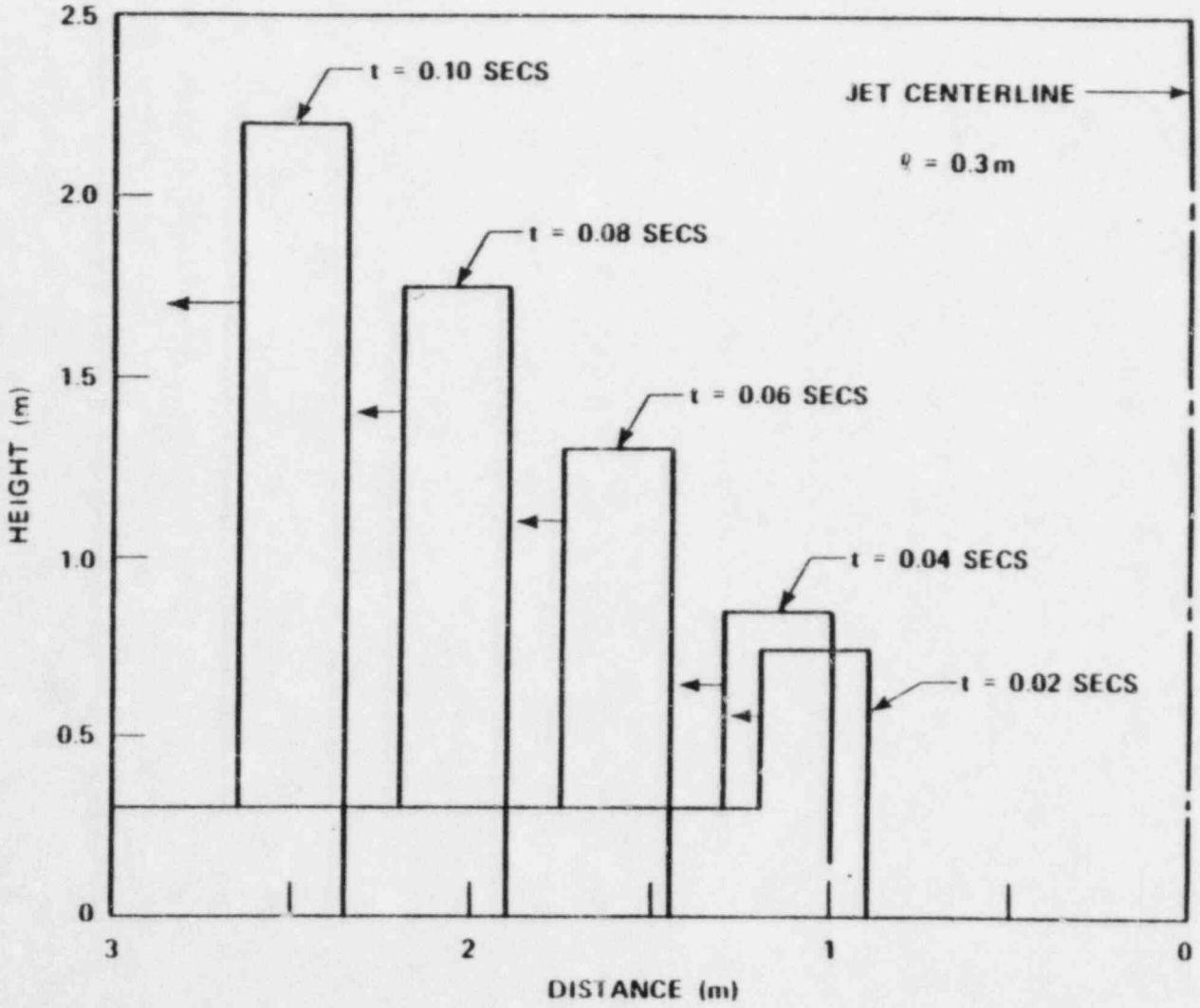

Fig. 3.22 Wave development for a transient sequence with ℓ = 0.3 m.

the time available for removal of the degraded core material from the instrument tunnel region.

The steam produced by the energy transfer process during this period would be added to the containment environment. If the bulk water condition in the reactor cavity/instrument tunnel/pedestal region is one of subcooled liquid, the dynamic process brought on by the high velocity gaseous discharge would be primarily an increase in the sensible heat of this water with little net steam generation.

The geometric configuration of the reactor cavity/instrument tunnel/pedestal regions can substantially influence the overall behavior of the material discharge into the containment for those postulated sequences resulting in a high velocity gaseous discharge. More specifically, while the major motion generated by the combination of high velocity liquid discharge followed by high pressure steam/hydrogen blowdown would produce a combination of a hydraulic jump and wave behavior, breakup and entrainment of the molten material would also occur. In fact, for that fraction of material not removed by the initial dynamic response, entrainment will be the principal removal mechanism from the cavity region. This is demonstrated by comparing the entrainment velocity (U_e) Ref. [3.30] with the average one-dimensional velocity in the instrument tunnel:

$$U_e = \frac{3.7 \left(g\sigma(\rho_F - \rho_g)\right)^{1/4}}{\left(\rho_g\right)^{1/2}} \qquad (3.71)$$

where g is the acceleration of gravity, σ is the surface tension of the core debris mixture, ρ_F is the density of the degraded core material, and ρ_g is the density of the steam/hydrogen mixture at the containment pressure. For example, consider the debris to be 7000 kg/m^3, the surface tension to be 1.0 N/m, and the density of the steam/hydrogen mixture to be 0.6 kg/m^3 corresponding to a containment pressure of 0.3 MPa (the transient sequences). Under these conditions, the resulting entrainment velocity would be 77 m/sec. For the instrument tunnel cross-sectional area of about 8 m^2, the initial gas discharge of approximately 550 kg/sec would result in a velocity of about

115 m/sec, which is greater than the entrainment value. However, the horizontal-to-vertical geometry of the instrument tunnel provides a means whereby the entrained material, particularly the larger sizes, can be separated out of the gas stream and redeposited on the far wall of the instrument tunnel.

This separation process and its relative efficiency can be illustrated by a simple example. Consider the geometry shown in Fig. 3.23 with the characteristic lengths L_1, L_2, and L_3. Assume a spherical particle of radius r_p is accelerated by the horizontal gas flow over the length L_1 with constant acceleration given by

$$a = F/m = \frac{3}{16} \frac{\rho_g U_g^2}{\rho_f r_p} \tag{3.72}$$

where U_g is the gas velocity in the tunnel. The particle velocity at the end of length L_1 would be

$$V_1 = (2aL_1)^{1/2} \tag{3.73}$$

At this position, the particle would have a horizontal velocity but the gas stream would be diverted to an essentially vertical path. If the tunnel cross-sectional area is assumed to remain the same, the vertical acceleration would be equal to that given above. However, for the particle to escape the tunnel intact, it must not impact on the opposite wall where it would be combined with a liquid film of core material, which would occur in a time interval given by

$$t = \frac{L_2}{V_1} \tag{3.74}$$

Consequently, the particle must be accelerated vertically so that it travels the distance L_3 in this time interval:

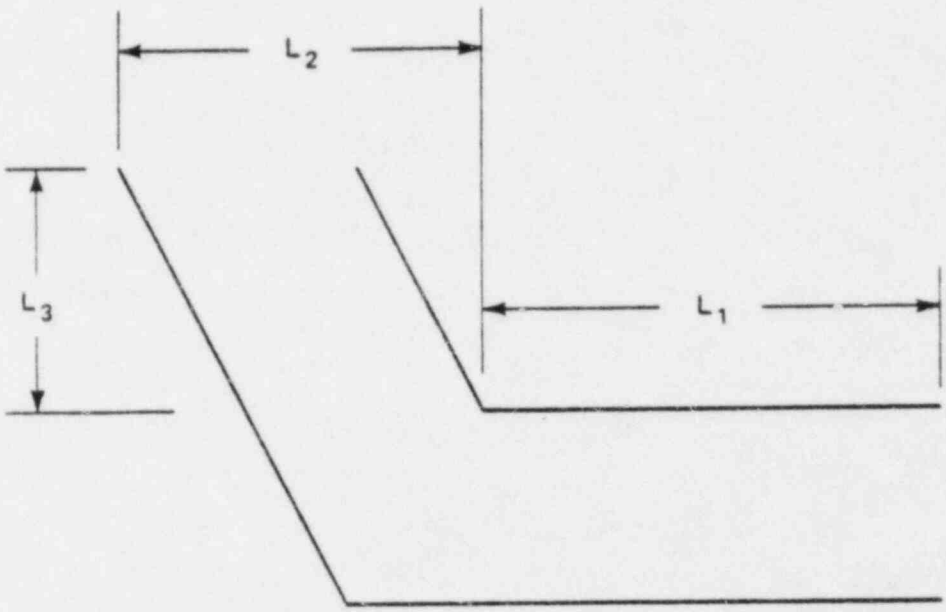

Fig. 3.23 Instrument tunnel configuration for separation calculations.

$$L_3 = \frac{1}{2} at^2 = \frac{1}{2} a \left(\frac{L_2}{V_1} \right)^2 \tag{3.75}$$

Substituting the expression for the velocity V_1 into this relationship yields

$$L_3 = \frac{L_2^2}{4L_1} \tag{3.76}$$

This represents the vertical distance traversed before impact would occur on the opposite wall. Using typical values of 3 m for L_2 and 6 m for L_1 gives a value of 0.38 m for L_3, which is far less than the actual distance. Hence, the separation process generated by the tunnel geometry would be very efficient in recombining discrete liquid globules.

In this state, the material would be transported upward to the containment floor as a recombined liquid stream. The governing expression for vertical transport is the "flooding" velocity for liquid films (U_F) which can be expressed by Ref. [3.30]

$$U_F = \frac{3.0 \left(g\sigma(\rho_f - \rho_g) \right)^{1/4}}{(\rho_g)^{1/2}} \tag{3.77}$$

where the variables in the expression are the same as those defined in (3.71). Since the constant is 3.0 for flooding as opposed to 3.7 for entrainment, a flow rate which satisfied the entrainment criterion will also exceed the flooding limit, i.e. the liquid film would be transported upward.

In summary, three key methods have been identified whereby the molten debris could be removed from the reactor cavity/instrument tunnel/pedestal region principally as a continuous liquid mass:

1. The high velocity liquid discharge directed into the horizontal-to-vertical instrument tunnel configuration thereby producing a hydraulic jump.

2. Large amplitude, short wave length wave formation which could also be directed into the upward sloping tunnel.

3. Entrainment with redeposition on the tunnel walls as a result of the curved flow path.

As a result of these influences, for those postulated accident sequences which result in an elevated primary system pressure at the time of reactor pressure vessel failure, the containment model assumes the material is removed from the cavity region at essentially the initiation of gaseous discharge. Since the major fraction of material is removed as a liquid mass, the containment evaluation model assumes it is distributed on the floor of the adjacent containment volume. Continued quenching could result in this region with the steam being added to the containment atmosphere.

In summary, for those sequences in which the RCS pressure is elevated at the time of vessel failure, the molten core debris accumulation within the reactor cavity/instrument tunnel/pedestal region would be a temporary condition. Because of its own momentum during this high pressure liquid discharge and also the high pressure steam/hydrogen discharge which follows, the core debris would be pushed out of the cavity/pedestal region and onto the containment floor in a time interval in an order of magnitude of one second. This debris removal time is short compared to the gaseous blowdown time of the primary system.

For large break LOCA conditions, the core debris drains from the vessel under its own static head and there is no high velocity gaseous discharge to disperse the material. Consequently, except for that material dispersed by ex-vessel steam explosions, the core debris would accumulate on the floor of the reactor cavity/instrument tunnel/pedestal regions. It should also be noted that BWR systems would also depressurize through the Automatic

Depressurization System (ADS) for most of accident sequences of interest. Hence, the dispersive potential would be negligible for such cases.

3.5 Debris Behavior in BWR Lower Plenums

Molten material moving from the original core boundaries into the lower regions of a BWR would tend to flow preferentially between the control rod drive (CRD) guide tubes. The thermal response of the material as a result of this downward flow of molten debris over the outside of the tubes must consider the thermal time response of the guide tube wall and the vaporization of water contained within the tubes. A model for the thermal response of the corium in the lower plenum has been formulated assuming that the diameter of the tube is sufficiently large that a slab approximation can be made.

During the introduction of molten core debris into the lower plenum the control rod drive tube as shown in Fig. 3.24 will be at least partially filled with water, which by vaporization on the inner surface will maintain the steel tube near the saturation temperature of the water, T_{sat}. Assuming that T_{sat} is constant, the thickness of the solidified corium layer is small compared to the radius of curvature of the tube, the molten core material is quiescent, material properties are constant, and the temperature difference across the upper CRD tube is small, the transient temperature solutions in the solidified and molten core material can be determined, respectively, from the relations given in Ref. [3.24],

$$T_s(x,t) = \frac{T_{mp}}{\text{erf}\lambda}\,\text{erf}\,\frac{x}{2(\alpha_s t)^{1/2}} \tag{3.78}$$

where $T_s(x,t)$ is the time dependent temperature profile of solid layer, and

$$T_L(x,t) = T_o - \frac{T_o - T_{mp}}{\text{erfc}\lambda\left(\frac{\alpha_s}{\alpha_L}\right)^{1/2}}\,\text{erfc}\,\frac{x}{2(\alpha_L t)^{1/2}} \tag{3.79}$$

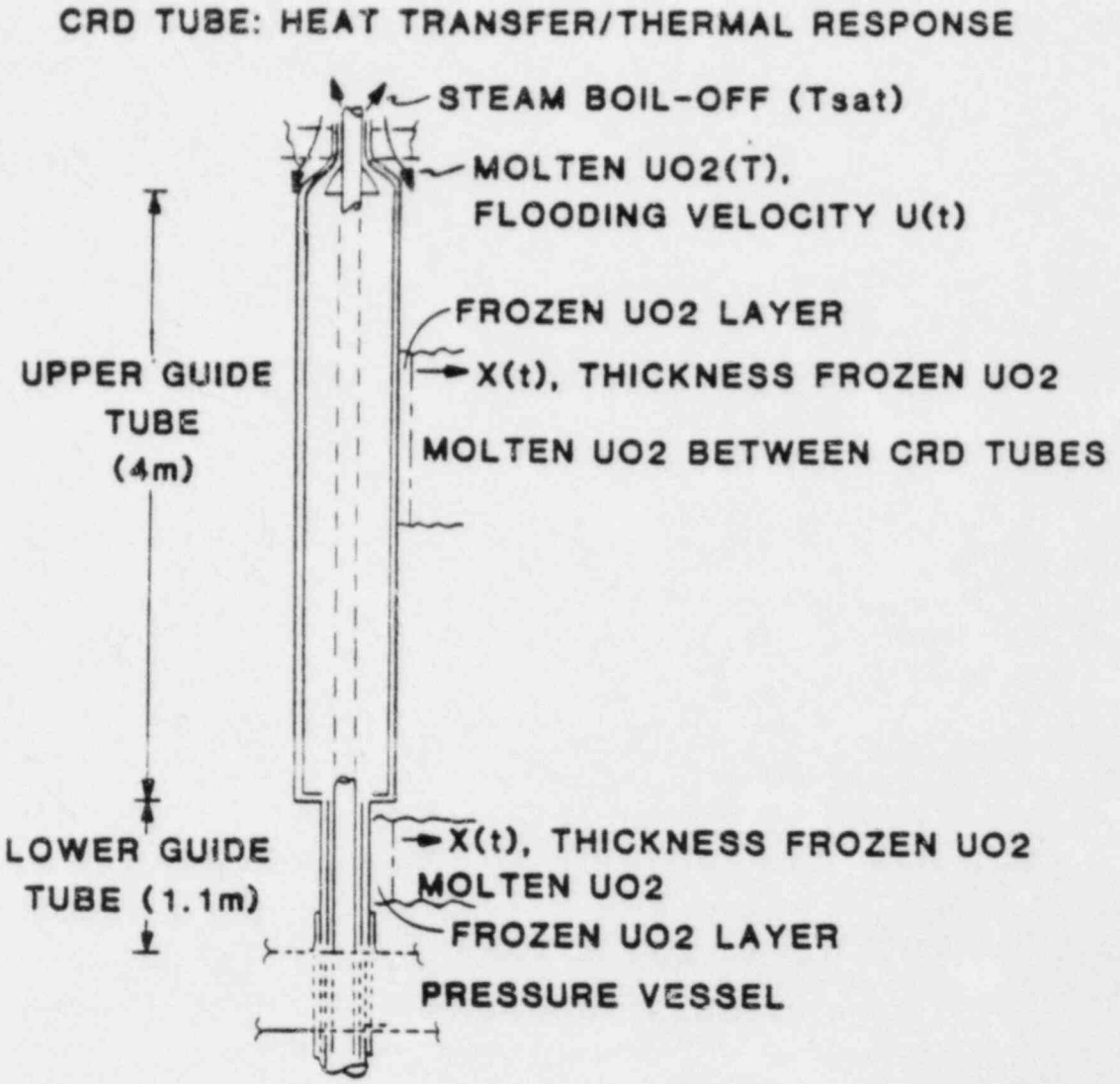

Fig. 3.24 Control rod drive guide tube configuration.

where $T_L(x,t)$ = time dependent temperature profile of liquid layer

α = thermal diffusivity (s = solid layer, L - liquid layer) in which the surface temperature at x = 0 is zero and the initial liquid and melting point temperature are T_o and T_{mp}, respectively.

The location of the freeze front is given by:

$$X(t) = 2\lambda(\alpha_s t)^{1/2} \tag{3.80}$$

The value of λ is determined from the transcendental relation:

$$\frac{e^{-\lambda^2}}{erf\lambda} - \frac{k_L}{k}\sqrt{\frac{\alpha_s}{\alpha}}\frac{(T_o - T_{mp})\exp\left(-\frac{\alpha_s}{\alpha_L}\lambda^2\right)}{T_{mp}\,erfc\lambda\left(\frac{a_s}{\alpha_L}\right)^{1/2}} = \frac{\lambda L \pi^{1/2}}{c_s T_{mp}} \tag{3.81}$$

where: L = latent heat of fusion and c = specific heat. Fig. 3.25 provides a sketch of the thermal transport.

For the case in which the coolant temperature is non-zero, but finite at T_c, a shift in the temperature scale is required. Redefining $T^* = T - T_c$ the relations are simply modified to replace T by T* in Eqs. (3.78), (3.79), and (3.81). Further, the liquid and solid properties of the fuel are taken as equal so that these relations reduce to:

$$T_s^*(x,t) = \frac{T_{mp}^*}{erf\lambda}\,erf\frac{x}{2(\alpha_s t)^{1/2}} \tag{3.82}$$

$$T_L^*(x,t) = T_o^* - \frac{T_o^* - T_{mp}^*}{erfc\lambda}\,erfc\frac{x}{2(\alpha_s t)^{1/2}} \tag{3.83}$$

and

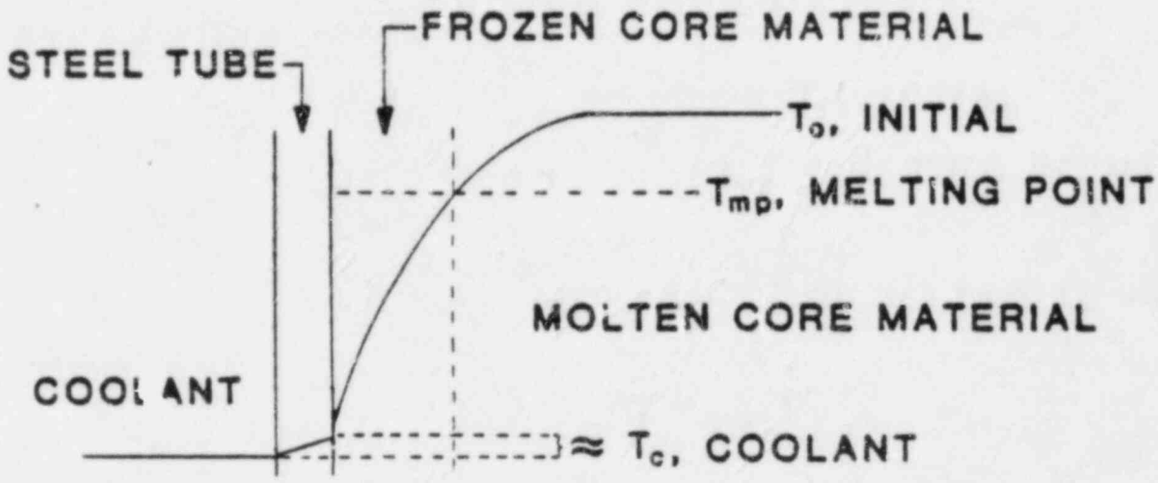

Fig. 3.25 Thermal transport processes for CRD guide tube .

$$\frac{e^{-\lambda^2}}{erf\lambda} - \frac{T_o^* - T_{mp}^*}{T_{mp}^*} \frac{e^{-\lambda^2}}{erfc\lambda} = \frac{\lambda L\pi^{1/2}}{cT_{mp}^*} \tag{3.84}$$

For the simplified case in which $T_o = T_{mp}$, Eqs. (3.79) and (3.81) reduce to:

$$T_L^*(x,t) = T_{mp}^* \tag{3.85}$$

and

$$\frac{e^{-\lambda^2}}{\lambda erf\lambda} = \frac{L\pi^{1/2}}{cT_{mp}^*} \tag{3.86}$$

Typical conditions for molten core material T_{mp} with 500°K cooling water would be:

$T_{mp} = 2673°K$, $T_o = 500°K$ and $T_{mp}^* = 2173°K$

$L = 3 \times 10^2$ kJ/kg

$c = 0.6$ kJ/kg - °K

$\alpha = 7.9 \times 10^{-7}$ m^2/sec

The value $cT_{mp}^*/L\pi^{1/2} = \lambda e^{\lambda^2} erf\ \lambda = 2.45$ from which $\lambda = 1.0$, the asymptotic value.

For the case of superheated molten core material of $T_o = 3000°K$ and the same base conditions as above, $\lambda = 0.9$. In the numerical algorithm this value is used for cases in which superheat is considered. It has only a minor influence on the thickness of the frozen layer.

The energy transfer rate to the water can be determined from the wall heat flux:

$$k \frac{\partial T_s^*}{\partial x}\bigg|_{x=0} = \frac{T_{mp}^* k}{erf\lambda(\pi\alpha)^{1/2} t^{1/2}} \quad (kJ/s\text{-}m^2) \tag{3.87}$$

and the accumulated wall energy transfer flux is:

$$Q(t) = \frac{2(T^*_{mp})k}{(\pi\alpha)^{1/2}\,\mathrm{erf}\lambda}\, t^{1/2} \qquad (kJ/m^2)$$

It should be noted that although the presence of the steel tube will absorb the very high initial wall heat flux, as this initial transient proceeds its temperature will quickly decrease so as not to seriously perturb the original assumption of no tube influence. This initial surge will also tend to prevent film boiling from occurring inside the tube.

Utilization of this energy transfer to the CRD tube water and that transfer during the filling period allows one to estimate the time intervals required for tube dryout, heat up and failure. For the $T_o = T_{mp}$ case considered, this time is ≈ 140 seconds. Since the heat sink is lost at this time, no further freezing on the upper CRD tube will occur and the thickness of the frozen layer can be determined from Eq. (3.80) with a correction to account for any core material frozen during filling. For this case X(140) ≈ 0.02 m.

The average temperature of the frozen layer, if at boil-off the molten corium is removed from the lower plenum, is obtained simply by integrating the solid temperature profile and spatially averaging since a uniform temperature profile will establish much more rapidly than the material will remelt by decay heat. The adiabatic temperature rise rate is about 0.2°K/sec. For the simplest case:

$$T^*(t_f) = \frac{T^*_{mp}}{\mathrm{erf}\lambda}\,\frac{1}{X}\int_0^X \mathrm{erf}\,\frac{x}{2\sqrt{\alpha t}}\,dx \qquad (3.89)$$

or

$$\bar{T}^*(t_f) = \frac{T^*_{mp}}{\mathrm{erf}\lambda}\left[\mathrm{erf}\lambda - \left(\frac{1 - e^{-\lambda^2}}{\lambda\sqrt{\pi}}\right)\right] \tag{3.90}$$

We note that the initially frozen material will have relaxed thermally so that the freeze front progresses according to Eq. (3.80). Therefore, with the CRD guide tube configuration in BWR systems, a considerable amount of debris can be held-up as frozen crust on the surface of the tubes and steam can be produced by vaporizing the CRD water on the inside of the tubes. This is modeled in the MAAP code.

3.6 Summary

The major issues of in-vessel and ex-vessel coolability can be addressed through a variety of models for particulated debris, all of which demonstrate reasonable agreement for particle sizes of about 1 mm. If the debris could be fragmented to sizes much smaller than this, the limitation to the removal would lie within the bed configuration itself. For much larger sizes, the limitation to bed heat removal appears to be hydrodynamic conditions at the top of the bed.

With the failure of a lower head penetration, the ablation of the reactor vessel wall by the high temperature debris is considerable and would be influential in determining subsequent events such as debris dispersal. Similar considerations must also be given to the material discharge following the overheated vessel failure for those configurations without bottom head penetrations.

Debris distribution within the reactor containment building following reactor vessel failure could be substantially influenced by the gaseous blowdown for those accident scenarios where the primary system contains a considerable pressure until vessel failure. These considerations are greatly dependent upon the specific geometry of the containment building and must be evaluated for each individual design. Hence, influence of these forces is a function of the accident sequence and specific geometrical characteristics.

3.7 References

3.1 L. Barleon and H. Werle, "Dependence of Debris Bed Dryout Heat Flux on Particle Diameter," Trans. of ANS, 38, June 1981, pp. 382-392.

3.2 D. Squarer, A. T. Pieczynski and L. E. Hochreiter, "Dryout in Large Particle, Deep Beds," Trans. of ANS, 38, June 1981, pp. 444-445.

3.3 R. Trenberth and G. F. Stevens, "Experimental Study of Boiling Heat Transfer and Dryout in Heated Particulate Beds," AEEW-R1342, July 1980.

3.4 P. N. Rowe, "Drag Forces in a Hydraulic Model of a Fluidized Bed - Part II," Trans. of Institute of Chemical Engineers, Vol. 39, 1961, pp. 175-180.

3.5 P. N. Rowe and G. A. Henwood, "Drag Forces in a Hydraulic Model of a Fluidized Bed - Part I," Trans. of Institute of Chemical Engineers, Vol. 39, 1961, pp. 43-54.

3.6 G. B. Wallis, One-Dimensional Two-Phase Flow, McGraw-Hill Book Co., 1969.

3.7 S. Ergun, Chemical Engineering Progress, 48, 1952, p. 93.

3.8 R. L. Lipinski, "Particle Bed Dryout Model with Upward and Downward Boiling," Trans. of ANS, 35, 1980, pp. 358-360.

3.9 R. W. Ostensen, "Advanced Reactor Safety Research Program Quarterly Report: October-December 1979," Sandia National Laboratories, 1980.

3.10 H. C. Hardee and R. H. Nilson, "Natural Convection in Porous Media with Heat Generation," Nucl. Sci. Eng., 63, 1977, pp. 119-132.

3.11 V. K. Dhir and I. Catton, "Prediction of Dryout Heat Fluxes in Beds of Volumetrically Heated Particles," Proc. Intl. Mtg. on Fast Reactor Safety and Related Physics, Chicago, Illinois, Vol. IV, October 1976, pp. 2026-2035.

3.12 "Final Report of Key Plenomerological Models for Assessing Non-Explosive Steam Generation Rates," Fauske AND Associates Report, FAI/82-30, December 1982.

3.13 "Hydrogen Generation During Severe Core Damage Sequences," Fauske and Associates Report, FAI/82-33, December 1982.

3.14 M. Epstein, J. Heat Transfer, Vol 99, p. 527, 1977.

3.15 A. Yim, M. Epstein, S. G. Bankoff, G. A. Lambert and G. M. Hauser, Int. J. Heat Mass Transfer, Vol. 21, p. 1185, 1978.

3.16 M. Epstein, M. J. Swedish, J. H. Linehan, G. A. Lambert, G. M. Hauser and L. T. Stachyra, AIChE Journal, Vol. 26, p. 743, 1980.

3.17 H. Martin, Advances in Heat Transfer, 3, Academic Press, New York, 1, 1977.

3.18 W. E. Stewart and R. Prober, Int. J. Heat Mass Transfer, Vol. 5, p. 1149, 1962.

3.19 C. D. Donaldson, R. S. Snedeker and D. P. Margolis, J. Fluid Mech. Vol. 45, p. 477, 1971.

3.20 F. Giralt, C. J. Chia and D. Trauss, Ind. Eng. Chem. Fundamentals, Vol. 16, p. 21, 1977.

3.21 S. Sitharamayya and K. Subba Raju, Can . J. Chem. Eng., Vol. 47, p. 365, 1969.

3.22 M. J. Swedish, M. Epstein, J. H. Linehan, G. A. Lambert, G. M. Hauser and L. J. Stachyra, AIChE Journal, Vol. 25, p. 630, 1979.

3.23 M. Epstein, Int. J. Heat Mass Transfer, Vol. 19, p. 1281, 1976.

3.24 H. S. Carslaw and J. C. Jaeger, Conduction of Heat in Solids, 2nd Ed. Oxford University Press, Oxford, 1959.

3.25 M. Epstein, M. G. Grolmes, R. E. Henry and H. K. Fauske, "Transient Freezing of a Flowing Ceramic Fuel in a Steel Channel," Nuc. Sci. Eng., Vol. 61, pp. 310-323, 1976.

3.26 F. G. Blottner, "Hydrodynamics and Heat Transfer Characteristics of Liquid Pools with Bubble Agitation," NUREG/CR-0944, SAND 79 1132, 1979.

3.27 H. L. Dryden, F. D. Murnaghan and H. Bateman, Hydrodynamics, Dover Publications, 1956, p. 540.

3.28 J. K. Vennard, Elementary Fluid Mechanics, 3rd Edition, John Wiley & Sons, Inc., New York, 1959.

3.29 Zion Probabilistic Safety Study, Commonwealth Edison Company, September, 1981.

3.30 H. K. Fauske, "Boiling Flow Regime Maps in LMFBR HCDA Analysis," Trans. ANS, Vol. 22, 1975, pp. 385-386.

4.0 RELEVANT EXPERIMENTAL INFORMATION

4.1 Introduction

Of the major issues, (1) in-vessel and ex-vessel debris coolability, (2) vessel failure and (3) debris dispersion, experimental information has been reported for debris coolability and dispersion. The debris bed experiments have been principally oriented toward measurements of the maximum heat removal capacity (dryout heat flux) for particulated beds with uniform spherical particles. The three major studies, Refs. [4.1, 4.2, and 4.3] relevant to LWR accident evaluations will be discussed in this section.

Experiments Ref. [4.4] demonstrating the potential for debris dispersal have been carried out in benchtop scaled configurations of the Zion reactor cavity/instrument tunnel configuration and also with a simulation of BWR Mark III pedestal region, Ref. [4.5]. These experiments were performed with both water and cerrulo (a high density metal alloy with a low melting temperature) to determine the gaseous velocity required to effect debris dispersal. These will be summarized in this section.

4.2 Debris Bed Dryout Experiments

Debris bed experiments have generally been performed with uniform spherical particles in various depths. While extensive numbers of experiments have been performed over a wide range of particle sizes (100 microns to 1.5 cm in diameter) only three experiments have been performed in the range of interest for LWR accident scenarios. These are the experiments reported by Trenberth and Stevens [4.1], Squarer, et al [4.2] and Barleon and Werle [4.3]. These tests cover a range of particle sizes from about 500 μm to 1.5 cm in diameter and were conducted with either induction heating or direct electrical heating of the particles.

Trenberth and Stevens varied both the particle size and the bed depth in their experiments. These tests demonstrated the strong influence of the bed depth for rather shallow beds with a marked transition to a constant dryout heat flux at a depth of a few centimeters. The bed height at which

this transition to a constant heat flux occurred was observed to be dependent upon the particle size and was interpreted as the onset of the deep bed limit. As will be discussed, another important parameter which was automatically varied as the bed depth changed was the surface heat flux of the individual particles. This can have a substantial influence on the flow patterns developed within these densely packed particulate beds.

Squarer et al. investigated particle sizes of 0.6, 1.2, and 6 mm in diameter with the particles being heated by an induction coil. As with previous investigations, the dryout heat flux was found to be a function of the particle size with all the experiments in this study being performed as "deep beds". Results from these various particle sizes show that dryout heat fluxes below the critical heat flux limit for the smaller particle sizes and somewhat above for those tests carried out with 6 mm particles. Here again, the surface heat flux for the individual particles could have a significant influence on the flow regimes developed inside of the particle beds. As was discussed in Section 3, these considerations can determine whether continuous liquid films can cover the surface of the particles as is assumed by most of the debris bed formulations.

Large particle (2 mm to 1.5 cm in diameter) debris bed dryout experiments were performed by Barleon and Wehre with induction heated beds of steel walls. These beds were typically 10 cm deep and measured dryout heat fluxes as high as 5000 kw/m^2. The dryout measurements for these experiments were generally greater than those reported by both Threnberth and Stevens and Squarer et al., with the data typically being several times that representative of the pool boiling critical heat flux on a horizontal flat plate. In fact, for the largest particle sizes, the surface heat flux of the individual particles is a substantial fraction (0.25 to 0.5) of the pool boiling critical heat flux. As a result, these experiments would not develop a continuous liquid film over the surface of the particles and the only stable flow regime which could develop within the bed would be dispersed flow, i.e. individual droplets falling through the bed and temporarily wetting the particle surface. It should also be noted that these extremely high heat fluxes at the particle surface are not typical of the conditions of interest in LWR accident evaluations. As a result, the differences described by these

tests must be incorporated when assessing the potential for achieving a permanently coolable state within a reactor system. The only time such large surface heat fluxes could potentially be achieved would be during the quenching of overheated but solidified core debris, i.e. removal of stored heat as opposed to removal of decay power.

In a follow-on study, Squarer, et al., Ref. [4.6] carried out experiments with various particle size mixtures to investigate the effect upon dryout heat flux. Mixtures with particle sizes varying over an order of magnitude were employed and the results indicate the combination of particle size and porosity determine the coolability limit. For the reactor system, fine scale fragmentation of the melt would require either large forces or a much larger reactor vessel. Neither of these is typical of behavior within the primary system and should small particles be developed after the material has left the reactor vessel, large areas are generally available for cooling. This will be discussed further in Section 6.

4.3 Debris Dispersal Experiments

To demonstrate the effect of gaseous blowdown forces on the accumulation of molten debris within a reactor cavity, Spencer et al. [4.4] conducted a bench scale experiments using a simulation of the Zion reactor cavity and instrument tunnel configuration. Figure 4.1 illustrates the pertinent dimensions of the experimental apparatus and the materials investigated for this dispersion potential were water and Cerrelow-136, the latter being a metallic alloy with a melting point of 58°C. In addition, this alloy has a density of about 8600 kg/m^3 which allows a simulation of the dispersive capabilities for high density materials within this simulated reactor cavity. These experiments were carried out in both a quasi-steady and a transient manner to determine the velocities required to entrain and remove the debris from this configuration. These experiments demonstrated that a velocity of 10 m/sec was sufficient to disperse the water while a velocity of about 30 m/sec was required to disperse the Cerrelow out of the instrument tunnel. The transient runs demonstrated both the wave formation and the entrainment phenomena with the net result of each of these being an

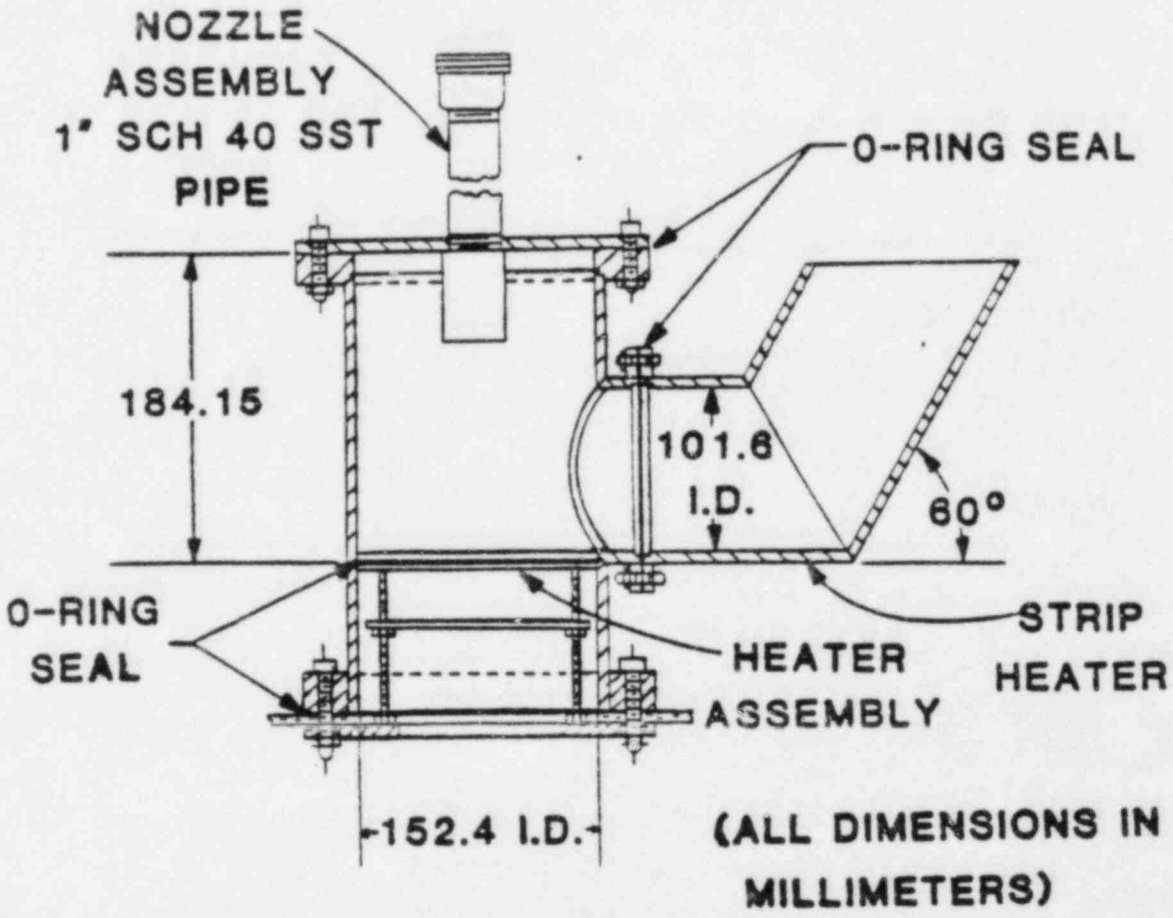

Fig. 4.1 Reactor cavity simulation apparatus.

accumulation of debris along the upward sloping wall of the instrument tunnel, i.e. the major fraction of material is released from the reactor cavity region as a continuous liquid wave. It should be noted that these velocities are below those generally subscribed to entrainment levels for horizontal gas flow over a liquid interface. Hence, the cavity configuration and perhaps the dynamic processes associated with the transient behavior result in a more efficient material removal and dispersal than would be normally attributed to an entrainment process.

In addition, Spencer Ref. [4.5] performed benchtop scale, simulant fluid dispersal tests for a BWR Mark III configuration. These tests illustrated that a BWR Mark III geometry could experience significant dispersal should the reactor vessel blowdown from an elevated pressure after discharge of the molten core debris. This will be discussed in detail in Section 6.

4.4 Summary

Debris bed experiments have demonstrated that the heat removal capabilities for debris beds with particle sizes of several millimeters are approximately equal to or greater than the pool boiling critical heat flux for a horizontal flat plate. While this can be directly attributed to the dependence upon particle size, the experiments which have been conducted have resulted in employed surface heat fluxes off the individual particles which have been substantially greater than those which would be anticipated in reactor accident conditions. As a result, these must be accounted for in the interpretation and extrapolation to the reactor system.

Small scale experiments have demonstrated the potential for debris removal from reactor cavity/instrument tunnel/pedestal configurations should these provide for a smooth continuous path for the debris. These experiments have demonstrated that the velocities required for dispersal are considerably less (about a factor of 3) than those which would be required for direct entrainment off of a horizontal liquid interface.

4.5 References

4.1 R. Trenberth and G. F. Stevens, "Experimental Study of Boiling Heat Transfer and Dryout in Heated Particulate Beds," AEEW-R1342, July 1980.

4.2 D. Squarer and J. A. Peoples, "Dryout and Inductively Heated Beds With and Without Forced Flow," Transactions ANS, Vol. 34, p. 535, 1980.

4.3 L. Barleon and H. Werle, "Dependence of Debris Bed Dryout Heat Flux on Particle Diameter," Transactions of the ANS, Vol. 38, p. 382, 1981.

4.4 B. W. Spencer, D. Kilsdonk, J. J. Sienicki, and G. R. Thomas, "Phenomenological Investigations of Cavity Interactions Following Postulated Vessel Melt-Through," paper presented at the ANS/ENS International Meeting on Thermal Reactor Safety, Chicago, Illinois, August 1982.

4.5 B. W. Spencer, personal communication, 1982.

4.6 D. Squarer, A. T. Pieczynski, and L. E. Hochreiter, "Affect of Debris Bed Pressure, Paritcle Size and Distribution on Degraded Nuclear Reactor Core Coolability," Nuclear Science and Engineering, 80, p. 2, 1982.

5.0 COMPARISONS WITH EXPERIMENTS

5.1 Introduction

To provide the necessary background for extrapolating the basic considerations presented in Section 3 to the postulated reactor accident case, these physical models must be compared to the range of experimental information available. As discussed in Section 4.0, pertinent experimental information is only available for debris bed coolability and for the potential for debris dispersion in those accident scenarios with an elevated primary system pressure.

5.2 Debris Bed Coolability

The data of particular interest for application to LWR systems are the large particle data reported in Refs. [5.1-5.3] where uniform particle sizes were used, the sizes varying from sub-millimeter diameters to 1.6 cm in diameter. For the very large particle sizes used by Barleon and Werle, the porosity increased substantially with the particle size. As a result, the data is compared in Table 5.1 for the specific experimental conditions. As shown in the table, the hydrodynamic stability limit is in agreement with the measured dryout heat fluxes.

The combined results of Refs. [5.1,5.2,5.3,5.4] for water are compared to the proposed models in Fig. 5.1. These data are for a porosity of ~ 0.4 and the two largest particle sizes of Ref. [5.1] are omitted since the measured porosity is significantly greater than 0.4. As shown, the shallow bed data (~ 8 cm) of Ref. [5.1] is in good agreement with the hydrodynamic stability limit, whereas the deep bed results of Ref. [5.2] (up to 30 cm) and Ref. [5.3] (up to 20 cm) have lower dryout heat fluxes and are in closer agreement with the internal bed limitation. The small particle, deep bed data reported in Ref. [5.4] have heat fluxes comparable to or less than those of Refs. [5.2] and [5.3] and begin to approach the values typical of bottom heating [5.5]. The CHF for a horizontal flat plate is about 1200 kw/m^2 at a pressure of 0.1 MPa and represents an average value for the dryout heat flux

Table 5.1

Hydrodynamic Stability at the Top of the Bed
Comparison with the Water Data of Barleon and Werle

Particle Size mm	Bed Porosity	Dryout Heat Flux	
		Predicted kw/m^2	Experimental Range kw/m^2
2	0.386	1077	1050-1150
3	0.392	1504	1100-1400
4.76	0.403	2037	2000
7.94	0.422	2946	2200-2700
10.00	0.436	3655	3600-4300
15.88	0.473	5250	5600-4800

in the range of several millimeter diameter particles. This greatly simplifies the calculation for both coolability and quenching and as a result is the manner in which such behaviors are represented in the MAAP code.

Similar comparisons are shown in Fig. 5.2 for Freon-113 data for a bed porosity of 0.4. As with the water data, the very large particle, shallow bed measurements of Ref. [5.1] are in better agreement with the hydrodynamic stability model and the small particle, deep bed data of Ref. [5.4] is in general agreement with the internal limitation approach. Also, the deep bed dryout heat fluxes approach those typical of bottom heating.

5.3 Debris Dispersal

The experiments carried our by Spencer et al. [5.6] demonstrated that the phenomena of wave formation and entrainment are indeed experienced in the bench scale simulation of the Zion reactor cavity and instrument tunnel configuration. In these experiments, the velocity required for removal of water from this configuration were approximately 10 m/sec and that required for removal of the much heavier Cerrelow alloy was about 30 m/sec. As discussed in the Zion Probabilistic Safety Study [5.7], only gaseous velocities of 100 m/sec and above through the instrument tunnel were credited for the removal of the debris. As demonstrated by the experiments of Ref. [5.6] these values were conservative and debris dispersal would be anticipated for velocities considerably less than those credited in Ref. [5.7].

In other similar experiments [5.8] with a BWR Mark III simulation, Spencer demonstrated that dispersal could be achieved in such geometries. As a result of the "sunken" pedestal arrangement, the velocities causing entrainment are more difficult to quantify. This will be considered in Section 6.

As discussed in Section 2.0, these dispersal mechanisms are greatly influenced by the specific geometry of the reactor cavity and instrument tunnel for the pressurized water reactor systems and for the pedestal and drywell regions for the BWR systems. Therefore, while the potential for

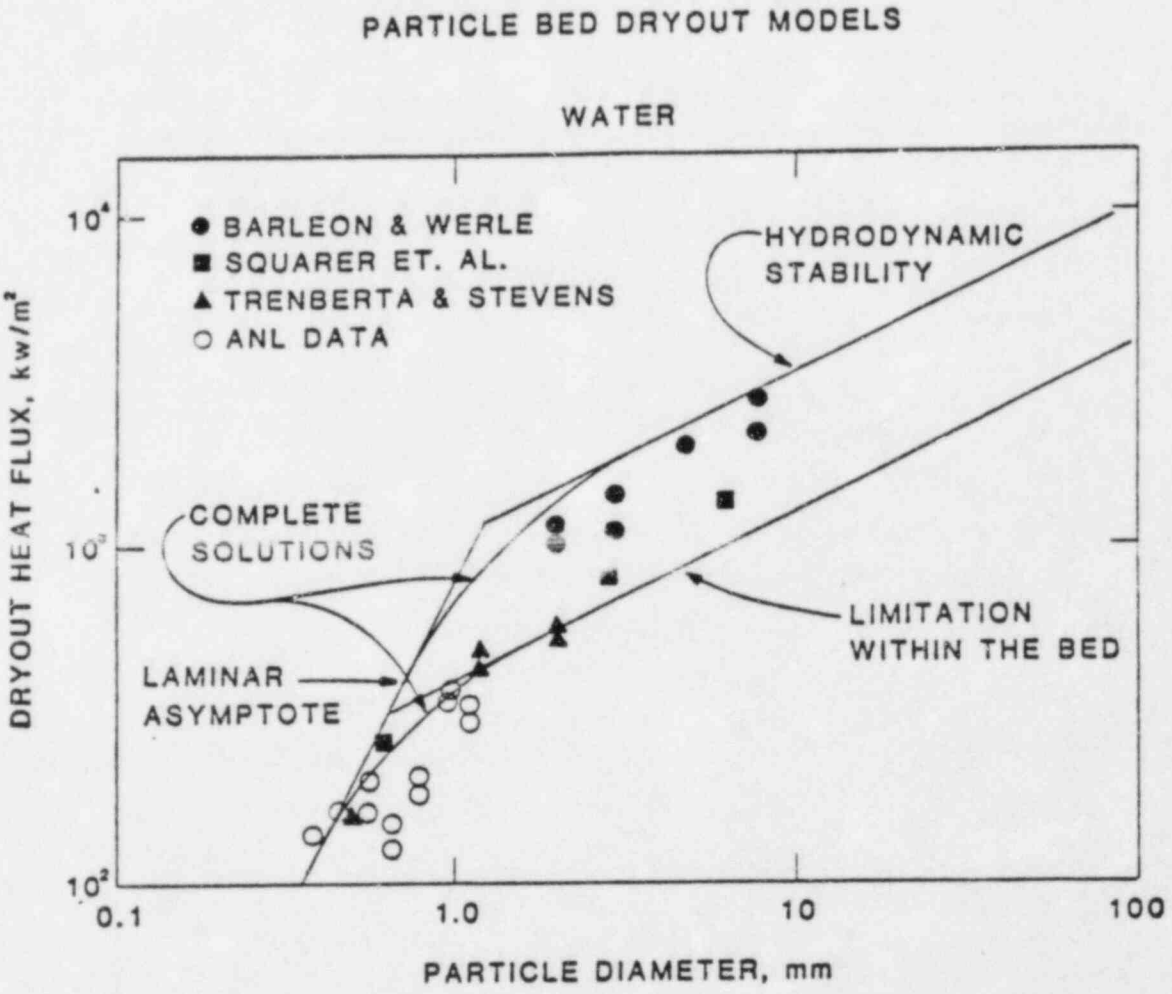

Fig. 5.1 Comparison of the two limitations and experimental data. Bed porosity ∿ 0.4.

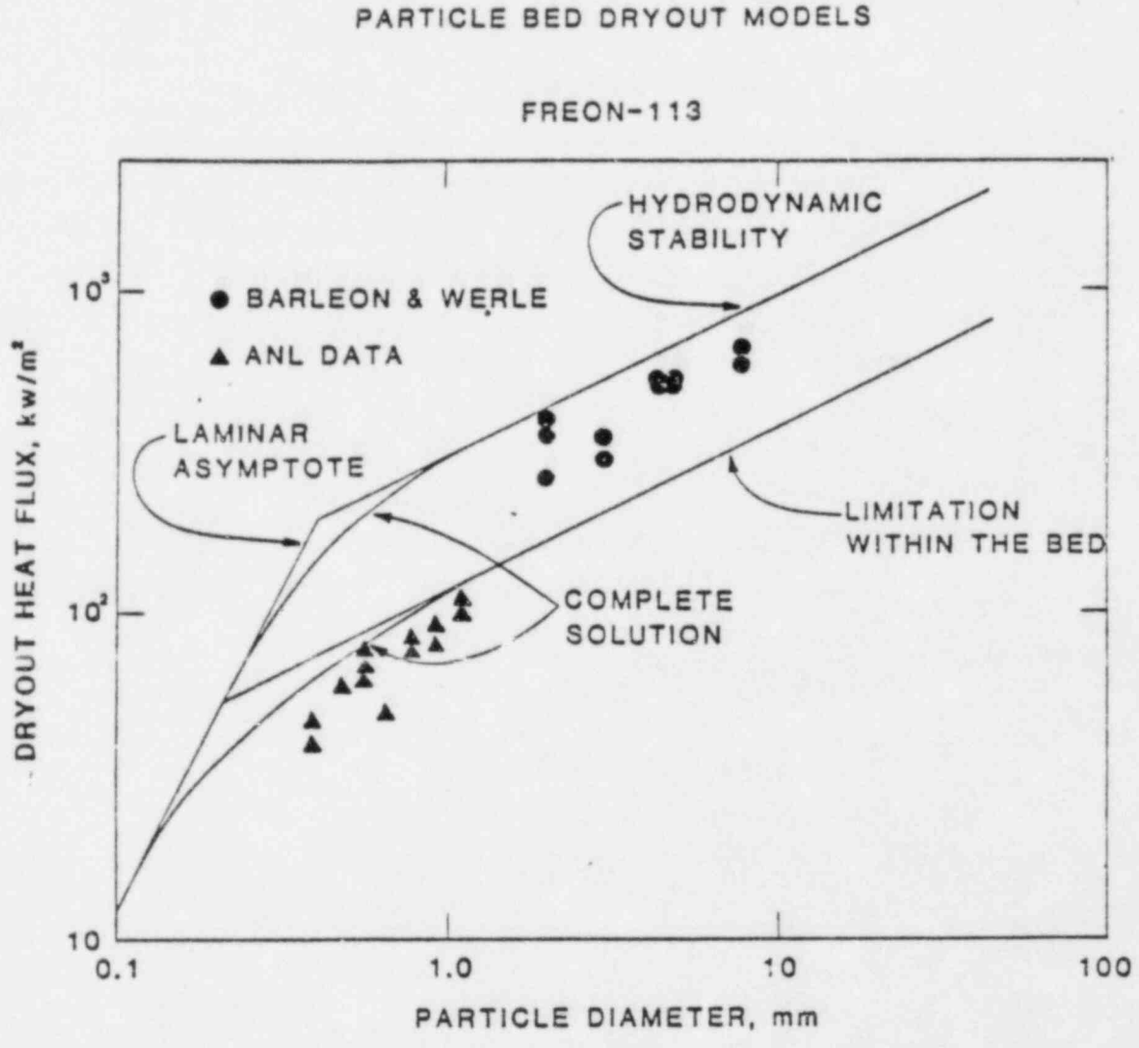

Fig. 5.2 Comparison of the two limitations with experimental data. Bed porosity = 0.4.

debris dispersal is conservatively represented by the entrainment criteria, the individual geometric configurations must be considered in the reactor system evaluations.

5.4 Summary

Comparisons of the experimental information for debris bed coolability with the simplified models used in the MAAP code show an excellent agreement for the range of data considered. For the reactor systems, the internal bed limitation is the most appropriate modeling considering the surface heat fluxes off of the debris particles is far less than those representative of the experimental information acquired in the tests of Squarer et al. and Barleon and Werle. Therefore, since the actual particle size would not be known for specific reactor conditions, only the critical heat flux limit is considered in the MAAP code evaluations. As discussed earlier, this presents a good average representation for the coolability limit as well as the rate at which debris would be quenched for the in-vessel and ex-vessel steam spike evaluations as presented in Ref. [5.9].

Simulation experiments for the potential of debris dispersal show that the containment criteria proposed in the ZPSS are indeed conservative. In these experiments debris dispersal was accomplished with velocities approximately one-third of those predicted by a direct entrainment criterion.

5.5 References

5.1 L. Barleon and H. Werle, "Dependence of Debris Bed Dryout Heat Flux on Particle Diameter," Transactions of the ANS, Vol. 38, p. 382, 1981.

5.2 D. Squarer, A. T. Pieczyhski, and L. E. Hochreiter, "Affect of Debris Bed Pressure, Particle Size and Distribution on Degraded Nuclear Reactor Core Coolability," Nuclear Science and Engineering, 80, p. 2, 1982.

5.3 R. Trenberth and G. F. Stevens, "Experimental Study of Boiling Heat Transfer and Dryout in Heated Particulate Beds," AEEW-R1342, July 1980.

5.4 D. R. Pedersen, et al., "Status Report on LMFBR Debris Accommodation Technology - 1982," ANL/RAS/82-20, June 1982.

5.5 S. W. Jones, et al., "Investigation of Limiting Boiling Heat Fluxes from Debris Beds," Transactions of the ANS, 35, pp. 361-363, 1980.

5.6 B. W. Spencer, D. Kilsdonk, J. J. Sienicki, and G. R. Thomas, "Phenomenological Investigations of Cavity Interactions Following Postulated Vessel Melt-Through," Paper presented at the ANS/ENS International Meeting on Thermal Reactor Safety, Chicago, Illinois, August 1982.

5.7 "Zion Probabilistic Safety Study," Commonwealth Edison Company, September 1981.

5.8 B. W. Spencer, personal communication, 1982.

5.9 "Final Report of Key Phenomenological Models for Assessing Non-explosive Steam Generation Rates," Fauske and Associates Report, FAI/82-30, December 1982.

6.0 APPLICATION TO REACTOR SYSTEMS

6.1 Introduction

The assessments for in-vessel and ex-vessel coolability, reactor vessel failure, and dispersive debris characteristics must be applied to the reactor systems for both BWR and PWR designs and the various containment configurations considered in the IDCOR program. This involves establishing the basic behavioral characteristics which influence coolability as well as the limitations on the rate of quenching for overheated core debris and the influence that this may have on the vessel failure mechanisms. In addition, the potential for dispersal must be tracked as a function of the postulated accident sequence and the specific containment configuration of interest. Guidelines for these evaluations as they are determined in the BWR-MAAP and PWR-MAAP coding systems are given below.

6.2 In-Vessel Debris Coolability

6.2.1 In-Vessel Debris Coolability with Limited Core Damage

As long as the core geometry remains intact, water addition at a rate considerably greater than that required to remove the decay power would be sufficient to terminate the accident sequence and establish coolability within the original core boundaries. For those postulated accident sequences where the core remains uncovered for an extended time interval, thereby allowing sufficient degradation to begin geometrical changes within the core, the potential for establishing coolable states is somewhat different for the BWR and PWR systems. This is due to the segmented core configuration typical of BWR systems as opposed to the open lattice configuration used in pressurized water reactors. In the segmented BWR configuration, considerable degradation could occur within a given fuel assembly. However, as long as the zircaloy fuel assembly cans essentially retain their intact configuration, water could be supplied through the interstitial spaces between the fuel cans and extract heat from the outer fuel can surface, thereby allowing the inner material to be quenched and permanently cooled.

Such an evaluation can be approximated as conduction through a cylindrical configuration with a radius of approximately 7 cm. In this configuration, it is assumed that significant degradation has occurred within the fuel can such that the material has lumped together and prevents water from flowing through the interior of the fuel can. The steady-state temperature difference between the central region and the outer wall of this badly damaged fuel can would be given by

$$T_{max} - T_{sat} = \frac{\dot{q}\, r_o^2}{4\, k_F} \tag{6.1}$$

where $\dot{q}$ is the internal volumetric heat generation, k_F is the corium thermal conductivity, T_{max} the the maximum temperature in the fuel region, and T_{sat} is the saturation temperature of the water at the primary system pressure. Assuming the decay power to be approximately 1 percent of the normal operating level, the steady-state temperature difference would only be 370°C. Such temperature levels are far below those required to melt any of the constitutive materials such as zircaloy, zirconium dioxide, or uranium dioxide. Also, these temperatures are considerably less than those required for significant oxidation should steam be available to the internal regions of the lumped material mass.

The above configuration could be maintained until the stainless steel control rod blades achieved temperatures where melting and relocation would occur. As a result, the heatup codes used in the MAAP coding system monitor the temperatures of the fuel bundle and the control rod blade to determine the time at which such geometric changes would be anticipated. Following this time, such an intimate cooling path is assumed to be unavailable.

For the open lattice configurations in PWR systems, the intact configuration would be maintained until either the zircaloy cladding, the stainless steel control rod fingers or the control rod material itself would be melted and liberated within the core. For those systems using silver-indium-cadmium control rod material, the low melting point of the silver and

the high cadmium vapor pressure would likely cause the stainless steel control rod fingers to be ruptured at temperatures well below the stainless steel melting point and the silver material would be liberated within the core. This could potentially alloy with the zircaloy cladding and drain into the cooler regions of the core where it could resolidify. As a result, the geometry of the system would have been substantially changed and the evaluation for core coolability in terms of an intact configuration should no longer be used. For those other PWR systems which use either hafnium or boron carbide control rod material, the temperatures for significant loss of intact geometry should be equated to stainless steel melting if the control rod fingers are made of such material or zircaloy melting should this material be utilized for the control rods.

6.2.2 In-Vessel Coolability with a Badly Distorted Core

These evaluations can be formulated through the use of the critical heat flux model discussed in Section 3 and with the assumptions of either the horizontal area available within the core or twice this area which accounts for some additional surface area due to the non-uniform accumulation of debris. As discussed in Section 3, and in Ref. [6.1] the comparison with TMI-2 data illustrates that the CHF model with an area twice that of the cross-sectional area available inside of the core barrel adequately represents the measured quenching behavior. Thus, it would also allow an evaluation for in-vessel coolability for a badly damaged state. This can be used to assess the potential for coolability as a function of accident sequences since the pressure within the primary system would be considerably different for those which result in a depressurized state (large break LOCA) as opposed to those which occur at pressures approaching the nominal operating value. Such global evaluations are illustrated in Table 6.1 for various primary system pressures. As illustrated, at the higher pressures, a coolable configuration could be achieved for a decay power of approximately 1 percent of the nominal operating value. However, even those regions in which a permanently coolable state could be achieved within the original core boundaries, the excess heat removal over that generated within the core is comparatively small. As a result, should material pour into the lower plenum of the vessel, the debris quenching rate would be comparatively slow and the time required for quenching the

Table 6.1

In-Vessel Heat Removal
Decay Power - 30 Mw

	System Pressure MPa	CHF kw/m^2	Heat Removal Capacity, Mw Area Planar	Area Hemispherical
I. PWR Systems (Planar Area ~ 12 m^2)	0.3	1,800	22	44
	4.0	4,075	49	98
	7.0	4,355	52	104
	17.0	2,665	32	64
II. BWR Systems (Planar Area ~ 16 m^2)	0.3	1,800	29	58
	4.0	4,075	65	130
	7.0	4,355	70	140

debris would be long compared to that required to fail the in-core instrument penetrations or control rod drive stub tubes. Even for those reactor vessels without lower head penetrations, the time required for vessel failure, Ref. [6.2], appears to be much less than that required to cool the debris. As a result, the potential for establishing an in-vessel coolable condition in the lower plenum of the reactor pressure vessel would be small. Therefore, in the MAAP evaluations, credit is not taken for establishing a coolable condition in the lower plenum of the reactor vessel.

6.3 Vessel Failure

6.3.1 BWR Systems

All BWR systems considered in the IDCOR program have cruciform control rods which enter through the bottom head of the reactor pressure vessel. These lower head penetrations are mounted with limited depth penetration welds on the inside of the reactor vessel head. In addition, the in-core instrument penetrations are also through the lower vessel head and have similar limited depth welds. As a result of accumulation of molten material in the lower head following the failure of the core support plate for severe core damage sequences, these lower penetrations are calculated to fail within a time interval of tens of seconds to a few minutes. This does not provide sufficient time for extracting the large amount of stored energy within the molten fuel debris which has poured into the lower plenum. As a result, vessel failure occurs well before the debris could be quenched. In the BWR-MAAP code evaluation, a single penetration is assumed to be the initial failure location and the ablation calculations are based upon this failure size. However, the effect of multiple penetrations failing simultaneously can be investigated in the MAAP daughter code, but typically this is not observed to be an influencial change. Specifically, the resulting vessel breach diameter following discharge of the molten core material into the containment building would be approximately 20 to 40 cm in diameter; the exact dimension being dependent upon the amount of core material accumulated on the core support structure prior to its failure. Such extensive ablation already encompasses several surrounding penetrations which would be those most likely to fail simultaneous if such behavior were to occur. Therefore, the single

penetration failure inherently represents multiple failures with respect to the vessel breach size with some minor change in the time for material discharge.

6.3.2 PWR Systems

For the Westinghouse and Babcock and Wilcox (B&W) systems considered in the IDCOR program, as well as the Combustion Engineering (CE) System 80 designs, the in-core instrumentation tubes penetrate through the lower vessel head. As a result, the vessel failure location resulting from molten debris pouring into the lower plenum is again the failure of these limited depth penetration welds. This failure is calculated to occur about 1 to 2 minutes after the accumulation of debris on the lower head of the reactor vessel. As with the BWR systems, the steaming rates off of the core material in the lower plenum are insufficient to extract the stored energy in the debris within the time interval required for failure at one of the penetrations. As a result, in-vessel coolability within the lower plenum is not credited within the PWR-MAAP code evaluations.

In the PWR evaluations, a single penetration is the initial failure size used in the PWR-MAAP code accident sequences and as discussed above, the influence of multiple penetrations failing simultaneously can be studied in the MAAP daughter code. As with the BWR cases, this is not found to be an influencial parameter on the overall primary system and containment response.

For those CE systems without instrument penetrations through the lower head, vessel head failure would be expected within a few minutes following core support plate failure as a result of the ablative attack induced by the molten corium jet. While the detailed mechanism is somewhat uncertain, the containment response is relatively insensitive to the initial failure size. Also, the actual time required for establishing a failure condition in the lower plenum is not an influencial parameter in the containment response since the steam produced within the primary system as the water attempts to quench the debris during the time that the lower head is undergoing thermal attack is merely accumulated within the primary system. Following failure of the reactor vessel lower head, this steam would be discharged to the contain-

ment atmosphere and essentially represents steam that could have been produced by corium-water interaction immediately following vessel failure. As a result, the containment atmosphere and the overall containment transient are not greatly affected by changes of a few minutes in the vessel failure time.

6.4 Core Debris Dispersal

6.4.1 BWR Systems

For the BWR reference plants investigated in the IDCOR program (Grand Gulf, Peach Bottom, and Susquehanna) the Mark-I and Mark-II containment systems have passageways between the pedestal and drywell regions which are open and are at the same level such that core material can flow from the pedestal region into the drywell due to gravity alone. Consequently, the evaluation for material dispersion due to the high pressure gaseous discharge following reactor vessel failure is only important in determining whether this material could be directly transported into the suppression pool wherein it could be quenched and coolable. In the BWR-MAAP code system, this direct transport of material into the suppression pool as a result of gaseous blowdown is not currently evaluated since there is no experimental data to provide guidance on the extent of such direct transport. In the BWR-MAAP system, the transport to the suppression pool is calculated if the molten debris can thermally attack portions of the containment structure, such as the downcomers in the Mark-II configurations, causing failure and allowing direct transport of core material into the suppression pool by drainage. Consequently, for these systems there is no evaluation of dispersive potential since the material has the ability to be transported from the pedestal region into the drywell in the absence of such dispersion.

For the Mark-III containment systems which have a "sunken" pedestal configuration with respect to the drywell, drainage of material from the pedestal into the drywell would not occur. However, for those sequences in which the reactor vessel is at an elevated pressure at the time of failure, the blowdown forces could have a significant effect on that material which is initially discharged from the primary system. Benchtop scale experiments have

been carried out at Argonne National Laboratory [6.3], with a configuration similar to a Mark-III containment using both water and Cerrelow-136, which is a low melting point alloy with a density of about 8,500 kg/m^3. These experiments demonstrated that disperson of material could occur due to the gaseous blowdown into this "sunken" pedestal region. The effects of such blowdown can be evaluated in terms of the general entrainment criteria for typical BWR-Mark-III containment systems.

For those sequences in a BWR Mark-III containment in which the reactor vessel is at an elevated pressure at the time of vessel failure, the high velocity gases exhausted after corium discharge could potential entrain and disperse the core debris. A model for evaluating this entrainment potential is developed below.

Assuming for simplicity that the blowdown of the vessel occurs isothermally, the gas velocity at the vessel breach would be sonic and is given by,

$$c = \sqrt{RT_g} \tag{6.2}$$

and the mass flow rate (W_g) can be expressed by,

$$W_g = \eta P_o A_b / \sqrt{RT_g} \tag{6.3}$$

In these equations A_b is the vessel breach area, P_o is the pressure within the reactor vessel, η is the isothermal critical pressure ratio, R is the gas constant for the mixture, and T_g is the gas temperature. As the sonic gaseous stream leaves the breach (throat) it would depressurize to the pedestal pressure and continue to accelerate. The gas velocity (u_a) after the stream depressurizes to the surrounding atmosphere is given by,

$$u_a = \frac{(\eta P_o - P_p)A_b}{W_g} + c \tag{6.4}$$

and this would occur within 4 or 5 breach diameters. After this pressure equilibration, the high velocity jet would entrain the surrounding atmosphere,

undergo several dynamic shocks and re-expansion and finally become subsonic at the pedestal pressure.

As the gaseous stream approaches the bottom of the pedestal, the flow must be stagnated and reversed. The one dimensional gas velocities can be estimated by assuming that the downward and upward streams each occupy one-half of the pedestal cross-sectional area (A_p) as shown in Fig. 6.1. Therefore, the upward velocity (U_1) is given by,

$$U_1 = \frac{2\, W_g\, RT_g}{P_p\, A_p} \tag{6.5}$$

This velocity can be compared to the entrainment velocity (U_e) as given by,

$$U_e = \frac{3.7\, \sqrt[4]{g\sigma(\rho_F - \rho_g)}}{\sqrt{\rho_g}} \tag{6.6}$$

where g is the acceleration of gravity, σ is the liquid-gas surface tension, with ρ_F and ρ_g being the corium and gas densities respectively. If $U_1 > U_e$, then material dispersal would occur.

For example, consider a reactor vessel pressure of 7 MPa, a gas temperature of 500 K and a breach area of 0.03 m^2. This would produce a gas flow rate of 660 kg/sec with a throat velocity of 700 m/sec and a jet equilibration velocity of 1400 m/sec. With a pedestal area of about 29 m^2, the upward one dimensional velocity would be approximately 106 m/sec. This is to be compared to an entrainment velocity of 90 m/sec, i.e., entrainment and dispersal would be anticipated. It should also be noted that geometry influences the entrainment behavior and with this flow stagnation and reversal, one would expect entrainment and material removal at velocities below that predicted by Eq. (6.6).

These evaluations demonstrate that dispersion could occur for these BWR Mark-III configurations, but it should be recalled that for most BWR accident sequences, the automatic depressurization system is activated on high

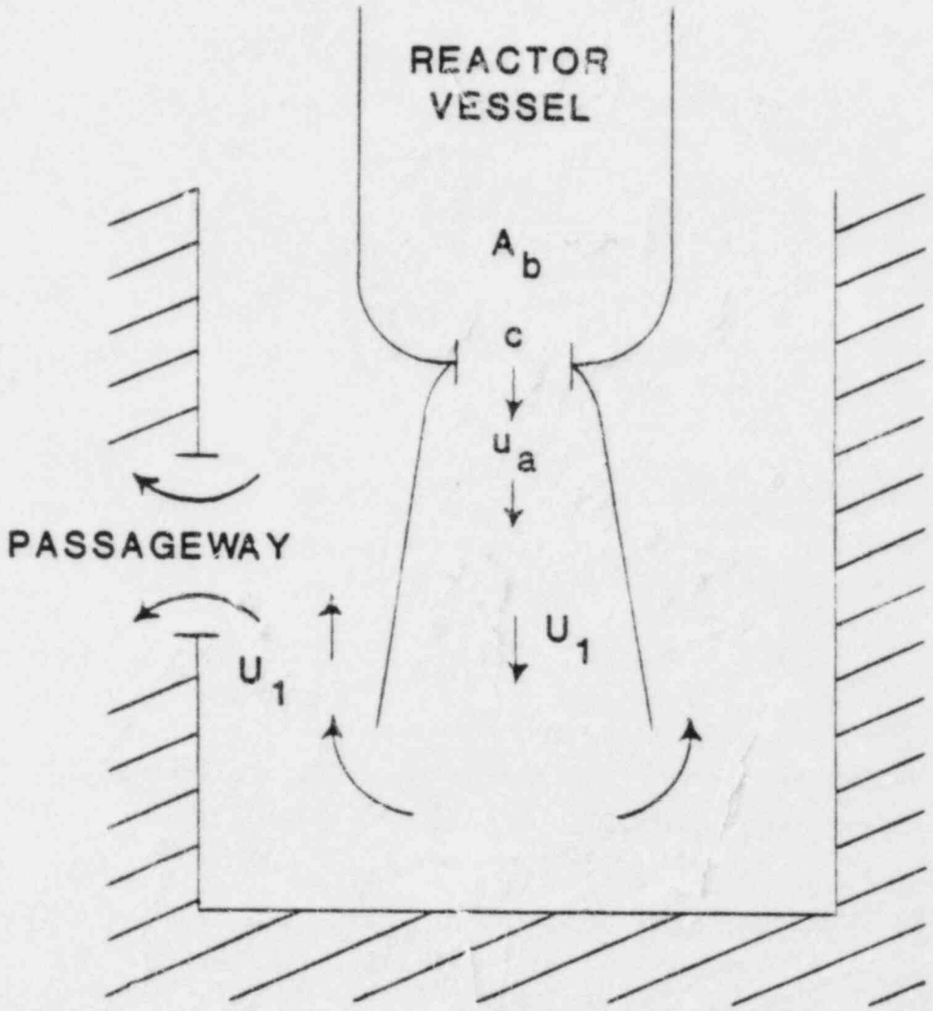

Fig. 6.1 Entrainment evaluation.

drywall pressure. As a result, the primary system is generally depressurized for most of the accident sequences and there is little potential for disperal forces as a result of the primary system blowdown following reactor vessel failure. Within the BWR-MAAP code system for the Mark-III containments, the entrainment criteria is applied as discussed above and if the velocities are sufficient to cause direct entrainment of the debris, the material is deposited on the drywell floor. That material which is lost from the primary system at a later time is then accumulated in the pedestal region as it drains from the primary system. Given this distribution of material, the debris coolability and/or the core-concrete thermal attack is evaluated in both of these regions.

6.4.2 PWR Systems

The general behavior for dispersal in a PWR system with a Zion type reactor cavity/instrument tunnel configuration was presented in Section 3. With this comparatively smooth tunnel configuration (essentially no regions where substantial material could be entrapped and retained), the dispersive calculations demonstrate that the debris would be anticipated to be removed from the reactor cavity/instrument tunnel region and deposited on the containment floor. In the PWR-MAAP code analyses, this material is distributed on the containment floor inside of the missile barrier where additional water is retained and substantial vaporization is calculated as the debris is quenched. This steam spike is a major part of the containment transient following vessel failure and is important in the assessment of a combustible atmosphere during this and subsequent portions of the accident sequence.

For the reactor cavity/instrument tunnel configuration at Sequoyah, which is shown in Fig. 6.2, there are several regions in which debris could be entrapped as a result of movement from the reactor cavity towards the openings at the top of the instrument tunnel. These openings are in the hatch, which covers the personal accessway into the instrument tunnel, and potentially through the seal table where the instrument tubes are terminated. As illustrated in Fig. 6.2, the upward sloping portion of the instrument tunnel begins at a point about 2 m above the floor of the reactor cavity and tunnel region. Consequently, this is a place where debris could be entrapped as

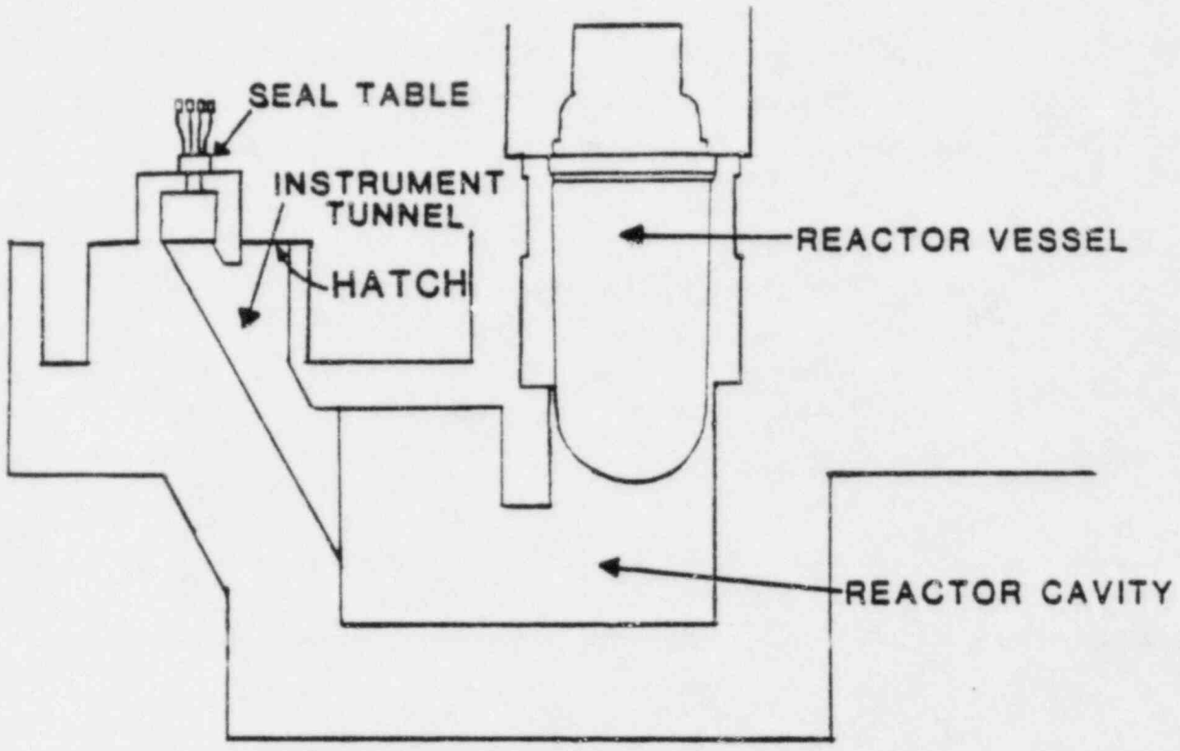

Fig. 6.2 Sequoyah reactor cavity/instrument tunnel configuration.

schematically represented in Fig. 6.3. In this region, the major flow field would pass over that region represented by the corner below the entry of the upward sloping wall of the instrument tunnel, and assuming that this can be approximated by a line extrapolated down from the upward sloping portion, half of the core material could be retained in this region. In addition, the configuration of the instrument tunnel in the vicinity of the seal table also tends to provide considerable separation of the debris.

More importantly, the Sequoyah cavity design is divided into a region directly below the reactor vessel, which is about 6 m in diameter, and that between the vessel and the beginning of the instrument tunnel. This latter region is about 6 m wide and 7 m high, a cross-sectional area of about 42 m^2, which is about 3.5 times that of Zion. Consequently, the one-dimensional velocity through the Sequoyah cavity during the gaseous blowdown period is much less than would be the case for a similar postulated accident sequence at Zion. With this lower velocity, the potential for debris entrainment in the cavity region is markedly reduced and the 2 m vertical step at the entrance of the instrument tunnel would act as a separator to "catch" high density material which had been entrained. Also, as discussed in Section 3, material could be removed as a wave formed by the initial blowdown forces. But with the increased cross-sectional area and the 2 m vertical step, waves would decrease in amplitude as the gases by-pass the wave crest as the area expands. Also, the vertical step would "catch" any material transported along the cavity floor.

Another feature of the Sequoyah instrument tunnel design which would influence material removal is the configuration of the personnel access hatch. This also serves as a path for air circulation and provides an exhaust for the gaseous blowdown. With the initiation of the gas discharge, this hatch would be opened with a resulting flow area of about 4.5 m^2. For an assumed accident condition of 7 MPa primary system pressure at the time of vessel failure, the initial gas flow rate would be about 400 kg/sec, producing a velocity at the personnel hatch of about 100 m/sec. The stagnation pressure associated with this velocity is about 4.5 kPa and it is doubtful that the seal table would be disrupted at this modest pressure. Therefore, the region below the seal table would act as a separator for the limited amount of material which could be swept into the instrument tunnel.

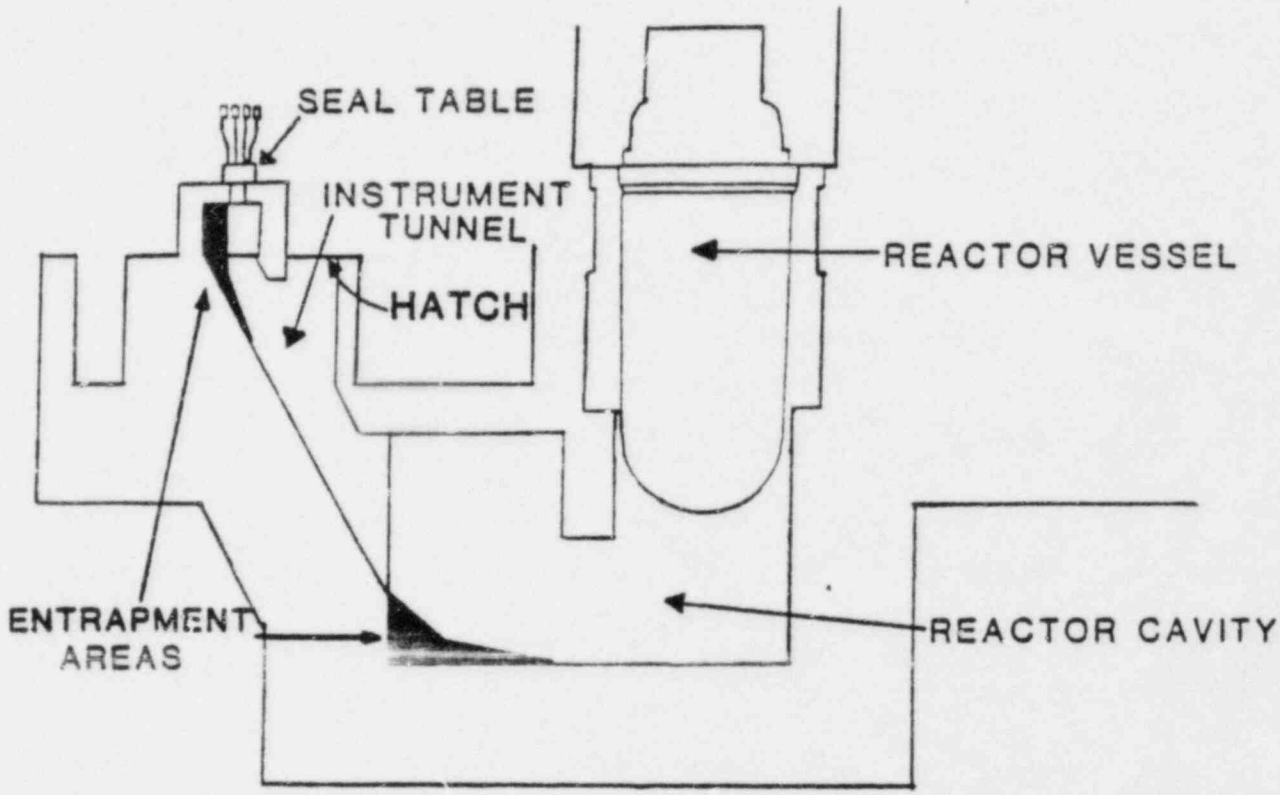

Fig. 6.3 Areas for debris retention in the Sequoyah reactor cavity/instrument tunnel configuration.

While the general arrangement of the Zion and Sequoyah reactor cavities and instrument tunnels are similar, the above considerations of the specific design features lead to greatly different predictions for core dispersal. In Zion, the smooth cavity configuration and single exit path make dispersal of the debris released before the blowdown highly probable. However, for Sequoyah, the large cross-sectional area, the 2 m vertical step and the personnel hatch/seal table configuration would cause the debris to be retained in the cavity.

6.5 Ex-Vessel Coolability

For all containment systems, the ex-vessel coolability for debris and contact with water is assessed through the flat plate critical heat flux limit discussed in Section 3. This heat flux is multiplied by the available floor area within a specific region to determine the heat removal from the debris beds in the presence of water. If this exceeds the decay power, then the debris is eventually quenched and a coolable debris bed is formed as long as water is continually supplied to the debris. This quenching of debris can be illustrated by the particle data of Cho et al., Ref. [6.4], which was discussed in Ref. [6.5]. This can also be demonstrated by a concrete attack experiment run at Sandia and reported at the 1981 NRC LWR Reactor Safety Information Meeting, Ref. [6.6]. In this experiment, a 50 kg iron mass was heated in a cylindrical concrete cavity be an induction coil surrounding the concrete block. The temperature history recorded for the experiment is illustrated in Fig. 6.4. As shown, the temperature of the block was above the concrete ablation temperature for an extended period of time ($\sim$ 2 hrs.). Thirty minutes after the onset of ablation, a crust was formed over the top of the cavity and the temperature rise rate increased as a result of the decrease in upward heat losses. When this crust was deliberately broken, the measured temperature decreased dramatically and subsequently increased when the crust began to reform. After 187 minutes of operation, the steel penetrated radially through the concrete, contacted the power coils, and caused the power circuit to trip. During the subsequent cooling process, the crust solidified and 17 minutes later, the upper region of the cavity was flooded with water. As illustrated by the temperature history shown in Fig. 6.4, this water addition resulted in a substantial increase in the cooling rate. As discussed in

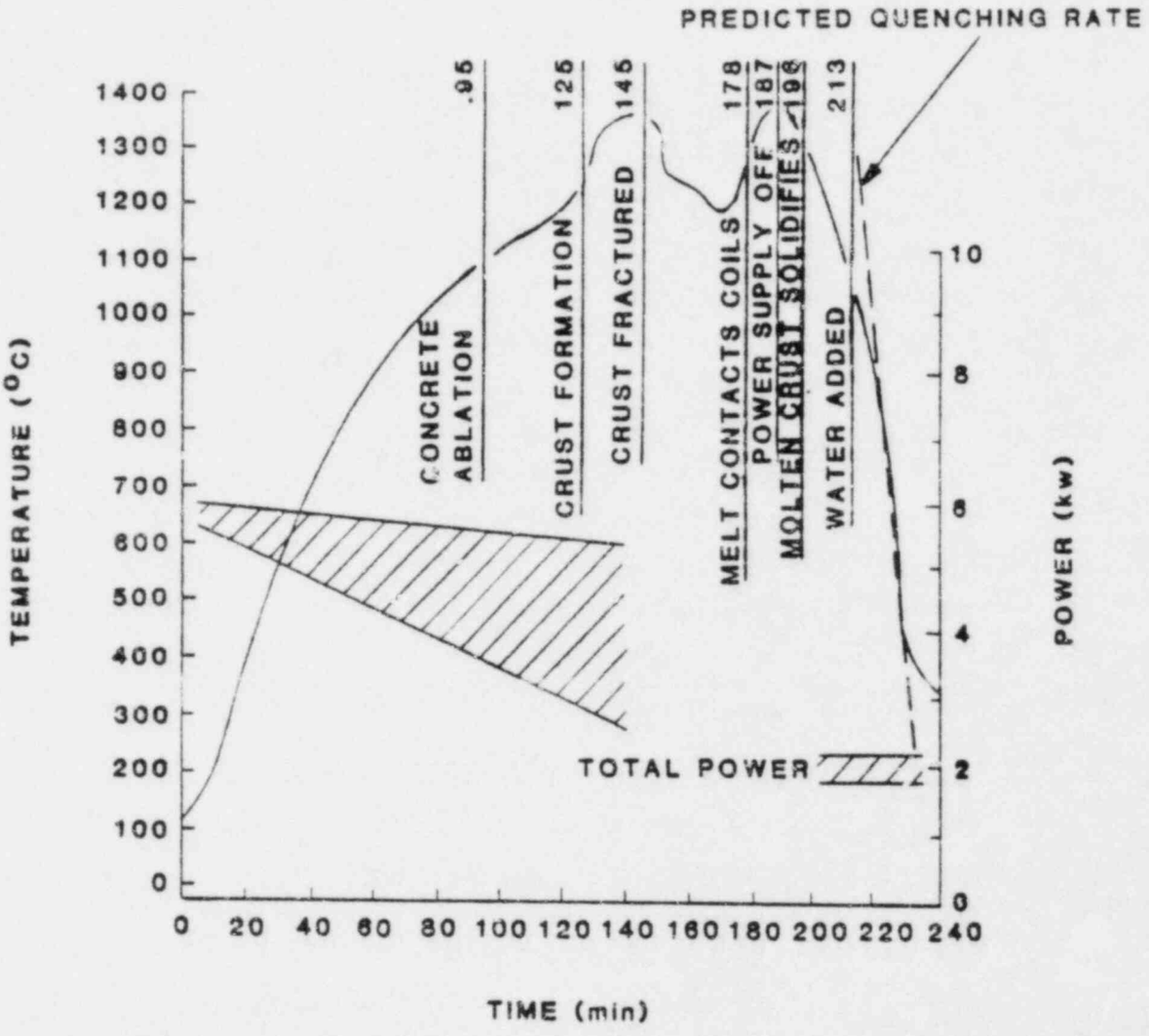

Fig. 6.4 Temperature and input power history.

Ref. [6.6], the water did not instantaneously vaporize, but boiled off over a several minute interval.

Figure 6.5 illustrates the post-test configuration in which the steel ablated the concrete in both the downward and sideways directions. The amount of concrete attack and the subsequent material relocation were extensive. With the degree of attack illustrated in Fig. 6.5 and the cooling rate given in Fig. 6.4, the net quenching rate of the steel-concrete mixture can be estimated and compared to the CHF model. If the overall mass shown in Fig. 6.5 is assumed to have the configuration of a trucated cone with an average base diameter of 33 cm, a height of 42 cm, and a diameter of 22 cm at the upper surface, the total volume would be almost 19,600 cm^3. The steel had an initial diameter of 20.3 cm and was 19.7 cm high, corresponding to a volume of 6373 cm^3, thereby giving a volume for the once molten concrete of approximately 13,200 cm^3. Assuming the entire mass of steel and concrete to have the same quenching rate, the energy removal rate (q) can be determined from

$$q = [m_s c_s + m_c c_c] \frac{dT}{d\theta} \tag{6.7}$$

where m_s, m_c, c_s, and c_c are the masses and specific heats of the steel and concrete respectively. Using average values of 2300 kg/m^3 for the concrete density and 0.8 kJ/kg °K for the concrete specific heat, along with the cooling rate of 0.8 °K/sec. shown in Fig. 6.4, the energy extraction rate would be 35 kw. The cavity diameter of 22 cm provides an area of 0.038 m^2 and a resulting heat flux over this area of 921 kw/m^2. With the altitude at Sandia, the flat plate critical heat flux (q/A)

$$q/A = 0.14\, h_{fg} \sqrt{\rho_g}\ \sqrt[4]{g\sigma(\rho_f - \rho_g)} \tag{6.8}$$

value at the local pressure is about 1100 kw/m^2 for saturated liquid conditions. In this equation, h_{fg} is the latent heat of vaporization, ρ_f and ρ_g are the saturated water and steam densities respectively, g is the acceleration of gravity, and σ is the liquid-vapor surface tension. This is in remarkable agreement with the experimental result considering (1) the simplifying approximations and (2) that some non-condensible gases were

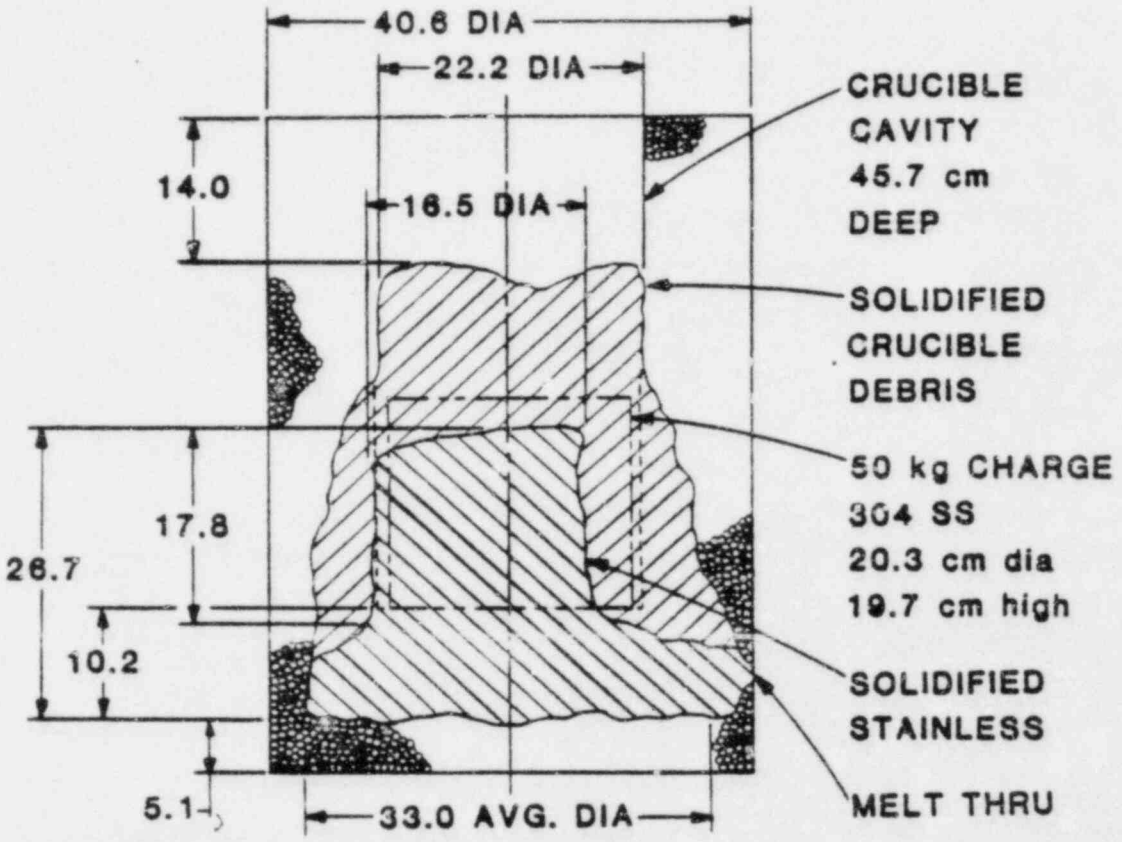

Fig. 6.5 Experimental configuration and post-test material location.

generated and must also be eventually cleared from the cavity region. This quenching rate persisted even though the cavity opening was covered by a crust of once molten concrete material. However, this crust had sufficient cracks, or vent holes, to allow the downward penetration of water and the upward alleviation of the steam formed by the quench. Such close agreement between the model and crusted over molten pool demonstrates the applicability of the approach to reactor accident analyses.

In the absence of water, the heat transfer from the debris is calculated as a result of convection and radiation with the convection being driven between containment compartments as a result of natural circulation. If the energy can be extracted from the debris such that the interface temperature with the concrete does not exceed the concrete melting point, then a quasi-coolable state would be achieved since the concrete attack would be extremely slow. As the decay power decreased, the stability of this state would increase and after a few tens of hours at a very minimal attack rate, this would eventually become a permanently coolable configuration. In this dry atmosphere heat removal configuration, the energy must also be extracted from the containment or an overpressurization would ultimately occur. In general, this is accomplished through either active heat removal with fan coolers or the onset of containment sprays or directly through the containment wall for those systems which may have an uninsulated steel containment shell.

6.6 Summary

In-vessel coolability could potentially occur if water is added to the primary systems prior to the time at which sufficient core material is accumulated on the core support plate to result in failure of this structure. If debris is transported into the lower plenum, the detailed evaluations for both BWR and PWR systems illustrate that the potential for in-vessel coolability is small. Therefore, in the MAAP code evaluations, no credit is taken for in-vessel coolability when the material has already begun to migrate into the lower plenum.

For both BWR and PWR systems, the time of vessel failure is between ten of seconds and a few minutes for failure of the limited depth penetration

welds used for the in-core instrument penetrations and for the CRD stub tubes in the BWR design. For the vessels without lower head penetrations, the assessment for vessel failure also shows a time interval of a few minutes following the pouring of debris into the lower head of the reactor vessel. Therefore, all of these systems have failure times of about the same magnitude with the most likely failure location to be the central region of the lower head.

Dispersive characteristics for BWR systems are somewhat less important than for PWR designs since the automatic depressurization system causes most BWR accident sequences to have a depressurized primary system at the time of reactor pressure failure. However, for those systems where such evaluations are pertinent, i.e. the Mark-III system, experiments have been carried out and models are incorporated in the BWR-MAAP code to determine if sufficient potential exists for dispersal. If this is the case, the material is removed from the pedestal region and distributed on the drywell floor.

For the PWR systems, the details of the specific reactor cavity/instrument tunnel configurations are influential in determining whether such dispersive potential is realistic or whether the debris can be retained and "pockets" formed by the specific geometry. In essence, this must be decided through hand calculations for the specific reactor cavity/instrument tunnel configuration of interest and must then be incorporated into the MAAP code for the system to determine if sufficient dispersive potential is available. In the case of the Zion design, the smooth reactor cavity/instrument tunnel geometry allows for complete and rapid removal of debris from the reactor cavity region when the primary system is blowing down from an elevated pressure. However, considering the specifics in the Sequoyah design, the debris would be anticipated to be held up in the "pockets" provided at the juncture between the horizontal and upward sloping portions of the instrument tunnel and potentially in the vicinity of the seal table. Following the blowdown, and material near the seal table would fall or drain back into the reactor cavity.

To establish ex-vessel coolability, the debris must be able to extract its decay power and a heat transport path must be developed to remove

the energy from the containment atmosphere. For those accident sequences in which the debris is covered by water, the ability to extract the decay power is determined through the application of the critical heat flux formulation applied over the cross-sectional area of the containment area. If this energy removal rate exceeds the decay power generated, the debris would be quenched and a permanently coolable state established as long as water could be supplied on a continual basis. For those configurations where debris could be accumulated in a sufficiently thin solid layer that it could exchange its energy directly with the containment atmosphere, the debris would be coolable as long as the energy could be removed from the containment environment either by direct heat removal through fan coolers, etc. or directly through the containment shell.

6.7 References

6.1 "Final Report of Key Phenomenological Models for Assessing Non-explosive Steam Generation Rates," Fauske and Associates Report No. FAI/82-30, December 1982.

6.2 L. E. Anderson, et. al., "Effects of Hypothetical Core Melt Accidents on a PWR Vessel With Top-Entry Instruments," EPRI/NSAC Final Report for IDCOR Subtask 15.2, May 1983.

6.3 B. W. Spencer, personal communication, January 1983.

6.4 D. H. Cho, D. R. Armstrong, L. Bova, S. H. Shan, and G. R. Thomas, "Debris Bed Quenching Studies," Paper presented at the ANS/ENS International Meeting on Thermal Reactor Safety, Chicago, Illinois, August, 1982.

6.5 "Final Report of Key Phenomenological Models for Assessing Non-Explosive Steam Generation Rates," Fauske and Associates Report, FAI/82-30, December 1982.

6.6 W. W. Tarbell, "Core/Concrete Experiments at Sandia National Laboratories," Paper presented at the USNRC LWR Safety Information Mtg., Gaithersburg, Maryland, 1981.

7.0 SUMMARY AND CONCLUSIONS

With these assessments for in-vessel and ex-vessel coolability, vessel failure, and core debris dispersion, the following conclusions can be made and are incorporated into both the BWR-MAAP and PWR-MAAP coding systems.

1. If water can be added to the damaged core prior to the time that molten debris fails the core support structure and pours into the lower plenum, the establishment of an in-vessel coolable state is very likely. This is calculated in the MAAP codes as a competitive process between continued heat-up of the debris and the overall quenching with the principle diagnostic being the amount of molten debris accumulated on the core support structure. These coding systems allow for continued heat-up during the quenching process. The evaluation for quenching is conservatively represented by the flat plate critical heat flux criteria applied to the cross-sectional area inside of the downcomer/shroud of the reactor vessel. For those times at which the primary system has retained its intact configuration, the quenching process is evaluated through water refill, if the water is added from below, or through an annular flow flooding criteria if the water is added from above (core sprays or upper head injection). Also, some water can be allowed to by-pass from the upper core region to the vessel lower plenum.

2. When material migrates into the lower plenum of either BWR or PWR systems, the combination of large amounts of stored energy within the debris, the limited quenching rates provided by the cross-sectional area in the bottom of the vessel and the comparative short times to reactor pressure vessel failure do not provide for a high likelihood of establishing a coolable state within the lower head. As a result, the MAAP code calculations for both BWR and PWR systems predict that vessel failure would occur under these circumstances and debris would be discharged to the containment building.

3. For those BWR and PWR systems with extensive penetrations through the lower head, the limited depth welds for these penetrations would be the major mode of reactor vessel failure and this is calculated in the MAAP coding systems. For those PWR designs without penetrations through the lower head, separate analyses have shown that the failure would occur in the central region of the lower head after a time interval of several minutes. Therefore, the vessel failure mode for all reactor systems is calculated to be the central region of the lower head with the ablation caused by the discharge of molten corium to determine the breach size in the primary system.

4. For those accident sequences with an elevated primary system pressure at the time of reactor vessel failure, the blowdown of the primary system could substantially influence the distribution of core material within the containment. These analyses have been carried out for both BWR and PWR systems and they have been shown to be greatly influenced by the containment configuration. Therefore, the MAAP coding system contains the pertinent physical models to determine whether the potential exists for removal of debris from the reactor cavity/pedestal regions. However, the users must review the specific reactor cavity/ pedestal configuration and determine whether such debris removal would be allowed given the specifics of the design.

5. Ex-vessel debris coolability is generally dependent upon the continued availability of water to the debris configuration. In essence, if water is available on a continual basis the development of a permanently coolable state is likely. For those systems where water cannot be supplied to the debris, the internal energy generation can be potentially removed through thermal conduction within the slab type configuration. However, in both cases, a heat transport path must be established to remove the energy from the containment atmosphere and eventually from the containment building. This can be accomplished with either the available safety features such as contain-

ment sprays or fan coolers, or in some cases, by direct heat removal through the containment building shell. Again, this is dependent upon the specific design characteristics of the containment building and the heat removal systems provided for accident response.